Cranfield

College of Aeronautics Report No 9014
August 1990

Steady-State Experiments for Measurements of Aerodynamic Stability Derivatives of a High Incidence Research Model Using the College of Aeronautics Whirling Arm

M.J.M.Mulkens and A.O.Ormerod

College of Aeronautics
Cranfield Institute of Technology
Cranfield, Bedford MK43 0AL. England

ERRATA OF C.U.A. REPORT 9014

p.5, to be added: GPIB = General Purpose Interface Bus (Subroutines called IEEE-488.)

IEEE = Institute of Electrical and Electronics Engineers

p.11, second paragraph, 5 lines from the top: 'called MIRM I and MIRM II' should be: 'called MIRM I and MIRM II.'

p.20, formula (3.3): C_{M_j} should be C_{N_j}.

p.50, ref. 3: 'Unpublished.'

p.51, ref. 9: "D.W. Bayer" should be: "D.W. Beyer", and "1983" should be "1985".

p.52, ref. 20: "Rowthorne" should be "Rowthorn".

p.57, The selected NAG-routine F01JAF is actually a wrong choice. The correct routine should have been F01JBF. However, subsequent runs with the correct routine showed no differences in results.

p.58, first line: "For the 2-D scale MIRM II model" should be: "For the 2-D scale MIRM I model."

p.60, 7 lines from the bottom: "The values as found for this previous" should be: "The values as found for this previous"

p.71, second line from the bottom: "...of tubing system." should be "...of tubing systems."

Fig. 3.1, on the bottom right, "(GPIB)" should be "(RS-232)"

fig. 4.1, to be added: NRC = 0.1250.

fig. 4.2, for v_∞=70 m/s, $Re=1.7\times10^6$, there is a significant data point missing: (x,y) = (22.2°,-5.5).

fig. 4.16, 4.17 and 4.18: the ADS tests had a Reynolds number of 1.9×10^6.

Feb 1st, 1993

Cranfield

College of Aeronautics Report No 9014
August 1990

Steady-State Experiments for Measurements of Aerodynamic Stability Derivatives of a High Incidence Research Model Using the College of Aeronautics Whirling Arm

M.J.M.Mulkens and A.O.Ormerod

College of Aeronautics
Cranfield Institute of Technology
Cranfield, Bedford MK43 0AL. England

ISBN 1 871564 11 5

£10.00

Abstract

This report describes work done as part of the Ministry of Defence high incidence research project.

The High Incidence Research Model I (HIRM I) and HIRM II, representing configurations of highly manoeuvrable combat aircraft are being tested in the Cranfield Institute of Technology Whirling Arm facility, which is used to simulate a curved motion in flight and to obtain rotary derivatives. This report describes the work done for the measurement of the effects of steady pitching and yawing on HIRM I and II. Also, it describes the development of the (internal) strain gauge balance and models, used in these tests. Additional work as part of the research project involves transient experiments using the Whirling Arm, but this will be described in a future report.

The specially designed model and balance system were mounted on the Whirling Arm rig, as used for other projects. The signals coming from the balance were measured and processed, deriving the three moments, side and normal force acting on the model. Further processing by computer programs provided the aerodynamic coefficients and stability derivatives.

A five hole nose probe mounted on the model was used in some tests, to give improved data on angle of attack and dynamic pressure. Geometric incidence information was obtained from a linear transducer linked to the incidence changing mechanism.

The work described in this report is carried out under MOD Research Agreement (RA) AT/2028/0143, except for the work as described in chapter 4.4 and parts of appendix 1, which has been carried out under RA 2028/187/XR/AERO.

CONTENTS

LIST OF ABBREVIATIONS

ADR	Acceleration Derivative Rig
AGARD	Advisory Group for Aerospace Research and Development
AIAA	American Institute of Aeronautics and Astronautics
ARC	Aeronautical Research Council
CIT	Cranfield Institute of Technology
CoA	College of Aeronautics
CRP	Carbonfibre Reinforced Plastic
FF	Free Flight
FORTRAN	FORmula TRANslator
GRP	Glassfibre Reinforced Plastic
HIRM	High Incidence Research Model
LAPR	Large Amplitude Pitching Rig
MOD	Ministry Of Defence
MRC	Moment Reference Centre
NACA	National Advisory Committee for Aeronautics
NAG	Numerical Algorithms Group
NASA	National Aeronautics and Space Administration
NPL	National Physical Laboratory
PC	Personal Computer
RA	Research Agreement
RAE	Royal Aerospace Establishment
RR	Rolling Rig
SAOR	Small Amplitude Oscillatory Rig
WA	Whirling Arm

NOTATION

Note :

The notation of normalized derivatives of forces and moments and the notation of aerodynamic coefficient derivatives is entirely according to ref. 10, conforming to the notation standard as used in other work done on HIRM. It should be noted that wherever a moment is denoted, "script" letter font is used, *eg* $\mathcal{L}$, $\mathcal{M}$, and $\mathcal{N}$ in order to prevent confusion with L, M and N, denoting aerodynamic lift, Mach number and normal force respectively. For the sake of convenience, the table depicting the divisors for obtaining normalized quantities is given in table 3.1 (Source : ref. 10). The representative length l_0 as mentioned in this table is equal to $\bar{c}$ for the longitudinal mode and equal to b for the lateral/directional modes. Regarding the above-mentioned, it will be sufficient to give a few examples of derivatives of the pitching moment :

$$C_{\mathcal{M}} = \frac{\mathcal{M}}{(0.5\rho V^2 S\bar{c})}$$

$$C_{\mathcal{M}_q} = \frac{\partial C_{\mathcal{M}}}{\partial \check{q}} = \frac{\partial C_{\mathcal{M}}}{\partial\left(\frac{q\bar{c}}{V}\right)} = \frac{1}{0.5\rho V S\bar{c}^2} \times \frac{\partial \mathcal{M}}{\partial q}$$

$$\mathcal{M}_q = \frac{\partial \mathcal{M}}{\partial q}$$

$$\check{\mathcal{M}}_q = \frac{\mathcal{M}_q}{0.5\rho V S\bar{c}^2} = C_{\mathcal{M}_q}$$

A	matrix as used in Appendix 1
A	factor defined by (A2.2)
A	cross-section area
a	acceleration
B	matrix as used in Appendix 1
B	factor defined by (A2.3)
b	wingspan

$\underline{b}$	vector as used in Appendix 1
$\bar{c}$	mean aerodynamic chord
$\underline{c}$	vector as used in Appendix 1
D	outer diameter
d	inner diameter
F	force (in general)
g	gravity constant
$\mathscr{L}$	rolling moment
L	aerodynamic lift
$\underline{l}$	loading vector, front station
l	length (in general)
l_0	characteristic length
l_k	loading k on front balance station (k = p,y,n,r)
$\mathscr{M}$	pitching moment
$\mathscr{M}$	moment (in general)
M	Mach number
M	front strain-gauge station calibration matrix
m	mass
m_{ij}	element of matrix M
$\mathscr{N}$	yawing moment
N	normal force
n	revolutions per time-unit
P	power
p	rolling angular velocity
p	pressure
q	pitching angular velocity
q	dynamic pressure
R	radius
R	aerodynamic force (in general)
Re	Reynolds' number
r	yawing angular velocity
r	radius
S	wing area
$\underline{s}$	signal vector, front station
s_k	signal of front strain-gauge bridge, belonging to k. (k=p,y,n,r)
u	component of the airspeed along the X-axis

u	small perturbation of the component of the airspeed along the X-axis
V	airspeed
V	speed (in general)
v	component of the airspeed along the Y-axis
v	small perturbation of the component of the airspeed along the Y-axis
w	component of the airspeed along the Z-axis
w	small perturbation of the component of the airspeed along the Z-axis
X	axial force
$\underline{x}$	vector as used in Appendix 1
x_i	coordinate of any MRC along the X-axis. (i=1,2,...)
x_Z	x-coordinate of line of action of force Z
x_Y	y-coordinate of line of action of force Z
Y	side force
$\underline{y}$	vector as used in Appendix 1
Z	-N

α angle of attack ≡ arctan(w/u)

β angle of sideslip ≡ arcsin(v/V) = $\arctan\left(\frac{v}{\sqrt{u^2 + w^2}}\right)$

ϕ roll angle

φ angular position of the incidence gear of $\dot{\alpha}$-rig

η control surface deflection

$\underline{\lambda}$ loading vector, rear station

λ_k loading k on rear balance station (k=p,y,n)

μ_{ij} element of matrix Ω

Ω rear strain gauge station calibration matrix

ω angular velocity, *eg* of the WA

ω_{ij} element of matrix χ

ρ air density

σ_k signal of rear strain-gauge bridge belonging to k (k=p,y,n)

$\underline{\sigma}$ signal vector, rear station

τ angle between probe and tunnel axis as used in App. 2

Subscripts / superscripts :

.	time-derivative
..	second order time-derivative
A	aerodynamic body axis
aero	aerodynamic
B	bottom
C	foreplane ("canard")
C	centre
c	centrifugal
F	front
F	flap
G	geometric body axis
geom	geometric
i	denotes "top-in" or "top out"
j	denotes "front" or "rear"
max	maximum
mrc	moment reference centre
n	normal force
P	port
p	pitching moment
pr	pressure transducer
probe	nose probe
R	rear
r	rolling moment
req	required
S	starboard
s	swirl
s	static
stat	static
T	tailplane
T	top
t	total
tot	total
y	yawing moment

1 Introduction

An important aspect in the design of modern combat aircraft is to achieve a high standard of maneuverability. This is not only required to avoid attacks from enemy aircraft or weapons, but also to get into a proper position for aiming weapons to be locked on and released towards enemy targets. Thus, it is highly desirable the aircraft is able to fly tight turns in combat situations. The high lift in these manoeuvres necessitates flight at high angle of attack, quite often beyond the onset of flow separation over the upper wing surface. For that reason, the aerodynamic phenomena in the angle of attack region between flow separation and maximum lift needs to be understood well.

About 1980, the Royal Aircraft Establishment started a programme of research, aiming to study the characteristics of and to produce a mathematical model for a configuration considered to have characteristics desirable for a new combat aircraft. The programme now involves free flying models of two different configurations, called HIRM I and HIRM II. (HIRM - High Incidence Research Model) (see Fig. 1.1). HIRM I is a "three surface" configuration and HIRM II a canard configuration without tailplanes and a higher swept main wing than HIRM I. In order to establish or justify data used in flight control systems for these models, it is necessary to perform both static and dynamic wind-tunnel tests. For this purpose, a range of 4/9 scale and 2/9 scale models have been manufactured (full scale being defined as the free-flight model sizes), each being purpose-built for dynamic or static testing in wind tunnels; (See table 1.1 for an outline). Some of these models are used for oscillatory wind-tunnel testing. When simulating small perturbations from straight, steady flight it is possible, by using certain mathematical techniques, to derive the longitudinal stability derivatives $M_q+M_{\dot{w}}\cos(\alpha)$. This derivative describes the combined effect of two components of motion, a pitch without change of incidence and an incidence change without change of pitch. When testing in the directional mode, it is possible to derive $N_r-N_{\dot{v}}\cos(\alpha)$.

The CIT Whirling Arm facility is being used to test specially manufactured 4/9 scale models of HIRM I and HIRM II. The Whirling Arm (Fig. 1.2) is a counterbalanced arm of approximately 8 m radius, being able to turn at approximately 25 rpm. At the end of one of the arms, a model can be mounted, so that it is moved through the annular shaped test passage. (The WA is described in more detail in Chapter 2.2.) This manner of testing gives the model a curved path through the air. This is fundamentally different from conventional wind tunnels, where air is intended to flow in a uniform direction over a stationary model. In the longitudinal mode (Y-axis of the model vertical), there is a pitching angular velocity q. In the directional mode (Y-axis of the model horizontal) there is a yawing angular velocity r. This obviously allows examination of the aircraft behaviour under continuously curved flow with no change in incidence or sideslip. It is therefore possible to derive the stability derivatives $\check{M}_q$ and $\check{N}_r$, rather than $\check{M}_q+\check{M}_{\dot{w}}\cos(\alpha)$ and $\check{N}_r-\check{N}_{\dot{v}}\cos(\alpha)$ as can be obtained from the oscillatory tests.

The ability to measure $\check{M}_q$ and $\check{N}_r$ separately on the WA gives it a unique capability. However, comparison with oscillatory results must be done with great care: Since the oscillatory tests are dynamic, the forces and moments acting on the model are time-dependent. For example, the "reduced frequency" $\frac{q\times\bar{c}}{V}$ (with q being the maximum pitching angular velocity in these tests) may have influence on the magnitude of $\check{M}_q$ derived from these tests. For the WA tests, we have:

$$\frac{q\bar{c}}{V} = \frac{q\bar{c}}{qR} = \frac{\bar{c}}{R} \tag{1.1}$$

So, for a given model we can only test at one particular "reduced frequency". The mathematical formulation of the stability derivatives usually applies for small perturbations only, meaning for *eg* the longitudinal case that q (and hence $\frac{q\bar{c}}{V}$) has to be "sufficiently" small. The Whirling Arm results are derived from the effects of finite changes in pitch. The only variable is the change from positive to negative pitch rates.

A difficulty in WA testing is the presence of "swirl", *ie* the air in the test passage is not standing still but moves around due to the turning of the arm and the model. This obviously has to be minimized because of the loss of dynamic head, possible extra turbulence, and a non-linear velocity profile in the test passage. The swirl problem can be understood and controlled to a limited extent. The work done by D. Llewelyn-Davies (ref. 1) consists of swirl-measurements and adding swirl-reducing devices. An additional swirl problem encountered during HIRM testing will be discussed in Chapter 4.3.

2 Equipment

2.1 Introduction

The Whirling Arm facility has been modified by D. Llewelyn-Davies (ref. 1). These modifications consisted of:

1. Modifications to reduce swirl.
2. Development of a model support system.
3. Installing instrumentation for data acquisition and control.

All these modifications have been used for the earlier experiments as mentioned ref. 1. For the HIRM experiments, some extra development was necessary :

4. 4/9 scale models of HIRM I and II (Chapter 2.3).
5. A special internal strain-gauge balance (Chapter 2.4).
6. Use of nose probe pressure transducers (Chapter 2.5).

2.2 The Whirling Arm

The College of Aeronautics Whirling Arm (Fig. 1.2) was first installed at the National Physical Laboratory in 1942. This was the third WA at the NPL and a brief description of the first two can be found in ref. 1. The third NPL Whirling Arm was moved to Cranfield during the 1950's. Since it is described extensively in ref. 1, only the most important matters are mentioned here.

The CIT Whirling Arm is mainly used for aerodynamic research. It consists of a counterbalanced arm at the end of which a model can be mounted. Thus, when the WA is running, the model moves in a circular path through a test passage. The test passage has a constant cross-section, 2.6 m wide and 3.30 m high. The inner wall has a continuous slot 0.75 m high along which the faired ends of the rotating arm pass. The radius of the model path is approximately 8.3 m. On the moving arm near its centre, provision is made to mount data acquisition equipment, pressure transducers and signal conditioning hardware. At the opposite end (opposite to the model) a pitot static tube is mounted to give information on dynamic pressure.

The arm is powered by a 70 hp electric motor, located on the ground near the axis of rotation and connected to it through a gearbox. It is fed by up to 600 V DC supplied by a dedicated motor-generator set. The maximum obtainable rotational speed is about 27 rpm, the usual speed for tests is around 25 rpm.

The hydraulic incidence-changing mechanism as used in the HIRM measurements is shown in Fig. 2.1 (Source : ref. 1). It was designed originally for mounting an ogive-cylinder body on the arm, as described in ref. 1. The mechanism is moved by a hydraulically operated jack. This incidence-changing mechanism is only for changing the incidence between the "steady state" test conditions and not for changing incidence during transient measurements.

When the model is mounted with the wing plane vertical, the rotation gives steady pitching motion, and with the wing plane horizontal the

rotation gives steady yawing motion.

The speed of the arm and the incidence position can be changed from a panel, in a separate control room located in the Whirling Arm building. This room also contains equipment for test supervision and data recording.

2.3 HIRM models and shroud

The models of HIRM I and II as tested on the WA have the RAE designation Model 2206 and Model 2254 respectively. (See Table 1.1 for a complete list of all HIRM models tested in the RAE high incidence research programme.) For the selection of the scale of the models relative to the free flight models, the following points were considered:

1. Weight of the model. Aerodynamic forces are to be measured in the presence of centrifugal forces and it is necessary to ensure that the latter are not so large that they mask the former. The aerodynamic forces are proportional to the square of the model scale. If the mean density of the model is constant, its weight and the centrifugal forces are proportional to the cube of model scale so that the larger the model, the lower the ratio of aerodynamic to centrifugal forces. However, with the techniques used in design and manufacture, the mean density is likely to become lower as the model scale is increased and this reduction in the ratio with increase of scale may not apply for the range of sizes under consideration.

2. Viscous effects. For a given speed (the maximum possible due to 25 rpm being about 22 m/s), the Reynolds' number increases with model size. The larger the model, the closer the Reynolds' number of the free flight tests will be approached.

3. The parameter $\frac{q \times \bar{c}}{V}$. For oscillatory tests this was called the "reduced frequency". For steady state tests on the Whirling Arm, this is the tangent of the angular difference in free stream velocity at two positions at distance R of the WA centre, and having a distance $\bar{c}$ between them. This factor can be called "Path Curvature Number" for steady state WA tests. In the Whirling Arm, where $q = \omega$ = angular velocity of the arm, we have:

$$\frac{q\bar{c}}{V} = \frac{\omega\bar{c}}{\omega R} = \frac{\bar{c}}{R} \qquad (1.1)$$

This factor is independent of speed and is determined only by the size of the model, since R is fixed. The size of the forces and moments due to rotation, to be derived from measurements will be proportional to this factor.

4. Blockage and constraint effect. The greater the model size, the higher the unconventional (in relation to wind tunnels) corrections, uncertain because of the shape of the test passage.

5. Manufacturing. With a scale of 2/9 or 4/9 (the scale of the other wind-tunnel models), manufacturing would be speeded up and simplified, especially if the WA models can be produced by moulding techniques when components of the existing models may be used as a "positive" shape from which a "negative" manufacturing mould can be made.

Considering the above-mentioned aspects, it was decided to build 4/9 scale models (HIRM I and II) with GRP skin and filled with polyurethane foam. Fig. 2.2 shows the general arrangement of the Model 2206 (drawn by Elven Precision Ltd.) and Fig. 2.3 the general arrangement of Model 2254 (drawn by T & E (Designs) Ltd.). The centre consists of a Carbonfibre Reinforced Plastic (CRP) tube, to which all lifting surfaces are attached. The model weight is about 15 lb. The leading edge of the wings have a "droop" of approximately 20°, simulating a slat deflection in a high-g manoeuvre. The wing shape is deflected slightly upwards (as the free flight model) as would result from distortion in a high-g manoeuvre. The models can be tested with or without a 5 hole nose probe (as described in Appendix 2.1). In the nose and in the tail of the models, provisions are made for mounting counterweights. These can be bolted firmly onto the CRP tube. (The function of the counterweights will be explained in Chapter 2.4.) The surface of the model is painted white, and polished to a smooth finish. As on the full scale and other models, no boundary layer transition control (*eg* "trip strips") is used. The fin and lifting surfaces were designed to be detachable. The angular settings of canard and tail surfaces are adjustable in discreet steps.

Stiffness tests were made on HIRM I trial-wings built in the same manner as the ones for the Model 2206. These tests simulated wing loadings due to centrifugal effects and due to aerodynamic lift. The wing deflections were believed to be small enough not to have a serious influence on the measurements of rotary derivatives.

The HIRM II model was supplied with the strakes and fences (Fig. 2.4), as also mounted on other wind-tunnel models. These were used to alleviate a severe loss in directional stability (too low value of N_v) over a particular incidence range, as described in ref. 20.

A shroud was made to be mounted completely surrounding the model, not touching any part of it or the balance, but attached to the sting behind the model (See fig. 2.3). This arrangement was required to make runs with only the centrifugal influence acting on the balance, without the aerodynamic forces (explained more in detail in Chapter 3). The shroud was built in a fairly simple way. The main material is plywood. The rear mounting for clamping on the sting is made of light alloy. For HIRM II, some aluminium sheet extensions had to be added to allow more space for the main wing and the canard surfaces, allowing the same component to be used with both models.

Figures 2.11 and 2.12 show the Model 2206 in the Whirling Arm test passage.

2.4 The strain-gauge balance

In a conventional strain-gauge balance for the measurement of aerodynamic forces on wind-tunnel models, there are two stations (distance apart = l) at which gauges are applied to respond to bending moments (Fig. 2.5). To find the applied force (F) and its line of action (l_p from the balance centre) it is assumed that the moments at both front and rear stations are due only to the applied force, so that:

$$\mathcal{M}_F = F\times(l_p - l/2) \tag{2.4.1}$$

$$\mathcal{M}_R = F\times(l_p + l/2) \tag{2.4.2}$$

$$F = \frac{\mathcal{M}_R - \mathcal{M}_F}{l} \tag{2.4.3}$$

$$l_p = \frac{\mathcal{M}_R + \mathcal{M}_F}{2F} \tag{2.4.4}$$

$\mathcal{M}_R$ and $\mathcal{M}_F$ are combined by connecting strain gauges into bridge circuits to produce signals proportional to $(\mathcal{M}_R - \mathcal{M}_F)$ and $(\mathcal{M}_R + \mathcal{M}_F)$, proportional to F and $F\times l_p$ respectively.

For the internal balance to be designed for the Whirling Arm tests, there is the problem that high centrifugal loads (≈ 6g environment at 8.3 m radius and 25 rpm) put high moment loadings on a conventional balance as described above. Together with the much lower aerodynamic forces (low speed tests, only ≈ 20 m/s at 25 rpm) there is a potential problem of measurement accuracy. (Note that there were no earlier experiments on the WA involving measurements of aerodynamic loads on aircraft models using an internal strain-gauge balance.) A possible way of improving accuracy was a means of balancing so that the moments due to inertia loadings acting on the strain-gauge stations remain low.

The balance was designed to have two strain-gauge stations. The centre of gravity of the model plus the front of the balance was to be roughly on the front station. Between the front and rear station, there was to be mounted a long arm extending rearwards carrying a counterweight to reduce the moment at the rear station due to centrifugal loads. A schematic picture of the balance and model assembly is given in figure 2.6.

For such a balance, different loading systems influence the front and rear stations, so their strain gauges cannot be combined as on a conventional balance described above. For that reason, moment- and force bridges can use strain gauges of one station only. The placement and wiring of the gauges can be found in Fig. 2.7 and 2.8. Note that the pitching and yawing moment gauges make use of the longitudinal extensions and contractions, and the shear force and rolling moment gauges make use of deflections due to shear forces. Because the measurement of an axial force component requires much more work in the balance design, construction and calibration, and because axial force was not considered vital information for the phenomena to be studied, no attempt has been made to measure it.

The scheme for the aerodynamic experiments was to include two runs for every test condition (model configuration, speed, angle of attack, angle of sideslip, etc.) : one with a shroud mounted over the model and one without this shroud. The shroud was to be mounted on the sting behind the model covering the model completely without touching it. Thus, no inertia loadings of the shroud would influence the balance. With the shroud mounted, only the inertia effects of the model and balance would be measured, and without shroud, the total (inertia + aerodynamic) loadings would be measured. Provided the balance interactions behave in a linear way the aerodynamic loadings can be computed by taking the difference between the "total" and "inertia" runs. These can be combined to give the aerodynamic forces and moments about a reference point because the same aerodynamic loading system acts on the front and the rear station. Note that it is not important if the centrifugal bending moments are not exactly "balanced". The residual moments can be deduced and removed to leave

the aerodynamic moments by the method described above. Because of the "balancing" of the front and rear stations, the errors associated with finding the small differences between measurements containing large centrifugal components will be eliminated.

However, the shear force bridges (measuring shear force in centrifugal direction) cannot be "balanced" by a similar method. Nevertheless, the shear force bridges were considered desirable in order to provide data for interaction corrections and were used only for this purpose. To investigate feasibility of measuring bending moments in the presence of large and uncertain shear forces, a trial balance was manufactured and subjected to appropriate tests.

Besides these tests on the trial balance, several other tests were made to investigate feasibility of the design as mentioned here.

The mathematical method to get the forces and moments at each station had to be established. Calibration loadings were needed to compute the interaction matrices. Two methods are described in Appendix 1. Mulkens' method, as mentioned in Appendix 1, (from now on designated the "new" prediction method), being a fairly straightforward one, will probably be used in all future tests. Ormerod's method, as also mentioned in Appendix 1, being used for all tests mentioned in this report, is a similar one (from now on called the "old" prediction method), although there are some rather complex prediction corrections involved which are not described in detail here. The old prediction method was considered to be sufficiently accurate. An impression of the precision of the predictions of both methods is also given in Appendix 1.

The manufacture of the balance was by the College of Aeronautics. After the decision was made as to how the strain gauges were to be located, their application and wiring was done by Welwyn Strain Measurement Ltd..

2.5 The pressure measuring system on the whirling arm

The noses of HIRM-Models 2254 and 2206 can be made suitable either to have a sharp apex or to mount a long 5-hole nose probe. This 5-hole nose probe has the same outline as that used on the free-flight models, except that the latter is used as a "Kiel-pitot" tube. The 5-hole nose probe was mounted (for some runs) on the Whirling-Arm models because:

- a probe was used on free-flight configurations which could have had significant effects on the aerodynamic characteristics of the model, especially at high incidence.
- to give more accurate information about the local flow qualities (*ie* the swirling movement of the air through which the model was passing).

The five-hole nose-probe as used in the WA tests (Fig. 2.2) can be used to measure local angle of attack, angle of sideslip, total pressure and airspeed, provided a suitable calibration is done. Since the flow characteristics of a steady three-dimensional flow are defined by four independent parameters, all the other parameters can be derived with these four. The calibration procedure as used for analysis of the WA tests described in this report was of a simplified nature. It was used to derive only angle of attack and dynamic pressure in longitudinal tests. The procedure is described in Appendix 2. This Appendix also describes aspects of multi-hole probe calibrations in general (as found in literature) and mentions a suggestion for future re-calibration of the same probe, in order to obtain all flow parameters.

Initially during the WA tests, there was no data taken from the nose-probe. The pressure measuring system is shown in Fig. 2.9. The free-stream airspeed was derived from the dynamic pressure from a pitot-static head on the opposite side arm. This takes into account the swirl speed at the pitot-static position. When it gradually became apparent that there was a form of swirl which was not uniform round the test passage (especially at high incidence), measurement of local flow was required. The nose probe was calibrated and its

pressures were recorded. For the longitudinal tests on HIRM I only one pressure transducer was available and the upper hole, central hole and lower hole pressures, referenced to the static from the pitot-static head, were each measured separately in repeated runs. For lateral tests on HIRM I and all tests on HIRM II 6 pressure transducers were used as shown in fig. 2.10.

The pitot-static probe as mounted on the opposite side arm (Fig. 66 ref. 1) is of a conventional type, and is mounted on the datum radius (8.306 m) in the middle of the test passage.

The differential pressure transducers as mentioned in Fig. 2.9 and 2.10 are of the type "Celesco LCVR", mounted on their demodulator board type "Celesco LCCD". The pressure range of the transducer is 0 - ±50 mm H_2O (0 - ±490.5 N/m^2). This dynamic pressure corresponds to an airspeed of 28 m/s with standard sea-level air density. With the arm running at 25 rpm, the nominal speed (*ie* 0 % swirl assumed) would be 21.74 m/s at the datum radius of 8.306 m, so the pressure range of the selected transducer should be suitable. Size, lagtime, accuracy and price of the transducer were acceptable. (More information about this can be found in Celesco's product catalogue.)

The demodulator board is basically a signal conditioning unit, amplifying the transducer outputs to a voltage level from -10 V to +10 Volt DC nominally.

The transducers and their demodulators are mounted near the centre of the arm. The transducers are mounted with membrane surfaces parallel to the radius, which decreases centrifugal effects. However, the manufacturer ensures that these effects, as well as vibration effects, should be minimal, due to an extremely thin membrane. Trials on the whirling arm to check for these influences confirmed this. Initially, when there was only one transducer, this had been mounted in error with its membrane normal to the radius. There was a small but significant centrifugal force effect for which corrections were made.

2.6 Instrumentation

The Midas Sirton computer used for digitising, assembling, displaying and recording data during the steady-state experiments of HIRM is the same as described in ref. 1, so an elaborate description of it will not be repeated here. The analog inputs were:

7 strain-gauge balance
5 nose-probe transducer
1 pitot/static transducer

The strain-gauge signals are low voltage and needed to be amplified. For this, the in-house designed and built signal-conditioning units (as described in ref. 1) were used. The cut-off frequency of the low-pass filters was 2 Hz, which seems to be appropriate for steady-state measurements. The amplification was adjustable, a factor of 960 was used for all channels on most of the tests. As mentioned earlier, the pressure transducers had their own signal-conditioner boards and their output was fed directly into the Midas Sirton computer.

3 Data reduction and analysis method

3.1 Introduction

In this Chapter, a general explanation of the data reduction methods is given. Often, examples are given for the longitudinal mode. It should be kept in mind that, where applicable, the analogous formulae can be used for the directional mode. Also, the new test rig to be used in future transient experiments, is called the "$\dot{\alpha}$-rig", although it can also be used to measure the "$\dot{\beta}$-effect".

In this report, the final results will be given in the form of normalized derivatives of forces and moments in the aero-system, rather than aerodynamic coefficient derivatives. The difference (mainly a matter of notation) is explained in ref. 10. The reason for adopting this form of notation is to keep compatibility with other work done on HIRM, *eg* as presented in ref 19. The form of notations is entirely explained in ref. 10. For the sake of convenience, the table depicting the divisors for obtaining normalized quantities is given in table 3.1. As an example, we define $\check{M}_q$, being non-dimensional, as :

$$\check{M}_q \equiv \frac{M_q}{0.5\rho V S \bar{c}^2} = \frac{\partial M / \partial q}{0.5\rho V S \bar{c}^2} \qquad (3.1)$$

Note that the representative length l_0 as stated in table 3.1, is equal to $\bar{c}$ for the longitudinal mode, and equal to b for the lateral mode.

3.2 General data reduction scheme

The data-reduction method employed to compute aerodynamic coefficients and aerodynamic stability derivatives from the signals is largely programmed. The general scheme for the longitudinal mode is given in Fig. 3.1. This figure shows what computer is used for particular computations. As can be seen, some computation is done by hand. Also, data transport from Superbrain in the WA building to the CoA VAX-750 is done by hand, which is quite laborious.

As Fig. 3.1 shows, for both the "top-out" and "top-in" position, the runs can be made with and without the shroud. Since for the shroud-off case the balance strain gauges are under centrifugal and aerodynamic loads, the sum of both effects will be represented in the shroud-off signals. When tested at the same attitude, but with the shroud mounted, only the centrifugal effect plays a role. In one of the programs written for the VAX-750 the difference of these effects is taken for the front and the rear stations of the balance. It should be noted that this difference should be calculated before combining the front and rear forces and moments since due to centrifugal loading, the loading systems acting on the front and rear gauge stations are different. The general method of computing the balance forces and moments is explained in more detail in Appendix 1.

For the shroud-on tests, only centrifugal loadings influence the balance gauges. For the purpose of computation, the "centrifugal" pitching moments and yawing moments of both front and rear station can be considered to behave as a second order polynomial as function of the geometric incidence, *eg* :

$$M_{i_{j_c}} = - a_{i_{j_0}} + a_{i_{j_1}} \times \alpha_{geom} + a_{i_{j_2}} \times \alpha^2_{geom} \qquad (3.2)$$

(i = top-in, top-out and j = front, rear)

The factors $a_{i_{j_k}}$ (k = 0, 1, 2) can be found by making just three runs at different incidences. The difference between the moments as

estimated according to (3.2) and moments measured at a larger number of incidences appeared to be acceptably small. For this reason, only three 'centrifugal' (shroud on) runs were required for each model roll position.

Apart from the methods as described above, the formulae for deriving the aerodynamic coefficients are relatively straightforward. The results of the data reduction programs are:

$$C_{\mathcal{L}_i},\ C_{\mathcal{M}_i},\ C_{\mathcal{N}_i},\ C_{Y_i},\ C_{Z_i},\ \text{with i = "top-in" or "top-out".}$$

Divisors for reducing data to coefficient form are: $1/2\times\rho V^2 S$ for forces, $1/2\times\rho V^2 S\bar{c}$ for pitching moments and $1/2\times\rho V^2 Sb$ for yawing- and rolling moments, thus conforming the notation standard as mentioned in ref. 10. It must be noted that the forces and moments thus found are relative to the geometric body axes rather than the aerodynamic body axes, as defined in ref. 10. When there can be any confusion about whether aerodynamic- or geometric body axes are meant, subscripts are used, resp. A and G. When no subscripts are given, the geometric body axes are meant, as is usual in most literature. Further, it should be noted that axial force is not calculated because of the reasons mentioned in Chapter 2.4. Because there is no axial force component it is not possible to compute lift coefficient. The reference centre for the moments can be freely chosen and the conversion formulae from one reference centre to the other may be applied in case a comparison with other than WA data needs to be made. The conversion formula for the longitudinal case is :

$$C_{\mathcal{M}_i}{}_{x_2} = C_{\mathcal{M}_i}{}_{x_1} + C_{\mathcal{N}_i} \times \frac{x_2 - x_1}{\bar{c}} \qquad (i = \text{top-in, top-out}) \qquad (3.3)$$

x_2-x_1 is the distance between the two moment reference centres. Formula (3.3) is also valid for $\frac{q\bar{c}}{V} \neq 0$, so it can be used for converting the whirling arm longitudinal results. The longitudinal results are presented grafically showing the variation of the coefficients with incidence. For each graph, the moment reference

centre is given. The moment reference centre used in the VAX-750 program, around which the moments are computed initially, must be taken equal to the "virtual" point of rotation (Fig. 2.1) (= centre of incidence rotation). This must be done because if a different point is taken, the "Path Curvature Number" $\frac{q\bar{c}}{V}$ will be changed by a (slight) amount: see (1.1) and Chapter 2.3. (Because, at most incidences, the radius to the MRC will be changed.) It should be noticed that the nominal incidence for a particular data point will also be changed if another moment reference centre is used.

The method for deriving M_q from the pitching moment coefficient is as follows : If we assume a linear relation between C_M and q for the range as expected on the Whirling arm, then we can state :

$$M_q = C_{M_q} = \frac{\partial C_M}{\partial\left(\frac{q\bar{c}}{V}\right)} = \frac{\Delta C_M}{\Delta\left(\frac{q\bar{c}}{V}\right)} = \frac{C_{M_{top\ in}} - C_{M_{top\ out}}}{(q_{top\ in} - q_{top\ out})\times\frac{\bar{c}}{V}} \qquad (3.4)$$

With $V = q_{top\ in}\times R$ and $q_{top\ in} = -q_{top\ out}$ we get :

$$M_q = \frac{\left(C_{M_{top\ in}} - C_{M_{top\ out}}\right)\times R}{2\bar{c}} \qquad (3.5)$$

3.3 Directional mode

For comparing different results of tests done in the directional mode, the necessary axis conversions can be more complex. For the directional tests on the whirling arm, it should be noted that the angular velocity due to the turning of the arm, is (apart from small angular discrepancies between the "geometric" arm speed and the airspeed, due to swirl) around the aerodynamic Z-axis rather than around the geometric Z-axis. (Again, definitions conforming ref. 10.) Especially at high incidences it is important to make conversions because the difference between aerodynamic and geometric body axes is considerable.

After measurement (by the WA strain-gauge balance) of the moments $\mathcal{L}_G$ and $\mathcal{N}_G$ from the WA directional mode tests with slip angle 0, we can make the following conversions to get the moments about aerodynamic body axes :

$$\left.\begin{aligned} (\mathcal{L})_A &= (\mathcal{L})_G\cos(\alpha) + (\mathcal{N})_G\sin(\alpha) \\ (\mathcal{N})_A &= (\mathcal{N})_G\cos(\alpha) - (\mathcal{L})_G\sin(\alpha) \end{aligned}\right\} \qquad (3.6)$$

(See Appendices A and B ref. 19.)
If we subsequently use the divisor to get the non-dimensional derivatives, (see table 3.1) we obtain:

$$\left(\check{\mathcal{L}}_r\right)_A = \frac{\left(\mathcal{L}_r\right)_A}{0.5\rho VSb^2} = \frac{\partial \mathcal{L}_A / \partial r}{0.5\rho VSb^2} \qquad (3.7)$$

Analogously, we obtain :

$$\left(\check{\mathcal{N}}_r\right)_A = \frac{\left(\mathcal{N}_r\right)_A}{0.5\rho VSb^2} \qquad (3.8)$$

$$\left(\check{Y}_r\right)_A = \frac{\left(Y_r\right)_A}{0.5\rho VSb} \tag{3.9}$$

Additionally, some preliminary data (directional mode) of the Acceleration Derivative Rig (ADR) as used by RAE Bedford is available. Graphs of $\left(\check{Y}_{\dot{v}}\right)_G$, $\left(\check{N}_{\dot{v}}\right)_G$, and $\left(\check{\mathcal{L}}_{\dot{v}}\right)_G$ as function of α will be presented. In order to make comparison with the earlier mentioned WA data useful, they have to be transformed to aerodynamic body axes:

$$\left.\begin{aligned}
\left(\check{Y}_{\dot{v}}\right)_A &= \left(\check{Y}_{\dot{v}}\right)_G \\
\left(\check{N}_{\dot{v}}\right)_A &= \left(\check{N}_{\dot{v}}\right)_G \cos(\alpha) - \left(\check{\mathcal{L}}_{\dot{v}}\right)_G \sin(\alpha) \\
\left(\check{\mathcal{L}}_{\dot{v}}\right)_A &= \left(\check{\mathcal{L}}_{\dot{v}}\right)_G \cos(\alpha) + \left(\check{N}_{\dot{v}}\right)_G \sin(\alpha)
\end{aligned}\right\} \text{via (B-3) ref. 19} \tag{3.10}$$

Also, values of $\left(\check{Y}_r-\check{Y}_{\dot{v}}\right)_A$, $\left(\check{N}_r-\check{N}_{\dot{v}}\right)_A$ and $\left(\check{\mathcal{L}}_r-\check{\mathcal{L}}_{\dot{v}}\right)_A$ are available, as obtained from table 3b ref. 19. These are obtained from the RAE Small Amplitude Oscillatory Rig (SAOR) tests. Combination of the ADR with WA data gives additional values of $\left(\check{Y}_r-\check{Y}_{\dot{v}}\right)_A$, $\left(\check{N}_r-\check{N}_{\dot{v}}\right)_A$ and $\left(\check{\mathcal{L}}_r-\check{\mathcal{L}}_{\dot{v}}\right)_A$. These data can be compared with the earlier mentioned SAOR data. Some non-compatibility is present due to different control surfaces deflections, so the comparison is difficult. The angles η_C and η_T will be mentioned in the graphs.

A comparison of WA with SAOR data can also be made for the sideslip derivatives $\check{Y}_v$, $\check{\mathcal{L}}_v$ and $\check{N}_v$. If we assume linear variation with v, r etc. then *eg* :
(for the geometric body axes:)

$$Y = Y_0 + Y_v \times v + Y_w \times w + Y_p \times p + Y_r \times r \tag{3.11}$$

The WA directional tests consisted of tests done at the nominal speed

of 25 rpm. A number of runs were made at β=-6°, β=0° and β=+6°, each at several incidences between 0° and 30°. With the assumption that (3.11) is valid, we can thus state, for one test series at constant incidence :

$$r = \text{constant}$$
$$p = \text{constant}$$
$$w = \text{constant}$$

Hence, the difference in side-force must be entirely due to the change in sideslip angle. Hence, we compute from the measured forces and moments (geometric body axes !) :

$$\left.\begin{aligned} \check{Y}_v &= \frac{\partial C_Y}{\partial \beta} = \frac{C_{Y_{\beta=6^\circ}} - C_{Y_{\beta=0^\circ}}}{6\times\pi/180} \\ &\text{and analogously :} \\ \check{\mathcal{L}}_v &= \frac{\partial C_{\mathcal{L}}}{\partial \beta} \\ \check{N}_v &= \frac{\partial C_N}{\partial \beta} \end{aligned}\right\} \qquad (3.12)$$

(Obviously, since the tests are taken at β=-6°, 0° and +6°, the difference in derivatives for positive and negative slip angle can be investigated.) Because of the small slip angles, sin(β) and cos(β) conversions to get back to the model plane of symmetry are neglected here. From SAOR tests, we also have available : $\left(\check{Y}_v\right)_G$, $\left(\check{\mathcal{L}}_v\right)_G$ and $\left(\check{N}_v\right)_G$ (table 3a ref. 19.) Hence, WA and SAOR data on v-derivatives can be readily compared. (A comparison of SAOR with static data on v-derivatives of HIRM I has been made in ref. 19.)

3.4 Additional notes

It should be kept in mind that the aerodynamic angle of attack α_{aero} was not obtained for all runs. It was only after the results from some runs had indicated unexpected variations of the swirl flow that the nose probe pressures were recorded. In the results presented it will be shown which angle of attack (aerodynamic or geometric) has been used.

As mentioned in Appendix 3, corrections are necessary to the dynamic head obtained from the nose probe due to differences between the path radii of the tip of the probe and the moment reference centre, which vary with model incidence. It can be shown that these corrections are of significant magnitude and they are therefore taken into account in the data-reduction process.

Due to the centrifugal loading, the sting incidence-changing mechanism was affected slightly, in that the indicated incidence at rest was different from that at 25 rpm. For that reason the incidence was only measured when the WA is at the speed for the test. The aforementioned effect was considerable during the early phase of testing, and needed serious consideration. After welding in an extra steel member on the WA structure, it was reduced greatly. All measurements used for the final analysis of results were made after the attachment of this member.

The sting deflection as a result of the 6-g environment cannot be measured during running of the WA. Therefore, the output of the linear transducer (used for the geometric incidence measurement) is corrected, using the balance loads and stiffness characteristics (not covered in detail here) measured during tests with the balance mounted on the calibration rig. Of course, when measuring the angle of attack with nose probe, this correction is not necessary.

One of the unfortunate restrictions when using the WA for aerodynamic experiments is that one can only test at Reynolds' numbers low in

comparison with normal wind-tunnel tests. Calculations of the Reynolds' numbers for the HIRM I and HIRM II Models (2206 and 2254) tested at 25 rpm are shown below:

$$V = 2\pi Rn = 2\pi \times 8.306 \times \frac{25}{60} \text{ m/s} = 21.7 \text{ m/s}$$

HIRM I; $\bar{c} = 0.386$ m

$$\Rightarrow Re_{\bar{c}} = \frac{V\bar{c}}{\nu} = \frac{21.7 \times 0.386}{1.4607 \times 10^{-5}} = 5.7 \times 10^{5} \qquad (3.13)$$

HIRM II; $\bar{c} = 0.560$ m

$$\Rightarrow Re_{\bar{c}} = \frac{V\bar{c}}{\nu} = \frac{21.7 \times 0.560}{1.4607 \times 10^{-5}} = 8.3 \times 10^{5} \qquad (3.14)$$

These Reynolds' numbers are much smaller than those of other HIRM wind-tunnel results. To make a confident comparison of WA results with other results, we must know how important the scale-effect is. Some information was obtained by testing the HIRM I, Model 2206 in the RAE-Bedford 13' x 9' wind tunnel at two different Reynolds' numbers:

$$Re_{\bar{c}} = 5.0 \times 10^{5} \text{ and } Re_{\bar{c}} = 1.1 \times 10^{6}$$

The lower number is in the region of the WA tests and the higher number in the region of a number of different wind-tunnel tests, as done at RAE Bedford and Farnborough. The results of these 13'x9' "comparison tests" appeared to be encouraging and they are shown in Chapter 4.2. Additionally, a comparison is made between the high-Reynolds' number ($Re_{\bar{c}} = 1.1 \times 10^{6}$) tests of the Model 2206 with higher-Reynolds' number tests ($Re_{\bar{c}} = 1.9 \times 10^{6}$) of the Model 2130, also in the RAE 13'x9' tunnel. Unfortunately, because of strength considerations, it was not possible to test Model 2206 at the high Reynolds' number 1.9×10^{6}.

For all tests, ambient pressure and temperatures were measured, in order to derive the air density (See Appendix 3). Measurement of air humidity was not considered necessary.

4 Results and discussion

4.1 Introduction

The results of WA measurements mentioned in this Chapter are presented mainly in graphical form. This presentation adequately shows the main aerodynamic properties of the models. The numerical form of this data is stored in computer files and hence, remains available.

This Chapter is divided in several parts describing different areas of investigation. Where appropriate, the results of WA measurements have been compared with other dynamic wind-tunnel tests, as done with the SAOR, LAPR or ADR facilities of RAE Bedford.

Directional WA results of HIRM II are not yet available, but it should be noted that such tests (both steady-state and transient) can be made with the new test rig, currently under development for future transient experiments.

During the first five years of this work the emphasis was on developing techniques and verifying the quality of test data rather than accumulating results for the range of different configurations available of the Whirling Arm models of HIRM I and II. Only tests with $\eta_C = \eta_T = 0^\circ$ were carried out. While these selected control surface angles give good opportunities for comparison with wind-tunnel data, it should be noted that in the future, if time permits, more configurations can be tested.

4.2 HIRM I wind-tunnel results

As mentioned in Chapter 3, HIRM I was tested in the RAE 13'x9' wind tunnel to investigate the importance of scale effect. Only the main results are shown here, in the form of Figures 4.1, 4.2 and 4.3. They show the pitching moment-, axial force- and normal force-coefficient respectively. The airspeeds corresponded to the Reynolds' numbers:

$$Re_{\bar{c}} = 5.0 \times 10^5 \quad \text{and} \quad Re_{\bar{c}} = 1.1 \times 10^6$$

for Model 2206, the light-weight model as used in the WA tests. For the comparison with Model 2130, the results for the latter model are shown, at Reynolds' number:

$$Re_{\bar{c}} = 1.9 \times 10^6$$

Axial force, although not included in the Whirling Arm tests, was included in the wind-tunnel comparisons because its variation shows very clearly the incidence at which separation starts on the leading edge of the wing. This is the point at which the axial force stops falling as the incidence increases.

Looking at these figures, we see that no apparently significant scale effect is present, at least not between the Reynolds' numbers covered in the tests. Only the pitching moment and axial force at higher incidences show some differences.

There is difficulty in isolating the effects associated with Reynolds' number and the viscous boundary layer flow, from effects of aeroelastic distortion, as increased Reynolds' number is accompanied by an increase in dynamic head and increase of the actual aerodynamic load acting on the model at a given incidence. Aeroelastic effects would have been potentially more serious on the light-weight and comparatively flexible Whirling Arm model.

The very limited scale effect between the low Reynolds' number tests (as on the WA) and the higher Re number tests (as expected in the

free-flight trials) as well as the limited influence due to different models gives confidence in the data to be obtained from the WA tests. However, interpretation of the WA data should be done with care, because :

1. There may possibly be a scale effect for steady curved flows, not shown by the straight-flow comparisons, though this is felt to be unlikely as the types of flow over the model will not be dissimilar. A little work was done on the Whirling Arm at lower Arm speeds and showed no evidence of any major difference in the computed force and moment coefficients.
2. The turbulence levels in the WA (partly associated with swirl) may influence the boundary layer flows over the Whirling Arm model. As such turbulence is not present in free-flight and may be less severe and of different character in wind tunnels, comparisons must be made with turbulence effects in mind.

4.3 HIRM I longitudinal results

Fig 4.4 shows normal-force coefficients as a function of incidence for both top-in and top-out attitudes. The wind tunnel results are also shown. These Whirling Arm data are from early tests and gave strong indications that the experimental technique was unsatisfactory. It was difficult to visualize the aerodynamic behaviour of the model that would produce such variations of normal force, especially the inflection of the top-out curve between 8° and 12°. The wind-tunnel curves were expected to be between the top-in and top-out curves but at higher incidences this was not the case. At the lower incidences these results show the rotation to have little influence on normal force.

Fig 4.5 shows the pitching moment coefficients found from the same runs. Here, pitching angular velocity is shown to have more influence. The straight-flow result from the wind tunnel is between the curves for positive and negative q, as expected. There is no outstanding inconsistency in these curves.

The dynamic head, obtained from the pitot-static on the opposite arm and used in the computation of these coefficients, is shown by the curves of Fig 4.13, labelled "without flap". As the top-out incidence increases there is a gradual decrease of the dynamic head followed by a sharp increase between 7° to 13°, in the same region as the inflection of the top-out normal-force curve.

The unexpected normal-force curves strongly suggested an investigation to obtain a better understanding of the swirl flow. The speed of the swirl flow can be found as the difference between the known speed of the pitot-static tube through space and the speed through the air indicated by the pressures from the instrument in a known air density. An increasing dynamic head corresponds to a decreasing swirl speed. As a percentage of the speed through space, the swirl is indicated by the scale on the left-hand side of Fig 4.13. Many tests were made to find more details of the swirl flow affecting the model, especially in its top-out attitude where the

variations of the swirl flow appeared to be associated with the unacceptable normal-force curves. The cause of the obviously undesirable change of the swirl flow within the test incidence range and possible remedies were also investigated.

The work of improving the measuring technique to produce more plausible results in the presence of the changing swirl flow eventually involved using the model nose probe to assess both the dynamic head of the airflow relative to the model and also its direction. The calibration of the 5-hole probe in the Weybridge Tunnel is described in Appendix 2. For the immediate requirement of providing data for the top-in and top-out runs, the calibration was limited to cover an incidence variation at zero sideslip, taking pressures only from the top, centre and bottom holes. "Top" and "bottom" were relative to the model rather than to the hole positions in space. In using data from the nose probe, corrections were made to both incidence and dynamic head to convert these quantities measured at the tip of the probe to apply to the reference point of the model. The corrections were, to a small extent, dependent on the assumption, not strictly correct, that the swirl was always in a tangential direction, with a velocity proportional to the radial distance from the centre of the Arm.

The data from the nose-probe measurements is included in Fig 4.13, again labelled "without flap". Like data from the pitot-static, the nose-probe dynamic head shows a gradual decrease followed by sharp increase over the top-out incidence range from 7° to 13°. The new effect shown by the nose-probe data is the change of aerodynamic incidence due to the swirl flow. With the model in the top-out attitude, the aerodynamic incidence is 2° greater than the geometric incidence at a geometric incidence of 7° and 1° less than the geometric incidence at 13°. Using the dynamic head and aerodynamic incidence derived from the nose-probe, the inflection in the top-out normal-force curve is almost eliminated, as shown in Fig 4.9. The curve showing the previous normal-force variation is shown for comparison. Later test had shown some hysteresis in the inflection region, as indicated on the figure.

In parallel with the work associated with the nose probe to provide more data on the unexpected swirl variation tests were made to find its cause. Fig 4.6 gives the variation of dynamic head measured in tests with the shroud mounted; (there was no requirement for this pressure data in the assessment of the centrifugal loads on the balance). There is a decrease in dynamic head as the incidence of the very bluff shape is increased in the top-out attitude, with a possible tendency to increase at the highest incidence. This had a slight resemblance to the variation from tests on the clean model but with the point of the dynamic head rise possibly delayed to an incidence beyond the test range.

It was suggested that the dynamic head variation may have been due to a Reynolds' number effect with perhaps a change of flow separation from the fairings round the model support, induced by the change of model incidence. Some measurements were available from which the data of Fig 4.8 were prepared. These show that the normal force and pitching moment coefficients from an Arm speed of 12 rpm, at half the standard Reynolds' number, were substantially the same at those at 25 rpm, with the same inflection in the normal force curve. (This comparison supports the result from the wind tunnel tests that the aerodynamic characteristics of the model are little affected by changes of Reynolds' number, even at levels which are low in comparison with those of normal wind tunnel tests.) Measurements were made with vortex generators mounted on the model-support fairing, possibly modifying separations induced by the model wake, but there was no change in the measured variation of dynamic head.

Some limited attempts at visualization of the swirl flow were made using tufts and smoke but they did not show anything to throw extra light on the phenomenon. It was realized that more equipment would be required to make this type of visualization more effective, such as a television camera mounted on the moving Arm, and this would have involved more time and effort than were available at this stage of the work.

The change of aerodynamic incidence accompanying the change of dynamic head suggested that the swirl was influenced by flow through the slot in the inner wall of the test passage. This flow, at the model position and behind the end-plate fairing, appeared to be modified by the incidence of the model, with a major change in the flow pattern as the top-out incidence increased from 7° to 13°. It was considered that, if the flow into and out of the test passage could be modified, it might be possible to arrange that there was no critical change in the flow pattern within the incidence range of the model tests. Trials were made with a split flap attached to the trailing edge of the end-plate fairing, either on the model side or on the side towards the centre of the Arm, Fig 4.7. Various angles were tried and results are presented for an apparently successful arrangement with flap on the model side, set at 32°. The dynamic head measurements and the change of model incidence due to the swirl flow are shown in Fig 4.13. The sudden increase of dynamic head has been eliminated though there were gradual changes of dynamic head and swirl-flow direction which were more pronounced for the model in the top-out than the top-in attitude. The normal-force and pitching-moment curves for the top-in model attitude are shown in Figs 4.10 and 4.11. The presence of the flap has introduced no irregularities into these curves. The difference between the coefficients, with and without the flap, however, is rather disappointing, suggesting that further refinements in the test technique are desirable. These could be in the ways of obtaining the aerodynamic incidence and the dynamic head to be associated with the force and moment measurements, and perhaps, more fundamentally, by considering how the non-uniform swirl flow can change the effective rate of rotation.

Fig 4.12 shows the variation of $\check{M}_q$ with incidence. Two sets of Whirling-Arm values are included: one from early tests using geometric incidence and dynamic head from the pitot-static on the opposite arm and the second from data obtained using incidence and dynamic head from the nose probe. The second set was from tests with the flap on the trailing edge of the end plate fairing and probably represents the most reliable result so far. The first set is included

to show data of a standard similar to those of HIRM II, covered in the next section.

There is only a small difference between the two sets of $\check{M}_q$, obtained from the pitching moment coefficients, top-in and top-out. The differences between derivatives from normal force measurements would have been far greater.

In the Figure, the Whirling-Arm $\check{M}_q$'s are compared with values of the combined derivative $\check{M}_q + \check{M}_{\dot{w}}\cos\alpha$ obtained from SAOR tests (ref 19). When comparing these results one must bear in mind that the tail plane angle for the SAOR tests was not zero but at settings indicated on the figure, to limit the load on the sting. $\check{M}_q$ is shown to be almost independent of incidence and close to the combined derivative below 18°. Between 18° and 26° the combined derivative shows a pronounced dip, in effect doubling the pitch damping. There is no similar dip shown by the Whirling-Arm data and it may be concluded that the dip is associated with the $\dot{w}$ in the second part of the combined derivative. The investigation of the influence of $\dot{w}$ (also referred to as the $\dot{\alpha}$ effect) will be the subject of further work in the Whirling-Arm facility.

4.4 HIRM II longitudinal results

The elaborate swirl investigation as described in Chapter 4.3 was not repeated for the HIRM II runs. The main reason for this was lack of time. It should be noted also that the new test rig currently under development (as will be described in future reports), will enable all steady state tests to be repeated. With the new software incorporated for data acquisition, computing and recording, it will be much quicker to analyse all data, so rather than spend time with the old and laborious methods, it appears wiser to use the new system in the future.

Only the main results for HIRM II longitudinal tests are presented here. Figure 4.14 gives the pitching moment coefficients as function of α_{geom}. It also shows the straight-flow data (q = 0) as obtained from ref. 20. Figure 4.15 shows M_q as function of α_{geom}, as obtained from figure 4.14 and applying formula (3.5). Also, it shows the combined derivative $M_q + M_{\dot{w}} \times \cos(\alpha)$ as obtained from the RAE, Bedford oscillatory tests, with the LAPR facility. (Source : ref. 20.)

In the above-mentioned figures, α_{geom} is used rather than α_{aero} as obtained from the nose-probe. The nose probe was mounted in all HIRM II Whirling Arm tests, and the pressures were recorded. However, the unfamiliarity of the new system-user with the nose probe data-reduction methods prevented using them. It should be noted that, in principle, it is possible to get higher quality aerodynamic coefficients with the present data, by using dynamic head and incidence obtained from the nose probe, but for the reasons mentioned, it is better to do this with the new system.

It should also be noted that the nose probe as used on the HIRM II Model 2254 for WA tests is the same one as mounted on the HIRM I model. As mentioned in various literature, a sharp-pointed nose can result in asymmetric forces and moments for β=0 at high angles of attack. Considerable hysteresis can be observed in some coefficient curves. These phenomena are probably not present in WA tests due to the presence of the nose-probe.

Looking at fig. 4.14, there is no sudden change in C_M as function of α, as might result from an adverse swirl phenomena such as mentioned in Chapter 4.3. The fairly constant differences between the coefficients for top-in and top-out attitudes result in a smooth $\check{M}_q$ curve : see fig. 4.15. This curve does not show the sudden "spike" as in the LAPR results. This spike, apparently resulting from a HIRM II $\dot{\alpha}$-effect, gives a considerable decrease in damping-in-pitch, at $\alpha \cong 17^\circ$ to 20°. The exact cause of these $\dot{\alpha}$-effects is not yet understood. They justify the manufacture of the earlier mentioned test rig, called the "$\dot{\alpha}$-rig". This will provide alternative measurements of the $\dot{\alpha}$-effect which will give more certainty about its nature and magnitude. In attempting to understand the present results, the following questions arise:

- Why is the main $\dot{\alpha}$-effect on HIRM I stabilizing and on HIRM II destabilizing? (*ie* more and less damping in pitch, respectively.)

- Why do the main $\dot{\alpha}$-effects for both models exist only in a particular angle of attack range?

To answer these questions, it is probably necessary to consider the interactions between the lifting surfaces. This will be done after the WA $\dot{\alpha}$-experiments have been carried out. It may also be necessary to use additional experimental techniques (*eg* flow visualization) before these questions can be answered satisfactorily.

4.5 HIRM I directional results

The directional tests of HIRM I were done with the model's Y-axis horizontal. Again, the control-surface deflections η_C and η_T were equal to 0° for all tests. The 5-hole nose probe was mounted and its pressures were recorded but no use has been made of this information because, as mentioned earlier, no suitable calibration data for $\beta \neq 0$ was available.

Only top-up tests, corresponding to $r<0$, have been made. Due to arising health problems during these tests, they could not be completed with top-down model-attitude. It should be noted however, that like other steady-state tests, these can be carried out in the future with the transient test rig as mentioned earlier.

The numerical results of sideforce coefficient, yawing moment coefficient and rolling moment coefficient as function of α_{geom} are given in Table 4.1. The results for $\beta_{geom} = -6^\circ$, 0° and $+6^\circ$ have been obtained by interpolation of measurements covering a range of angles. When a suitable nose probe calibration is available, it will be possible to calculate aerodynamic side slip angles, β_{aero}.

Again, the presentation is mainly graphical for ease of assessment.

Yawing angular velocity derivatives :

The values of the derivatives due to angular velocity r (around the aerodynamic body-axis) as obtained from SAOR- (source : ref. 19) as well as combinations of WA- and ADR data (source : ref. 21) is shown in fig. 4.16 through fig. 4.18. The procedure of deriving these curves is mentioned in Chapter 3. Although the comparison is difficult to make, due to different control surface deflections, we see reasonably good comparison in fig. 4.17 and 4.18. The usual sign of $\check{N}_r$ is negative, and the usual sign of $\check{\mathcal{L}}_r$ is positive, both conforming to the results. There seems to be a discrepancy in fig. 4.16 between WA- and the other results. The sign of $\check{Y}_r$ is

usually positive. (Although the absolute value of $\left(\check{Y}_r\right)_{WA}$ is not very high.) The discrepancy cannot be explained at the moment.

Sideslip derivatives :

Comparison of SAOR- with WA data on sideslip derivatives can be readily done (as explained in Chapter 3) and the results are shown in fig. 4.19 through 4.21. For the WA tests, we see slight difference in the results for positive and negative sideslip. This difference might decrease when proper sideslip measurement is available with the re-calibrated noseprobe. The usual signs for $\check{Y}_v$, $\check{\mathcal{L}}_v$ and $\check{N}_v$ conform with the WA results, except for high angles of attack, where $\check{N}_v$ becomes negative, indicating directional instability. This high-α effect conforms the SAOR results. In spite of the fact that the WA steady state motion is fundamentally different from the SAOR tests, the agreement between the results of $\check{Y}_v$, $\check{\mathcal{L}}_v$ and $\check{N}_v$ is encouraging.

5 Conclusions and recommendations

Conclusions :

1. Using the Cranfield Institute of Technology Whirling Arm facility for measurement of stability derivatives of High Incidence Research Models has been shown to give useful results.
2. Due to the Whirling Arm environment with its typical problems (swirl, aerodynamic and mechanical noise, low airspeed, high inertia loads), careful thought has been given to the design of the balance, the reduction of swirl and the data acquisition- and analysis method.
3. The investigation of the phenomenon of non-uniform swirl proved to be particularly time-consuming. Nevertheless this investigation was thought to be necessary in order to find ways to reduce the interaction of model attitude and swirl, and thus improve the uniformity of the flow and the quality of the aerodynamic data to be obtained.
4. Rotary derivatives varied smoothly with incidence without the spikes shown by measurements of the combined derivatives, measured on oscillatory rigs, which included the $\dot{\alpha}$ or $\dot{\beta}$-effects.

Recommendations :

1. The apparent $\dot{\alpha}$-effects (and, to lesser extent, $\dot{\beta}$-effects) as obtained from comparisons of Whirling Arm with oscillatory results, need to be investigated further, in order to gain more information about the precise nature of these effects and their magnitude. Their significance in the design of a flight control system will be clarified.
2. These effects can be measured with different combinations of the angular velocity effects and with model movements unlike those of oscillatory rigs by making use of a specially designed test-rig, to be installed on the Whirling Arm.
3. In order to assure the aerodynamic data to have high enough quality, careful validation has to be carried out of the experimental techniques, in particular the data acquisition- and reduction methods. The design and calibration of the strain-gauge balance and other aerodynamic sensors is also important.

4. In the long term, considerations should be given to ways of improving the Whirling Arm as an aerodynamic tool. Cutting down the swirl flow into and out of the test passage by reducing the width of the slot in the inner wall, or perhaps sealing it, could be very beneficial.

References

1. D.I.T.P. Llewelyn-Davies: The use of the College of Aeronautics' Whirling Arm Facility to determine the effect of flow curvature on the aerodynamic characteristics of an ogive-cylinder body. Ph.D. Thesis, Cranfield Institute of Technology, College of Aeronautics, July 1987.

2. P.R. Ashill, E.W. Osbourn : Calibration of the flow in the channel of the whirling arm. Cranfield Institute of Technology, College of Aeronautics, CoA Note Aero No. 177, October 1969.

3. A.O. Ormerod: Report on Progress and Planning of the Research Agreement on Rotary Derivatives of a High-Incidence Research Model (HIRM) using the Whirling Arm. - (Research Agreement AT/2028/0143.) September 1986. (Unpublished)

4. G.F. Moss, A.Jean Ross, G.F. Butler : A program of work on the flight dynamics of departure using a high incidence research model (HIRM). RAE TM Aero 1950, Royal Aerospace Establishment, Farnborough, July 1982.

5. C.O. O'Leary : Dynamic tests on a high incidence Research Model (HIRM) in a low speed wind tunnel. RAE TR 84111, Royal Aerospace Establishment, Farnborough, November 1984.

6. A. Jean Ross, G.E.A. Reid : The development of mathematical models for a high incidence research model. Part I : Analysis of static aerodynamic data. RAE TR 83037, Royal Aerospace Establishment, Farnborough, April 1983.

7. Geraldine Edwards, E.B. Jeffries : Free flight trials of RAE research models, HIRM 1 and HIRM 2, at NASA Ames / Dryden, October to December 1986. RAE TM Aero 2119, Royal Aerospace Establishment, Farnborough, January 1988.

8. A.R.G. Mundell : Low speed wind-tunnel tests on the use of airjets to control asymmetric forces and moments acting on aircraft at high incidences. RAE TM Aero 1984, Royal Aerospace Establishment, Farnborough, January 1984.

9. D.W. Bayer, D.E. Walshe, H.C. Garner : Pressure probes selected for three-dimensional flow measurement. ARC R&M No. 3037, 1985. 1975.

10. H.R. Hopkin : A scheme of notation and nomenclature for aircraft dynamics and associated aerodynamics. ARC R&M No. 3562, 1970.

11. G.J. Voerman : Handleiding voor het gebruik van de vijf-buis meetsonde voor de bepaling van de snelheidscomponenten en de totale-druk in een onbekende stroming. Delft University of Technology, Faculty of Aerospace Engineering, Memorandum M-259, December 1976. (In Dutch.)

12. E.M. Houtman, W.J. Bannink : The calibration and measuring procedure of a five-hole hemispherical head probe in compressible flow. Delft University of Technology, Faculty of Aerospace Engineering, Report LR-585, April 1989.

13. Archibald R. Sinclair, A. Warner Robins : A method for the determination of the lag in pressure measuring systems incorporating capillaries. NACA TN 2793, September 1952.

14. Hans Weidemann : Inertia of dynamic pressure arrays. NACA TM 998, 1942.

15. J.M. Kendall : Optimized design of systems for measuring low pressures in supersonic wind tunnels. AGARD Report 174, March 1958.

16. K.N. Everett, A.A. Gerner, D.A. Durston : Seven-hole cone probes for high angle flow measurement : Theory and calibration. AIAA Journal 1983, Vol. 21, No. 7, pp. 992-998.

17. C.L. Lawson, R.J. Hanson : Solving least squares problems. Prentice-Hall, New Jersey, 1974.

18. Alan Pope, Kenneth L. Goin: High-speed Wind-Tunnel Testing. John Wiley and Sons, Inc., June 1965.

19. A. Jean Ross, G.E.A. Reid : The development of mathematical models for a high incidence research model. Part II : Analysis of dynamic test data. RAE TR 84072, Royal Aerospace Establishment, Farnborough, July 1984.

20. C.O. O'Leary, E.N. Rowthorne : Low speed dynamic tests on a canard configured High Incidence Research Model (HIRM 2). RAE TR 88024, Royal Aerospace Establishment, Farnborough, December 1987.

21. C.O. O'Leary : Preliminary results of HIRM I directional mode tests on the RAE Acceleration Derivative Rig. -unpublished.

Appendix 1 Loading prediction methods and balance calibration procedures

For the steady-state experiments as mentioned in this report, an internal strain-gauge balance was used, designed by A.O. Ormerod. Strain gauges are mounted on two different stations of this balance, and an internal counterweight is mounted between these stations and in the model to compensate for most of the centrifugal loads when the arm is running. To acquire knowledge about balance calibration in general and to understand the behaviour of this balance in particular, it was considered useful to carry out a re-calibration of it. Besides these motives, it was necessary to check whether or not the characteristics of the balance had changed, after it was possibly subjected to high loads in trials of an arrangement for future tests of the $\dot{\alpha}$ effect.

Calibration of a strain-gauge balance involves applying different (known) loads on the balance and reading the strain-gauge outputs for each loading. Hence, one attempts to define a relation between these signals and the applied loads, in order to assess the loads acting on the balance when it is actually in use.

The balance contains four strain-gauge bridges at the front station and three at the rear, giving the primary signals of:

Front:	Rear:
pitching moment	pitching moment
yawing moment	yawing moment
normal force	normal force
rolling moment	

Since manufacturing of the balance or applying the gauges can never be done perfectly, the separate signals of the various channels are not sufficient to assess the particular loading, *eg* with other loads present, we cannot estimate the pitching moment about the front

station accurately enough with only the front pitching moment signal. However, it was proposed to use every signal (of a particular station) to calculate a certain loading. We can define a matrix for the front and the rear station, describing the relation between the signals and the applied loads.

Front station:

$$\begin{pmatrix} m_{11} & m_{12} & m_{13} & m_{14} \\ m_{21} & m_{22} & m_{23} & m_{24} \\ m_{31} & m_{32} & m_{33} & m_{34} \\ m_{41} & m_{42} & m_{43} & m_{44} \end{pmatrix} \times \begin{pmatrix} s_p \\ s_y \\ s_n \\ s_r \end{pmatrix} = \begin{pmatrix} l_p \\ l_y \\ l_n \\ l_r \end{pmatrix} \qquad \text{(A1.1)}$$

or: $\quad M \times \underline{s} = \underline{l}$

with s_i, i = p, y, n, r being the primary signals of, respectively, the pitching moment, yawing moment, normal force and rolling moment and l_i being the corresponding loadings.

The analogous equations for the rear station are :

$$\begin{pmatrix} \mu_{11} & \mu_{12} & \mu_{13} \\ \mu_{21} & \mu_{22} & \mu_{23} \\ \mu_{31} & \mu_{32} & \mu_{33} \end{pmatrix} \times \begin{pmatrix} \sigma_p \\ \sigma_y \\ \sigma_n \end{pmatrix} = \begin{pmatrix} \lambda_p \\ \lambda_y \\ \lambda_n \end{pmatrix} \qquad \text{(A1.2)}$$

or: $\quad \Omega \times \underline{\sigma} = \underline{\lambda}$

So, calibration involves the assessment of the matrices M and Ω. Since s_i is the main signal determining the load l_i, we call s_i the primary signal for determining l_i, and s_j ($j \neq i$) the secondary. As a result, we expect m_{ii} to be considerably bigger than m_{ij} ($j \neq i$). Hence, we call m_{ii} the primary matrix factors and m_{ij} ($j \neq i$) the secondary.

The analogous assessment is valid for the rear station.

The matrix multiplications given here imply that we consider the strain gauges to be linear, *ie* all signals vary linearly with the loadings. Observation of the signals for all loadings during calibration has justified this proposition. (Note that when too high loadings are applied, this may prove to be untrue. Since the expected loads on the balance are all within the calibration range, no non-linear effects are expected.)

A.O. Ormerod's method :

His method for deriving the matrices involves usage of very few calibration loadings only. It uses a "least square" curve fitting technique finding the linear variation of all component signals with the applied loads. This technique showed that factors other than those included in the matrices shown above needed to be taken into account and a correction was applied involving rolling moment loadings used for the rear station. Besides that, a horizontal shear correction for both front and rear stations was used. (Note that there are no horizontal shear (side force) bridges on either front or rear stations. Hence, an estimation of the horizontal shear had to be made using front and rear yawing moments.) With these corrections applied, the method appeared to be satisfactorily accurate.

M. Mulkens' method :

It was felt useful to incorporate more loadings into derivation of the matrices in order to get a more accurate result, without using the horizontal shear and rolling moment corrections. The derivation can be done in a direct and an indirect way. The principle of the indirect way is described in Chapter 7:10 of ref. 18.

Indirect method :

The magnitude of each channel's signal is a result of all loadings (on that particular station). *eg* For the rear station:

$$\begin{pmatrix} \sigma_p \\ \sigma_y \\ \sigma_n \end{pmatrix} = \underbrace{\begin{pmatrix} \omega_{11} & \omega_{12} & \omega_{12} \\ \omega_{21} & \omega_{22} & \omega_{23} \\ \omega_{31} & \omega_{32} & \omega_{33} \end{pmatrix}}_{\equiv \chi = \Omega^{-1}} \times \begin{pmatrix} \lambda_p \\ \lambda_y \\ \lambda_n \end{pmatrix} \qquad \text{(A1.3)}$$

To find the factors ω_{1j}, j = 1,2,3 we can write:

$$\sigma_p = (\omega_{11}\ \omega_{12}\ \omega_{13}) \times \begin{pmatrix} \lambda_p \\ \lambda_y \\ \lambda_n \end{pmatrix} \qquad \text{(A1.4)}$$

Since all m calibrations have to satisfy this equation, we can write:

$$\begin{pmatrix} \lambda_{p,1} & \lambda_{y,1} & \lambda_{n,1} \\ \lambda_{p,2} & \lambda_{y,2} & \lambda_{n,2} \\ & \vdots & \\ \lambda_{p,m} & \lambda_{y,m} & \lambda_{n,m} \end{pmatrix} \times \begin{pmatrix} \omega_{11} \\ \omega_{12} \\ \omega_{13} \end{pmatrix} = \begin{pmatrix} \sigma_{p,1} \\ \sigma_{p,2} \\ \vdots \\ \sigma_{p,m} \end{pmatrix} \qquad \text{(A1.5)}$$

or: $\quad A \times \underline{x} = \underline{b}$

Note that $\sigma_{p,i}$ and $\lambda_{j,i}$ are known for all i = 1,2,....m and j = p,y,n. Since there are more than 3 independent equations, we cannot find any vector $\underline{x}$ satisfying this system exactly. However, it is possible to find a vector $\underline{x}$ satisfying a "least square" criterion. The factors thus obtained can be considered as an "optimum" for describing the relation between the signals and the loadings. The description of a least square problem of this nature is given in ref. 17.

An analogous description can be given for derivation of the factors $\omega_{2,j}$ and $\omega_{3,j}$, j = 1,2,3. And indeed, for the front station, we have the same problem except that it is four dimensional instead of three dimensional.

Since m is taken fairly large to improve accuracy of the final result, a computer program called MDETMAT has been written (mnemonic for Modified DETerminer of MATrix). The FORTRAN program uses NAG-routine F04JAF, solving the actual least square problems. Usage of this kind of readily available routines gives enormous savings in software-writing time.

When we have obtained the matrix χ, we of course have to invert this to obtain Ω :

$$\Omega = \chi^{-1} \tag{A1.6}$$

This is done by program INVMAT (mnemonic for INVersion of MATrix) using NAG-routine F01AAF.

Direct method :

This method prevents the operation of matrix inversion, so the final result may well be more accurate, depending on the condition of the inverted matrix in the indirect case. The method generates the matrices Ω and M in a direct way. *eg* For the rear station, the first system is:

$$\begin{pmatrix} \sigma_{p,1} & \sigma_{y,1} & \sigma_{n,1} \\ \sigma_{p,2} & \sigma_{y,2} & \sigma_{n,2} \\ & \vdots & \\ \sigma_{p,m} & \sigma_{y,m} & \sigma_{n,m} \end{pmatrix} \times \begin{pmatrix} \mu_{11} \\ \mu_{12} \\ \mu 13 \end{pmatrix} = \begin{pmatrix} \lambda_{p,1} \\ \lambda_{p,2} \\ \vdots \\ \lambda_{p,m} \end{pmatrix} \tag{A1.7}$$

or: $\quad B \times \underline{y} = \underline{c}$

$\underline{c}$ and B are known, $\underline{y}$ to be solved by the least square method. This least square method is the same as the one used to solve equation (A1.5), since equation (A1.7) is mathematically the same as (A1.5). When both the direct and indirect methods are used, we obtain matrices Ω and χ for the rear station and M and N for the front station. They should be the inverse, or approximately the inverse of each other. If they differ we will have to test which one performs better, *eg* for the rear station:

Ω obtained by direct method
or χ^{-1} obtained by indirect method

The testing of the matrices is done by the program DETLOAD (mnemonic for DETerminer of LOADings), using the NAG-routine F01CKF, which is a matrix multiplication routine. DETLOAD simply computes the loadings on the front and rear stations and then combines the two to get the overall forces and moments around a certain moment reference centre.

The following is the matrix for the front station, obtained by the direct method:

$$M = \begin{pmatrix} -34.9923703 & 8.1664415 & 0.6738611 & 0.4372738 \\ 6.7375606 & -35.4473074 & -0.6719434 & -0.1866956 \\ 1.1953189 & -4.0658361 & -33.5341227 & -0.2133595 \\ 0.1817767 & -0.1357321 & -0.2942013 & -35.2138376 \end{pmatrix}$$

and for the rear station:

$$\Omega = \begin{pmatrix} 36.2072972 & 0.0120921 & -0.0599730 \\ -7.7872748 & -34.1211834 & -0.2481124 \\ -0.9287326 & -4.0358437 & -32.4388051 \end{pmatrix}$$

(Obviously, the dimension of each matrix corresponds to the number of strain-gauge bridges mounted on it.) We see clearly that for *eg* matrix M, the primary matrix factors (m_{ii}) are considerably bigger

than the secondary ones (m_{ij}, $i \neq j$), as expected. The same statement is true for Ω.

The combination of front and rear loadings is done in the same way for both the "old" and "new" methods. A comparison of the accuracy of both methods can be made with table A1.1. This table is made by applying calibration weights on the balance by means of a calibration rig. (The "direct" version of the "new" version is used because it appeared to be slightly more precise than the "indirect" version. Besides that, the whole matrix derivation is simpler.)

The balance is designed to be mounted with one particular side to the outside of the WA during the aerodynamic testing whatever the model attitude in roll. The highest loads are obviously going to be in this direction since it is the direction of the centrifugal loads. This direction corresponds to the direction of the Force "Z" as mentioned in Table A1.1. In order to calibrate the balance within proper ranges, an estimation had to be made of the approximate maximum forces and moments. Since the model weight was estimated to be 4.54 kg (10 lb), the maximum normal force (in centrifugal direction) during calibration was 27.24 kg (60 lb). A representative selection of calibration runs is shown in Table A1.1 and as we see, both the old and the new method give reasonable predictions. Loading 1010 *eg* shows that in the presence of a large normal force, the low sideforce (0) is accurately enough predicted. The maximum discrepancy between actual force and predicted force is found to be with the "old" method, loading 1010;

$$\Delta Y = 0.49 \times 0.454 \times 9.81 \text{ N} = 2.18 \text{ N}$$

To find out how big an aerodynamic force coefficient conforms with this, we state:

$$\Delta C_R = \frac{\Delta Y}{0.5 \rho V^2 S} \qquad \text{(A1.8)}$$

For the 4/9 scale HIRM II model:

$$S = 0.4073 \text{ m}^2$$

For nominal W/A speed:

$$V = 2\pi nR = 2\pi \times \left(\frac{25}{60}\right) \times 8.306 \text{ m/s} = 21.75 \text{ m/s}$$

Hence

$$\Delta C_R = \frac{\Delta Y}{0.5\rho V^2 S} = \frac{2.18}{0.5 \times 1.225 \times (21.75)^2 \times 0.4073} = 0.0185$$

If we assume that $C_{L_{max}} = 2$, then:

$$\frac{\Delta C_R}{C_{L_{max}}} = 0.925 \text{ \%} \qquad \text{(A1.9)}$$

From (A1.9), we see that the accuracy of force prediction with the old method is <u>probably</u> around 1 % of $C_{L_{max}}$. This is considered to be reasonable.

A further look at Table A1.1 allows us to make a "performance" comparison between the "old" and the "new" method. We see that the new method gives the best estimates in 34 cases and the old method in 19 cases. This clearly better performance of the "new" (and simpler) method, is one of the reasons it is going to be used for all future transient tests.

Appendix 2 Nose probe calibrations

A2.1 Calibration procedure as used for HIRM tests

Because of swirl in the test passage of the Whirling Arm during HIRM measurements, it was considered necessary to measure the flow conditions near the model more precisely. This is especially important because it was suspected that the flow directions and dynamic pressure due to swirl can be quite different on both sides of the arm, so using *eg* the pitot-static probe on the opposite side does not necessarily give accurate enough information about the situation near the model.

A 5-hole nose probe is used for this purpose. The calibration of it is done in the College of Aeronautics "Weybridge" wind tunnel. Since there was no known method at that time for calibrating the probe to get all four independent flow parameters (*eg* α, β, p_t and p) accurately enough, some trials had to be done to devise such a method. Since it proved to be infeasible to find such a method within the very limited time, a simplified calibration was carried out. This calibration only uses three holes: the centre hole and the two other opposite holes. It was intended to derive only the dynamic pressure and the angle of attack with this method, since these parameters are considered to be the most important. This method is described in this chapter.

The probe, shown in fig. 2.2, was considered to be of sufficient length to be in undisturbed flow, so it is not necessary to calibrate it while it is mounted on a HIRM model. For calibration, the probe was mounted on a mast which was located on a turntable. The probe height was approximately at the tunnel centre (see Fig. A2.1). The probe is mountable as shown in Fig. A2.1, or it can be "rolled" over 180°. With the rotation vector of the turntable vertical, the turning represents different angles of attack and the holes (as in Fig. A2.1) can be designated top, centre and bottom.

It is first necessary to find the exact flow direction of the tunnel. (Because of flow imperfections, the flow direction at the tunnel centre might well be not parallel to the tunnel axis.) This is done by measuring $P_T - P_B$ at different incidences, both for roll angle $\phi = 0^\circ$ and 180°. (See Fig. A2.2.) This procedure takes into account the manufacturing imperfection of the probe. Due to this imperfection, $\Delta\tau$ (as defined in fig. A2.2) is a non-zero (but small) angle. The difference between the tunnel-axis and the flow direction in the horizontal plane through the probe is defined as τ_0. It can be derived from measurements as shown in fig. A2.2. The "probe incidence angle" α_{probe} is defined as zero, when the probe is pointed in the direction of the (local) tunnel flow, hence :

$$\alpha_{probe} = \tau - \tau_0 \tag{A2.1}$$

Subsequently, a scan is made over the expected incidence rate, for roll angle $\phi = 0^\circ$. In this scan, the following values are measured:

$$A = \frac{P_T - P_B}{0.5\rho V^2} \tag{A2.2}$$

$$B = \frac{P_C - \frac{P_T + P_B}{2}}{0.5\rho V^2} \tag{A2.3}$$

The values P_C, P_T and P_B are read from the probe-tappings (centre, top and bottom) and the value of $0.5\rho V^2$ can be found from the measuring system of the tunnel. The values as found for this probe is shown in Fig. A2.3. The ratio A/B (see Fig. A2.3) lies on a fairly linear curve , which is quite suitable for calibration purposes. The value A/B can be measured from the probe tappings, and α_{probe} can be determined unambiguously. Then, the value of A can be determined, from which the dynamic pressure can be derived.

Fig. A2.3 shows on the horizontal axis the value of $\alpha_{probe} + 4^\circ$ rather than α_{probe}, because the HIRM models have a nose cone with an axis directed 4° down (see Fig. 2.2 and 2.3). Hence, if

$\alpha_{probe} + 4^{\circ} = 0^{\circ}$, then the axis of the model has 0° incidence with the undisturbed flow.

The hemispherical nose probe with the arrangements of holes used in the longitudinal tests on HIRM I was not entirely satisfactory because it became less sensitive to flow direction at incidences above 25°. This was probably due to the upper hole becoming in, or close to, a separated area and the lower hole being close to the point of maximum pressure.

A2.2 Multi-hole probes - some general notes

Many different types of multi-hole probes have been used in the past, for various purposes. They exist as 2, 3, 4, 5 or 7-hole probes. Their purposes can be roughly divided into:

a. Probes for boundary-layer measurement (Quasi-2D flow).
b. Probes for measurements in separated flow.
c. Probes for measurement in non-separated, 3-dimensional flow.

The shape of the probes is such that their specific tasks can be performed in the best way. Type c can be sub-divided into:

c.1 Nulling probes.
c.2 Non-nulling probes.

A "nulling probe" is a probe that can be rotated about one or more axes, so that when the pressure difference between two opposing holes is zero, the flow direction in one or two planes is known, except for possible instrument-errors. In this way, the probe has to be adjusted for every measuring point, which can be a time-consuming task in case of large amounts of measuring points. An advantage, however, is that a direction calibration is not necessary (at least if the instrument-error is small enough) and the calibrations to obtain the total and static pressures are greatly simplified. A "non-nulling probe" is placed in a fixed direction and from the pressure readings, the flow-direction (and perhaps other flow-characteristics) can be determined. This is done by means of the results of the calibration of the probe.

Extensive literature is available about various types of probes. A (by no means complete) selection is given here. Ref. 9 describes several probes and their calibration of type a and b. One of them, the so-called "Templin-probe", (of type a), is used in the past on the Whirling Arm for ground-effect research. This is described in ref. 2. For the HIRM-project, we are particularly interested in the probes of type c, in order to get proper information in the vicinity of the moment reference centre. The probe needs to be of type c.2 (as

is the one used on the HIRM models) because the probe cannot be made adjustable relative to the model and because of the much faster measuring technique. ref. 16 describes the theory and calibration of a conical probe of type c.2, as does ref. 11. ref. 12 explains the importance of the geometry of the head of the probe. From that, it appears that a hemispherical probe is better suited for HIRM measurements on the WA than a conical head. (The one used on the tests has a hemispherical head.) Ref. 12 also explains an interesting calibration procedure for such a probe with which accurate estimations of all four independent flow parameters can be made, both subsonic and supersonic to $M \approx 2$. The calibration-coefficients are chosen by making use of the theoretical behaviour of flow over a sphere, at the various Mach numbers. By doing this, the flow parameters can be determined with higher precision than previously possible.

Obviously, on the WA we only need low-Mach number calibration. The procedure mentioned in ref. 12 can be simplified to cover only the incompressible range. Presumably, this is the procedure that is going to be carried out in the future. It will be possible to use the current 5-hole nose probe and measure α, β and q with relatively high precision. This will increase the "quality" of the aerodynamic data obtained from the WA tests. The precise procedure will be described in future work.

Appendix 3 Pressure measurent on the Whirling Arm some general notes

When setting up a pressure measurement system on the WA, one has to think carefully about what exactly is being measured and eventual corrections on the outputs. These corrections may be necessary due to several factors, mainly resulting from the typical Whirling Arm environment with its problems:

a) Placement of the pressure transducers.
b) Difference in radii of the static and total port in case of differential pressure measurement.
c) Influence of swirl.
d) Time lag due to transducer inertia and pressure tubes inertias.
e) Nose-probe calibration shortcomings.

The following notes are written to clarify the corrections as mentioned above. They are partly already discussed in ref. 1.

Let us consider the simple tubing system depicted in Fig. A3.1. It shows a tube which can be thought as part of a pressure measuring system mounted on the Whirling Arm. Its ends are open and located at different radii from the WA centre. With the arm running at a certain (constant) angular velocity ω, there will be a force acting on the air in the tube, as a result of centrifugal effects. To assess this force, only the pressure-component perpendicular to the radius plays a role. Hence, the centrifugal force acting on the air in the tube between $R = R_1$ and $R = R_2$ is:

$$F_c = \int_{r=R_1}^{R_2} \rho \times a(r) \times A \times dr \qquad \text{(A3.1)}$$

with A = cross-sectional internal area of the tube (Fig. A3.1).

$$\Rightarrow F_c = \int_{R_1}^{R_2} \rho \times \omega^2 \times r \times A \times dr = \rho A \omega^2 \times \int_{R_1}^{R_2} r \times dr = 0.5 \times \rho A \omega^2 \left[r^2 \right]_{R_1}^{R_2} =$$

$$= 0.5 \times \rho A \omega^2 \left(R_2^2 - R_1^2 \right) \qquad \text{(A3.2)}$$

Hence, the resulting pressure difference between $r = R_1$ and $r = R_2$ is:

$$p_2 - p_1 \equiv \Delta p_{21} = 0.5 \times \rho \omega^2 \left(R_2^2 - R_1^2 \right) = \frac{F_c}{A} \qquad \text{(A3.3)}$$

(Remember, this is only as a result of the centrifugal effect.) For $R_1 = 0$ and $R_2 = R$ = the nominal whirling arm radius, we get:

$$\Delta p_{21} = 0.5 \times \rho \omega^2 R^2 = 0.5 \times \rho (V_\omega)^2 \qquad \text{(A3.4)}$$

with V_ω = the speed of the arm at (nominal) radius R relative to the earth.

Now we consider a pressure measuring system with the tube as mentioned above and with a pressure transducer at radius R_{pr} with:

$$0 \leq R_{pr} \leq R \qquad \text{(A3.5)}$$

(See fig. A3.2.)
The pressure tapping d is used as a pitot tapping, static tapping or anything else (*eg* one of the 5-hole probe tappings), so the pressure p_d must be interpreted as such. The tube at $r = 0$ is connected to the atmosphere, so p_a is the atmospheric pressure at the arm centre. To find out what exactly the transducer is measuring, we try to find:

$$\Delta p_{cb} = p_c - p_b \tag{A3.6}$$

$$\left.\begin{aligned} &\text{with} \quad \Delta p_{dc} = p_d - p_c \\ &\text{and} \quad \Delta p_{ba} = p_b - p_a \end{aligned}\right\} \tag{A3.7}$$

Substitution of (A3.7) in (A3.3) gives:

$$\left.\begin{aligned} \Delta p_{dc} &= 0.5\times\rho\omega^2\left(R_d^2 - R_c^2\right) = 0.5\times\rho\omega^2\left(R^2 - R_c^2\right) \\ \text{and } \Delta p_{ba} &= 0.5\times\rho\omega^2\left(R_b^2 - R_a^2\right) = 0.5\times\rho\omega^2 R_b^2 \end{aligned}\right\} \tag{A3.8}$$

$$\Rightarrow \quad \begin{cases} p_c = p_d - \Delta p_{dc} = p_d + 0.5\times\rho\omega^2\left(R_c^2 - R^2\right) \\ p_b = p_a + \Delta p_{ba} = p_a + 0.5\times\rho\omega^2 R_b^2 \end{cases} \tag{A3.9}$$

Combination of (A3.6) and (A3.9) with $R_c = R_b$ gives:

$$\Delta p_{cb} = p_d - p_a - 0.5\times\rho\omega^2 R^2 = p_d - p_a - 0.5\times\rho(V_\omega)^2 \tag{A3.10}$$

Looking at (A3.10), we see that the location of the pressure transducer in this system (R_{pr}) plays no role at all.

One of the conclusions of this is that we can build a system as in Fig. A3.3, with *eg* p_e the static pressure from the pitot-static probe on the opposite side arm. If we assume this pressure to be equal to the static pressure at position d, and we take p_d as a total pressure tapping, then we can derive the dynamic pressure at position d by this measuring system, when V_ω is measured by the rpm-indicator. This can be shown as follows:

We substitute in (A3.3);

$$\left.\begin{aligned} \Delta p_{cd} &= p_c - p_d \\ \Delta p_{be} &= p_b - p_e \end{aligned}\right\}$$

So,

$$\left.\begin{aligned} p_c - p_d = \Delta p_{cd} &= 0.5\times\rho\omega^2\left(R_c^2 - R_d^2\right) \\ p_b - p_e = \Delta p_{be} &= 0.5\times\rho\omega^2\left(R_b^2 - \left(-R_e\right)^2\right) = 0.5\times\rho\omega^2\left(R_b^2 - R_e^2\right) \end{aligned}\right\}$$

$$\Rightarrow \quad \begin{cases} p_c = 0.5\times\rho\omega^2\left(R_c^2 - R_d^2\right) + p_d \\ p_b = 0.5\times\rho\omega^2\left(R_b^2 - R_e^2\right) + p_e \end{cases}$$

$$\Rightarrow \quad \Delta p_{cb} = p_c - p_b = 0.5\times\rho\omega^2\left(R_c^2 - R_d^2\right) + p_d + 0.5\times\rho\omega^2\left(R_e^2 - R_b^2\right) - p_e$$

$$\text{with} \begin{cases} R_e^2 = R_d^2 = R^2 & \text{and } R_b^2 = R_c^2 \\ p_e = p_{stat,e} = p_{stat,d} & \\ p_d = P_{tot,d} = 0.5\times\rho V_d^2 + p_{stat,d} & \end{cases}$$

we get:

$$\Delta p_{cb} = 0.5\times\rho V_d^2 \qquad \text{(A3.11)}$$

V_d is the airspeed at position d;

$$V_d = \omega R - V_s \qquad \text{(A3.12)}$$

Substitution of (A3.11) in (A3.12) gives:

$$\Delta p_{cb} = 0.5\times\rho(\omega R - V_s)^2 \qquad \text{(A3.13)}$$

This important relation shows that, with the assumption $P_{stat,e} = p_{stat,d}$ we can measure the (average) swirl speed V_s at position d with the system as depicted in Fig. A3.3. (Again, note the insignificance of the transducer location.) N.B. looking at (A3.13), we see that in order to know ρ, it will be necessary to measure ambient temperature and pressure.

In general, when measuring pressures on the Whirling Arm, one must always bear in mind that there might be a certain amount of swirl flow. This swirl might be of a turbulent nature, so when taking measurements on a steady state experiment, multiple samples have to be taken to calculate the average pressures. (The same is true for the strain-gauge balance outputs.) Additionally, the standard deviations of the samples can be computed to get an impression of the amount of turbulence.

As mentioned before, the transducer location plays no role as far as centrifugal effect on the aircolumn in the tubing system is concerned. The only thing to check is the effect of centrifugal loading on the transducer itself. For a membrane-type transducer, this effect will be minimal with the membrane-surface parallel to the arm-radius. Besides that, it will be minimal if R_{pr} is kept as low as possible. Consulting the technical documentation of the transducer or the manufacturer gives more information on this. Besides that, tests can be taken with the transducer mounted as in Fig. A3.4. Comparison of output with and without the arm running will give centrifugal effect on the membrane. (Connecting the transducer tappings to each other cancels out airmovement influence. The centrifugal effect in this tubing is self-compensating, *ie* it gives no influence on membrane deflection. We can find this tubing centrifugal effect $\Delta p_{ab} = 0$ by applying (A3.3) on the system a b c d as in Fig. A3.4.)

The samples taken from the 5-hole nose probe only make sense if a suitable calibration has taken place. There can be various

shortcomings in this calibration, *eg* the tunnel where the calibration has taken place has a flow which is not parallel enough for these purposes. More information on calibration of these probes is given in Appendix 2.

When making transient measurements (*eg* for the $\dot{\alpha}$-experiment described in a future report), the time lag in the tubing system will play a significant role. The tube's diameter, length and volume determine the "capacity" and the "resistance" of the system, and hence the time lag. Due to this time lag, the tubing system effectively acts as a low-pass filter in case of steady-state measurements, ruling out the need for electronic filtering. For the transient experiment as mentioned earlier, this time lag is probably too high to make any nose-probe measurements useful, even if the transducers are mounted in the model to limit the tube lengths. Various literature is available to estimate the time-lag of tubing system, *eg* ref. 13, 14 and 15.

model number	scale	HIRMI / II	materials	tests
2149	1/1	I	various	FF
2130	4/9	I	steel, GRP, aluminium alloy	SAOR, LAPR, static
2206	4/9	I	foam, GRP, CRP	WA, ADR, static
2093	4/9	I	master model for 2206 manufacturing	
2131	2/9	I	aluminium alloy	RR
2167	1/1	II	various	FF
2201	4/9	II	steel, GRP, aluminium alloy	SAOR, LAPR, static
2254	4/9	II	foam, GRP, CRP	WA (future: ADR)
2215	2/9	II	aluminium alloy	RR

table 1.1. Various HIRM models and their use.

Quantity	Example	Divisor for obtaining normalised quantity	
		in the aero-system	in the dynamic system
Length		l_0	The same
Mass		$\frac{1}{2}\rho_e S l_0$	
Time		l_0/V_e	
Linear velocity	w	V_e	as in the
Linear acceleration	$\dot{w}$	V_e^2/l_0	
Angular displacement	η	1	
Angular velocity	q	V_e/l_0	
Angular acceleration	$\dot{q}$	V_e^2/l_0^2	previous
Force	Z	$\frac{1}{2}\rho_e V_e^2 S$	
Moment	M	$\frac{1}{2}\rho_e V_e^2 S l_0$	
Pressure	P	$\frac{1}{2}\rho_e V_e^2 S/l_0^2$	column
Density	ρ	$\frac{1}{2}\rho_e S/l_0^2$	
Viscosity		$\frac{1}{2}\rho_e V_e S/l_0$	
Force derivatives with respect to			except that
linear displacement	Z_h	$\frac{1}{2}\rho_e V_e^2 S/l_0$	
linear velocity	Z_w	$\frac{1}{2}\rho_e V_e S$	
linear acceleration	$Z_{\dot{w}}$	$\frac{1}{2}\rho_e S l$	l_0
angular displacement	Z_η	$\frac{1}{2}\rho_e V_e^2 S$	
angular velocity	Z_q	$\frac{1}{2}\rho_e V_e S l_0$	
Moment derivatives with respect to			is replaced by
linear displacement	M_h	$\frac{1}{2}\rho_e V_e^2 S$	
linear velocity	M_w	$\frac{1}{2}\rho_e V_e S l_0$	
linear acceleration	$M_{\dot{w}}$	$\frac{1}{2}\rho_e S l_0$	μl_0
angular displacement	M_η	$\frac{1}{2}\rho_e V_e^2 S l_0$	
angular velocity	M_q	$\frac{1}{2}\rho_e V_e S l_0^2$	

Since $\mu = m_e/\frac{1}{2}\rho_e S l_0$ and $\tau = m_e/\frac{1}{2}\rho_e V_e S = \mu l_0/V_e$, the divisors for obtaining dynamic-normalised quantities sometimes have simpler alternative forms. For example, as $\tilde{q} = q l_0/V_e$, then $\hat{q} = q\mu l_0/V_e = q\tau$. Similarly

as $\tilde{M}_w = M_w/\frac{1}{2}\rho_e V_e S l_0$, then

$\hat{M}_w = M_w/\frac{1}{2}\rho_e V_e S\mu l_0 = M_w/m_e V_e$.

Source : ref.10

Table 3.1 . Divisors for normalised systems of units .

ALPHA DEG.	BETA DEG. (GEOM.)	SIDE FORCE COEF.	YAWING MOMENT COEF.	ROLLING MOMENT COEF.
0.0	0.0	0.015	0.0143	0.0013
	-6.0	0.078	0.0053	0.0039
	+6.0	-0.054	0.0264	-0.0027
5.2	0.0	0.023	0.0125	-0.0077
	-6.0	0.089	0.0037	0.0000
	+6.0	-0.048	0.0245	-0.0140
10.4	0.0	0.027	0.0124	-0.0118
	-6.0	0.096	0.0033	0.0052
	+6.0	-0.045	0.0229	-0.0282
13.0	0.0	0.028	0.0125	-0.0135
	-6.0	0.100	0.0040	0.0072
	+6.0	-0.040	0.0208	-0.0332
15.6	0.0	0.031	0.0112	-0.0173
	-6.0	0.098	0.0043	0.0060
	+6.0	-0.033	0.0173	-0.0384
18.2	0.0	0.038	0.0082	-0.0207
	-6.0	0.096	0.0036	0.0010
	+6.0	-0.020	0.0116	-0.0407
20.8	0.0	0.038	0.0046	-0.0269
	-6.0	0.094	0.0040	-0.0065
	+6.0	-0.011	0.0065	-0.0454
23.4	0.0	0.049	0.0033	-0.0308
	-6.0	0.096	0.0065	-0.0112
	+6.0	0.007	0.0006	-0.0474
26.0	0.0	0.062	0.0022	-0.0337
	-6.0	0.098	0.0079	-0.0142
	+6.0	0.022	-0.0034	-0.0506
28.5	0.0	0.067	0.0008	-0.0353
	-6.0	0.106	0.0100	-0.0162
	+6.0	0.025	-0.0066	-0.0518
31.1	0.0	0.082	-0.0003	-0.0357
	-6.0	0.126	0.0116	-0.0207
	+6.0	0.035	-0.0090	-0.0508

Table 4.1 Lateral coefficients from Model 2206 WA tests, top-up attitude.

loading number	$\mathcal{L}$	$\mathcal{M}$	$\mathcal{N}$	Y	Z	x_Y	x_Z
1010	0.0	-300.0	0.0	0.0	60.0	-	5.0
1012	0.0	-40.0	0.0	0.0	40.0	-	1.0
1013	12.0	-6.0	0.0	0.0	6.0	-	1.0
1021	12.0	-66.0	0.0	0.0	6.0	-	11.0
1034	0.0	0.0	-42.0	6.0	0.0	7.0	-
1037	0.0	0.0	-4.0	4.0	0.0	1.0	-
1038	-12.0	0.0	-6.0	6.0	0.0	1.0	-
1039	-12.0	0.0	-42.0	6.0	0.0	7.0	-
1040	-12.0	0.0	-66.0	6.0	0.0	11.0	-

table A1.1 a. Calibration loadings

Units : moments in pounds × lengths
forces in pounds
distances in lengths
(1 length = 50 mm)

loading number	$\mathcal{L}$	$\mathcal{M}$	$\mathcal{N}$	Y	Z	x_Y	x_Z
1010	.22	-301.62	2.62	-.49	60.37	-	4.996
1012	.41	-41.49	.59	-.32	40.13	-	1.034
1013	11.95	-6.67	.11	-.05	6.07	-	1.100
1021	12.34	-66.37	.37	-.04	6.03	-	11.000
1034	0.0	-.54	-42.01	6.02	0.07	6.981	-
1037	-.04	-.07	-4.03	4.02	.05	1.003	-
1038	-12.86	.35	-6.07	6.04	.03	1.005	-
1039	-12.58	-.36	-41.96	6.01	.06	6.985	-
1040	-12.55	-.52	-65.83	6.00	.05	10.977	-

table A1.1 b. Predicted calibration loadings, old method

Units : moments in pounds × lengths
forces in pounds
distances in lengths
(1 length = 50 mm)

loading number	$\mathcal{L}$	$\mathcal{M}$	$\mathcal{N}$	Y	Z	x_Y	x_Z
1010	-.31	-302.10	.51	-.06	60.26	-	5.014
1012	.13	-40.64	.10	-.01	39.89	-	1.019
1013	11.50	-6.57	-.09	.02	6.04	-	1.088
1021	11.85	-66.70	-.17	.03	6.07	-	10.993
1034	.15	-.26	-41.95	6.00	.03	6.986	-
1037	.10	-.17	-4.12	4.03	.02	1.021	-
1038	-12.21	.22	-6.07	6.03	-.02	1.007	-
1039	-12.00	-.06	-41.72	5.97	.01	6.997	-
1040	-12.00	.06	-65.62	5.94	-.01	11.027	-

Table A1.1 c. Predicted calibration loadings, new method

Units : moments in pounds × lengths
forces in pounds
distances in lengths
(1 length = 50 mm)

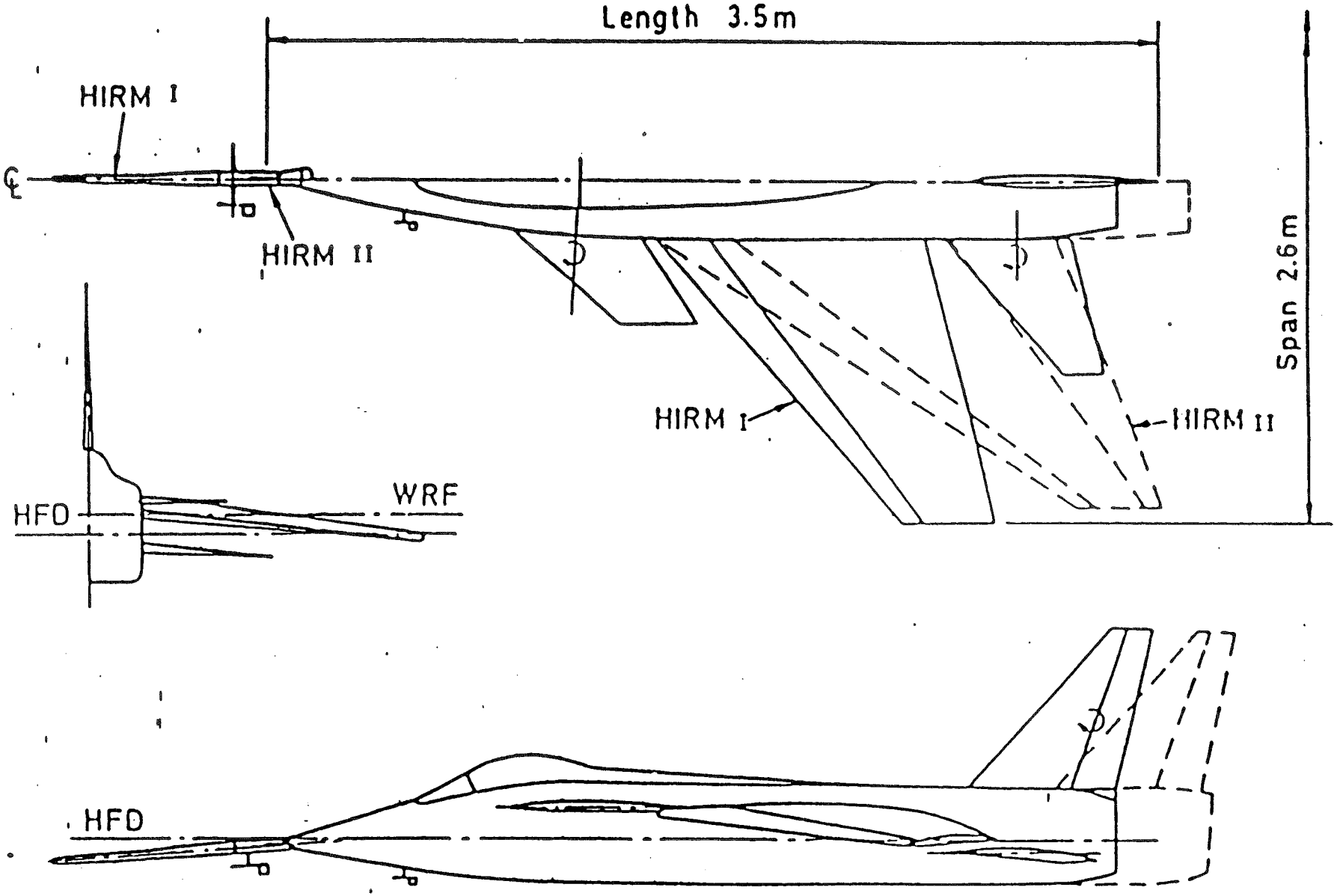

Figure 1.1 . HIRM I and HIRM II full scale models .

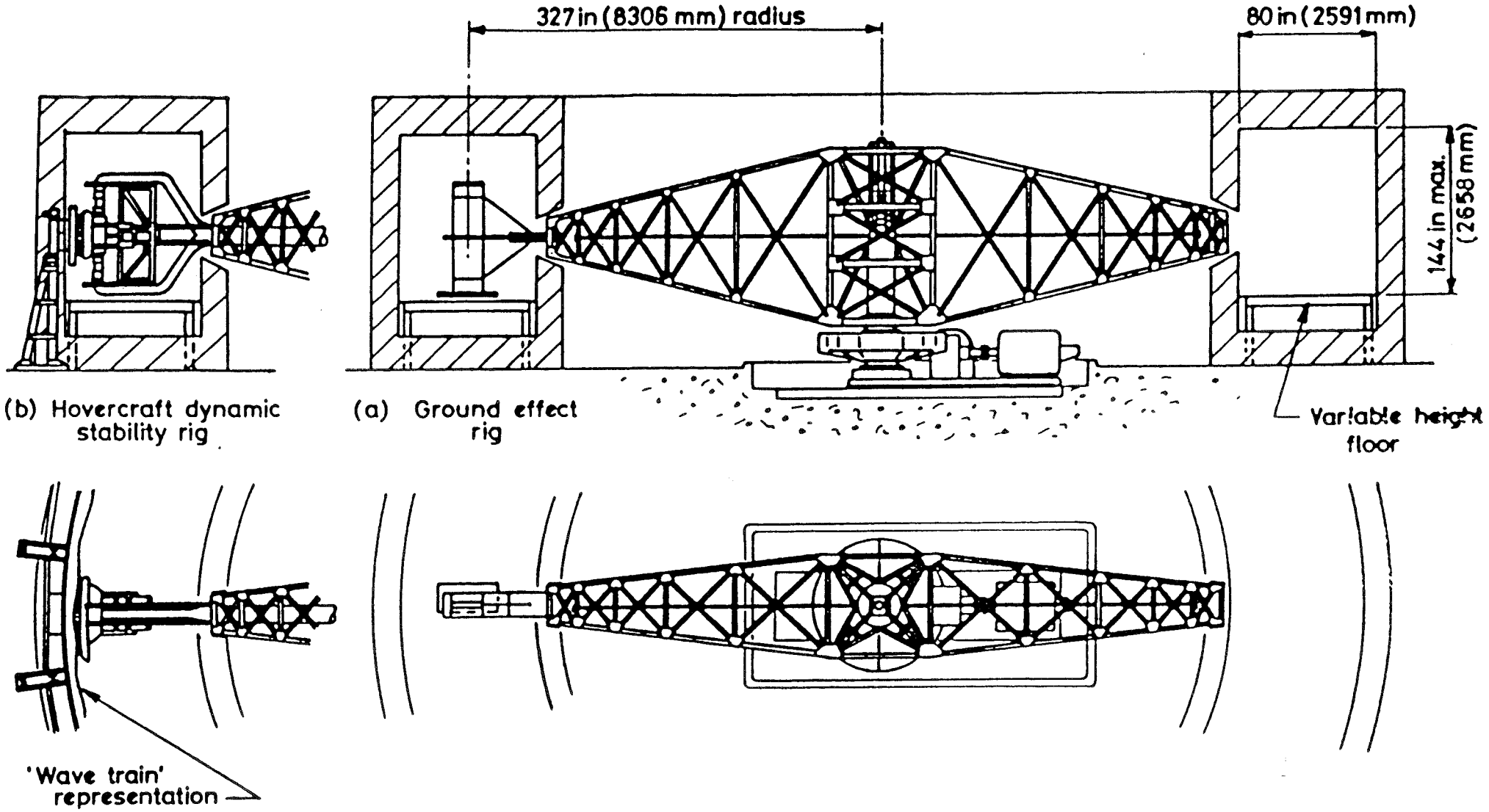

Figure 1.2 . The CIT Whirling Arm Facility . (Source : ref. 1)

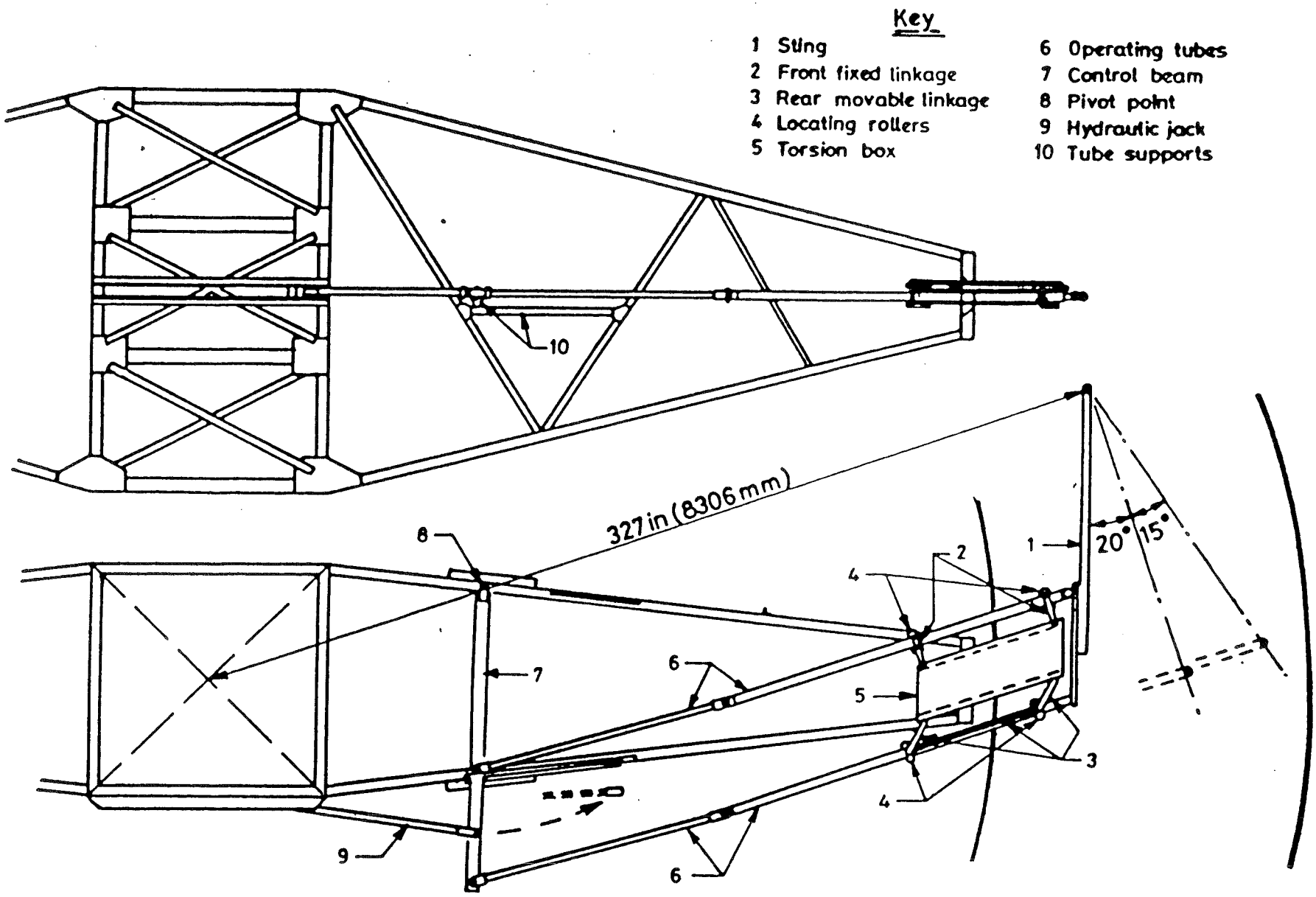

Figure 2.1 . Incidence changing mechanism . (Source : ref. 1)

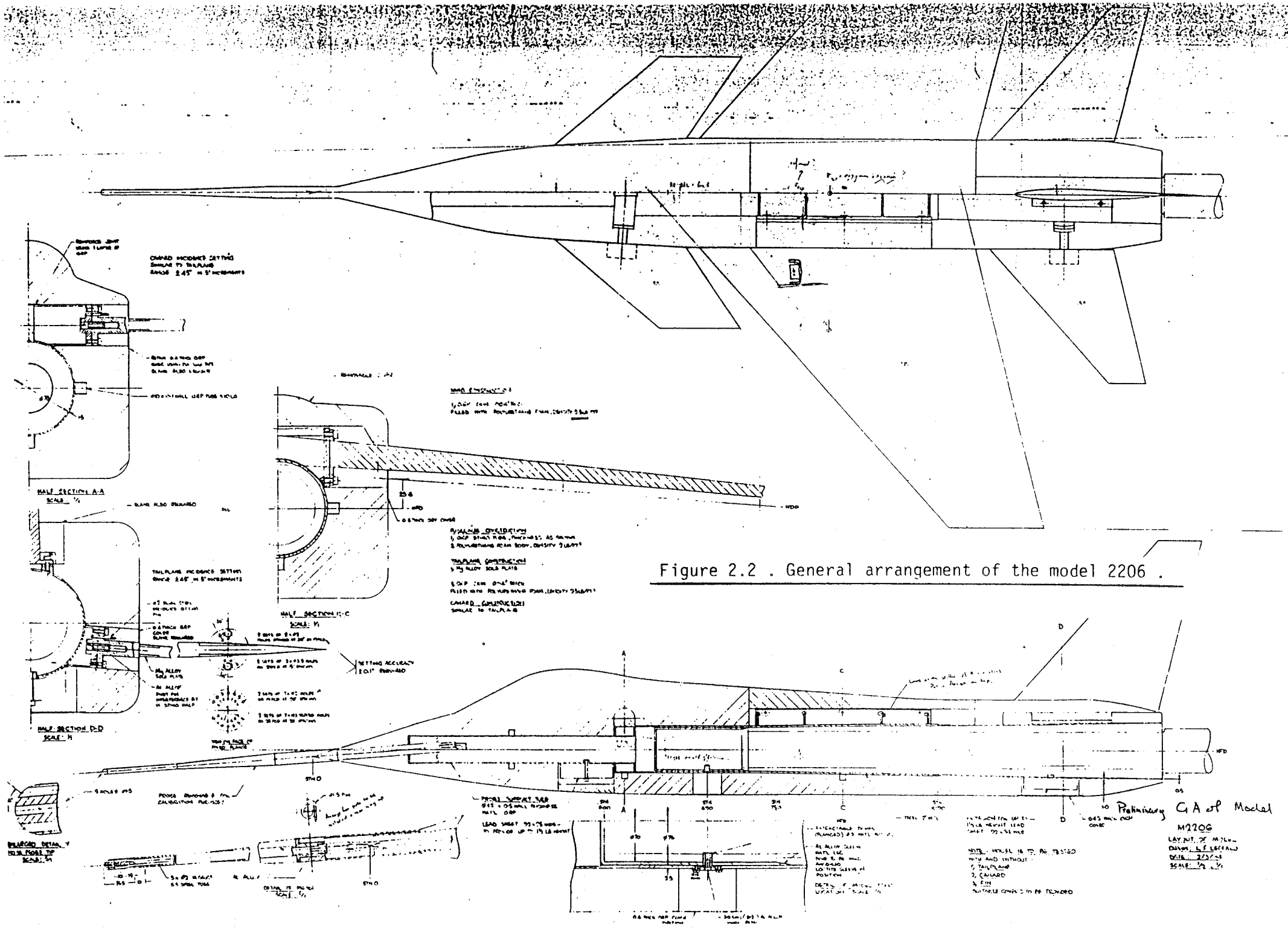

Figure 2.2 . General arrangement of the model 2206 .

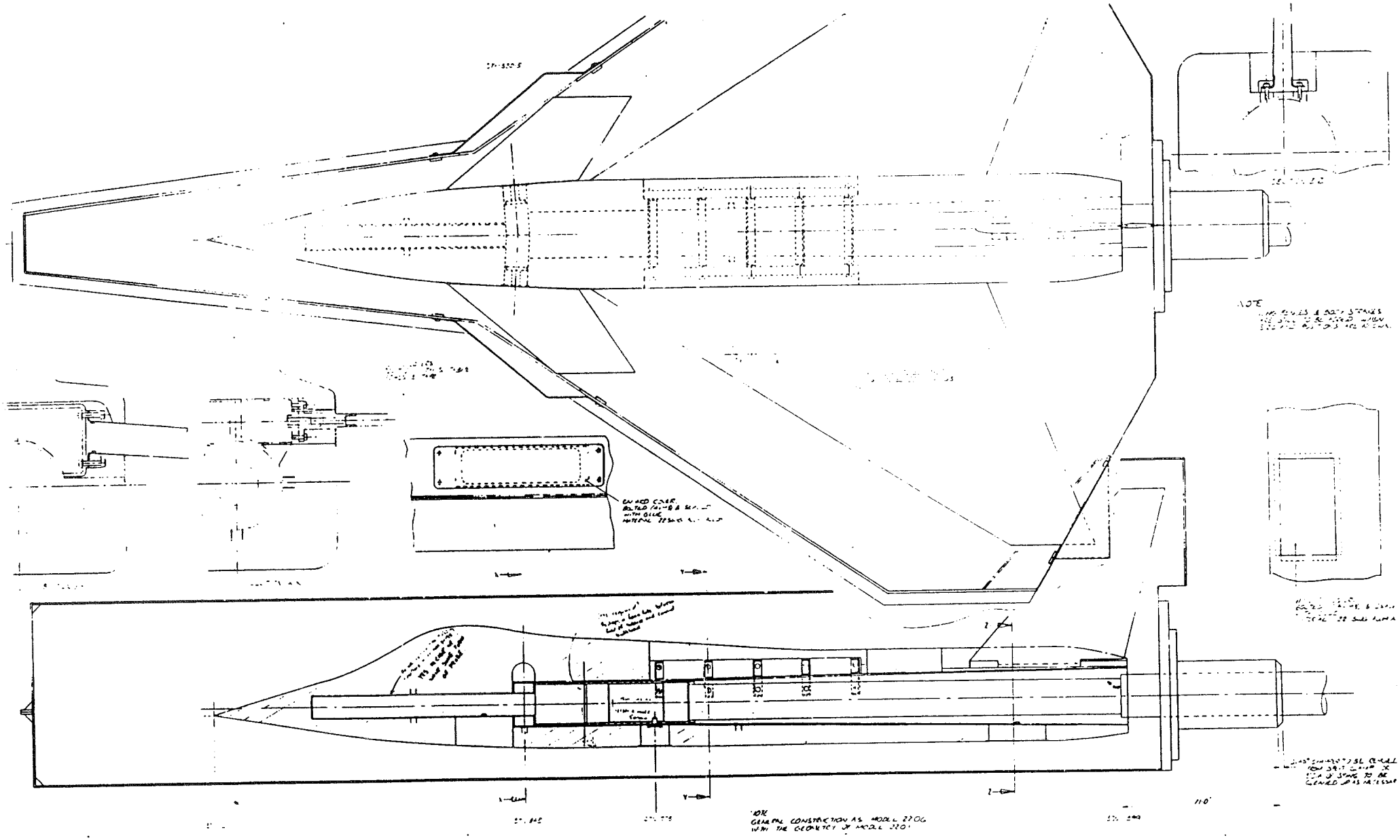

Figure 2.3 . General arrangement of the model 2254 .

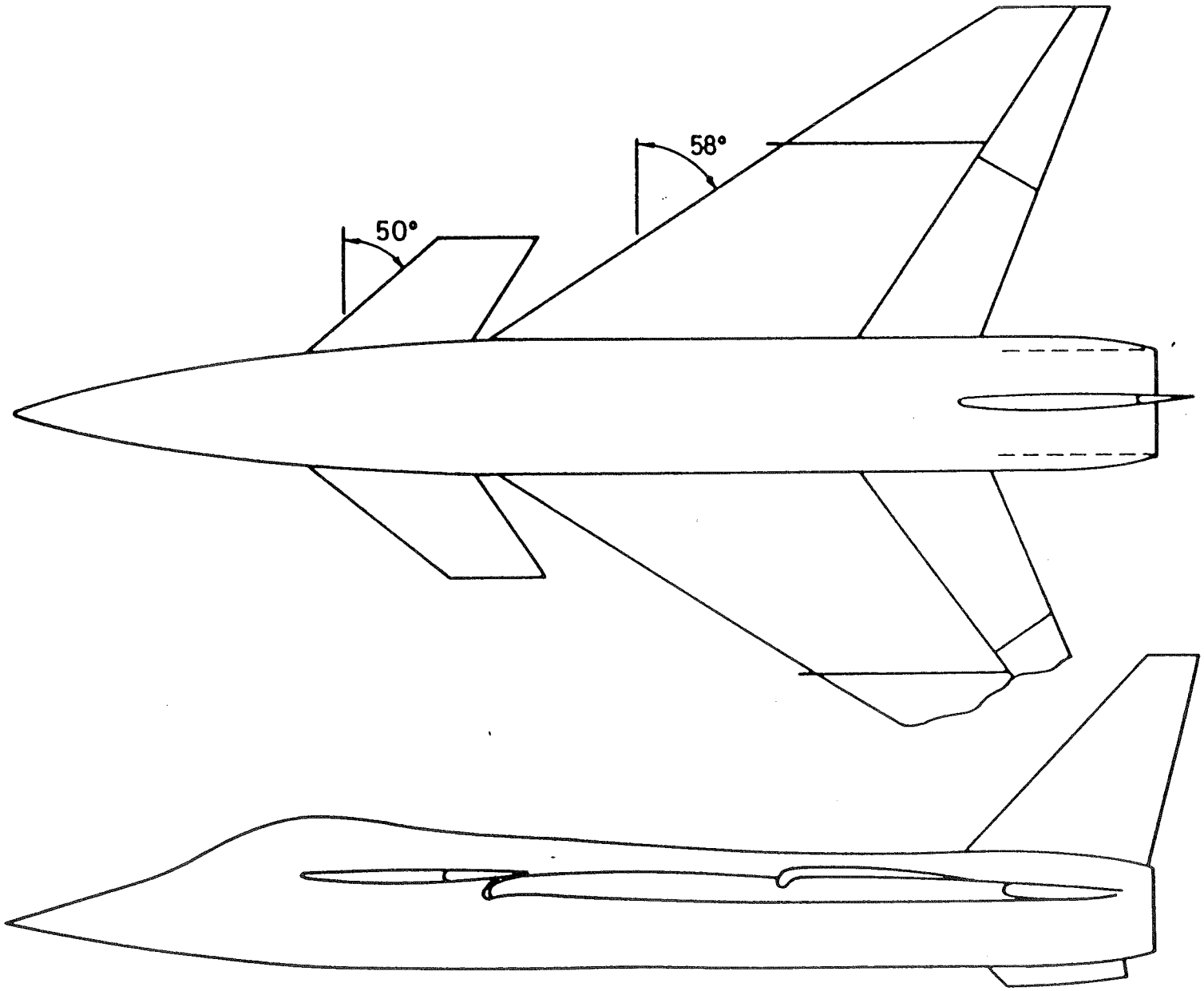

Figure 2.4 . HIRM II strakes and fences. (Source : ref. 20)

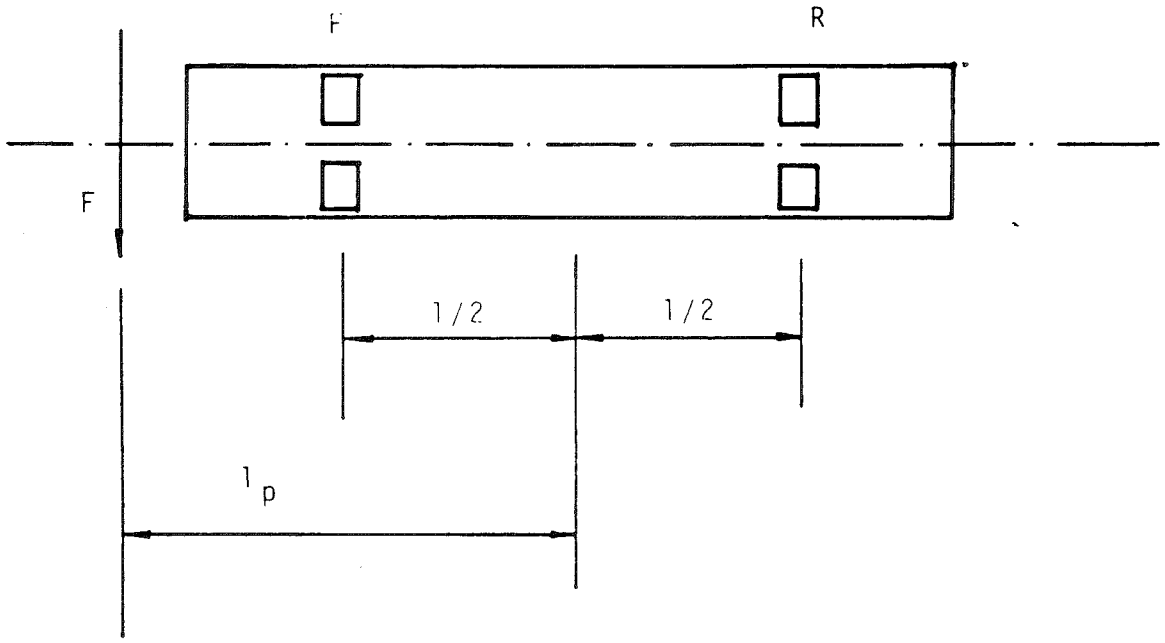

Figure 2.5 . Conventional strain gauge balance .

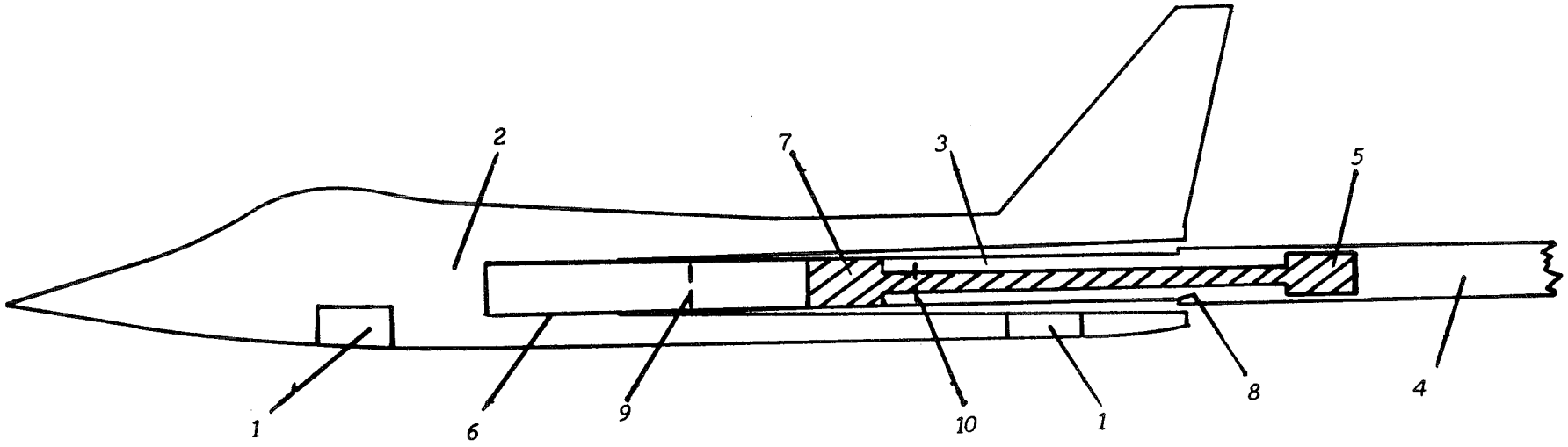

1 *provision for ballast*
2 *HIRM model*
3 *balance*
4 *sting*
5 *counterweight*
6 *connection balance-model*
7 *connection balance-counterweight*
8 *connection balance-sting*
9 *front strain-gauge station*
10 *rear strain-gauge station*

Figure 2.6. General scheme of model-balance assembly

This scheme shows the method of limiting the bending moments due to centrifugal loads at the front and rear strain gauge stations.

Provisions are made in the front and rear fuselage of the models to mount ballast. This is adjusted to bring the centrifugal bending moment at the front strain gauge station close to zero.

In the balance, between the two strain gauge stations, a rod is connected carrying a counterweight. The rod and counterweight do not touch the balance or sting at any point apart from the position where it is mounted on the balance. This counterweight is adjusted to bring the centrifugal bending moment at the rear station close to zero.

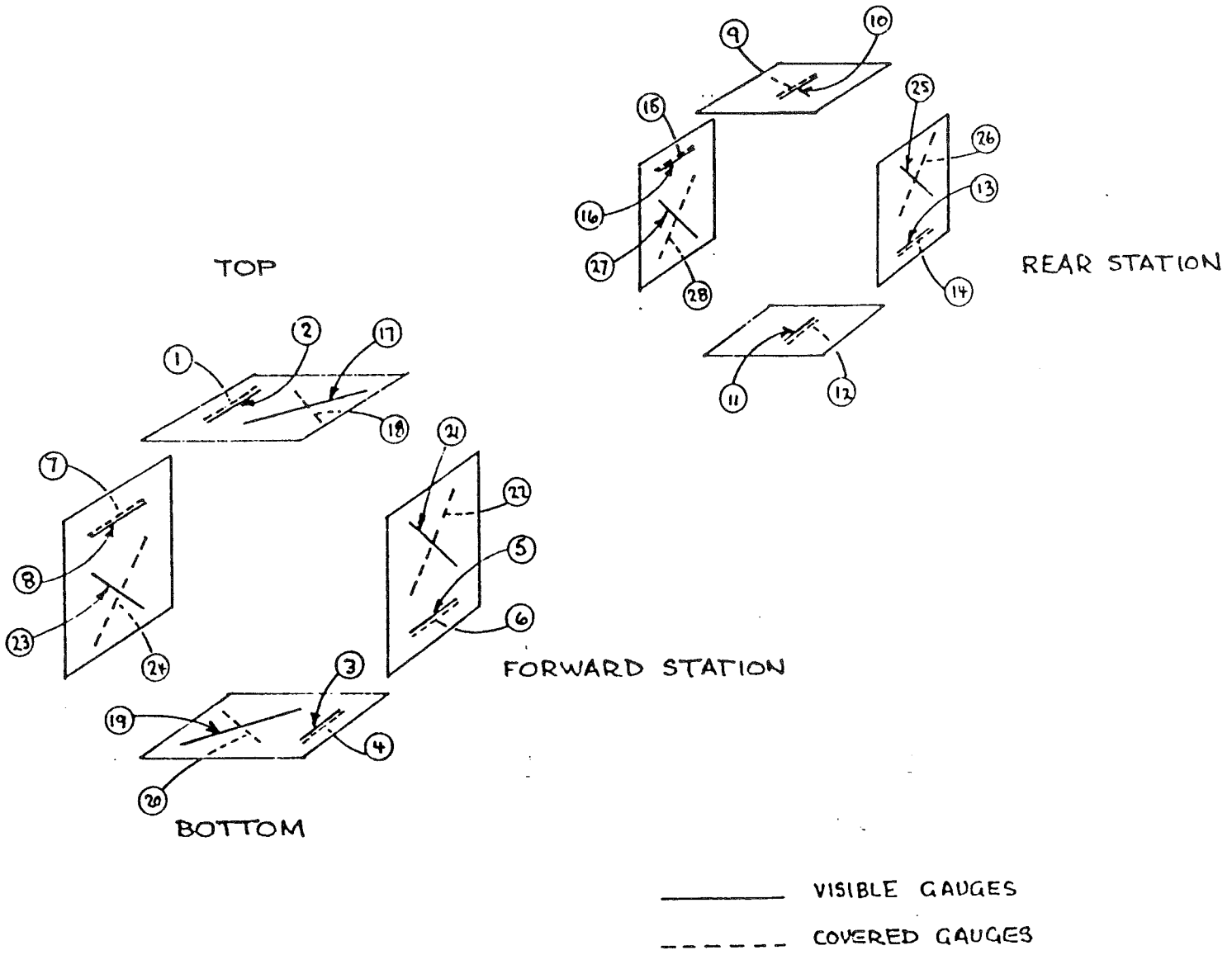

Figure 2.7 . Placement of strain-gauges for steady-state experiments balance .

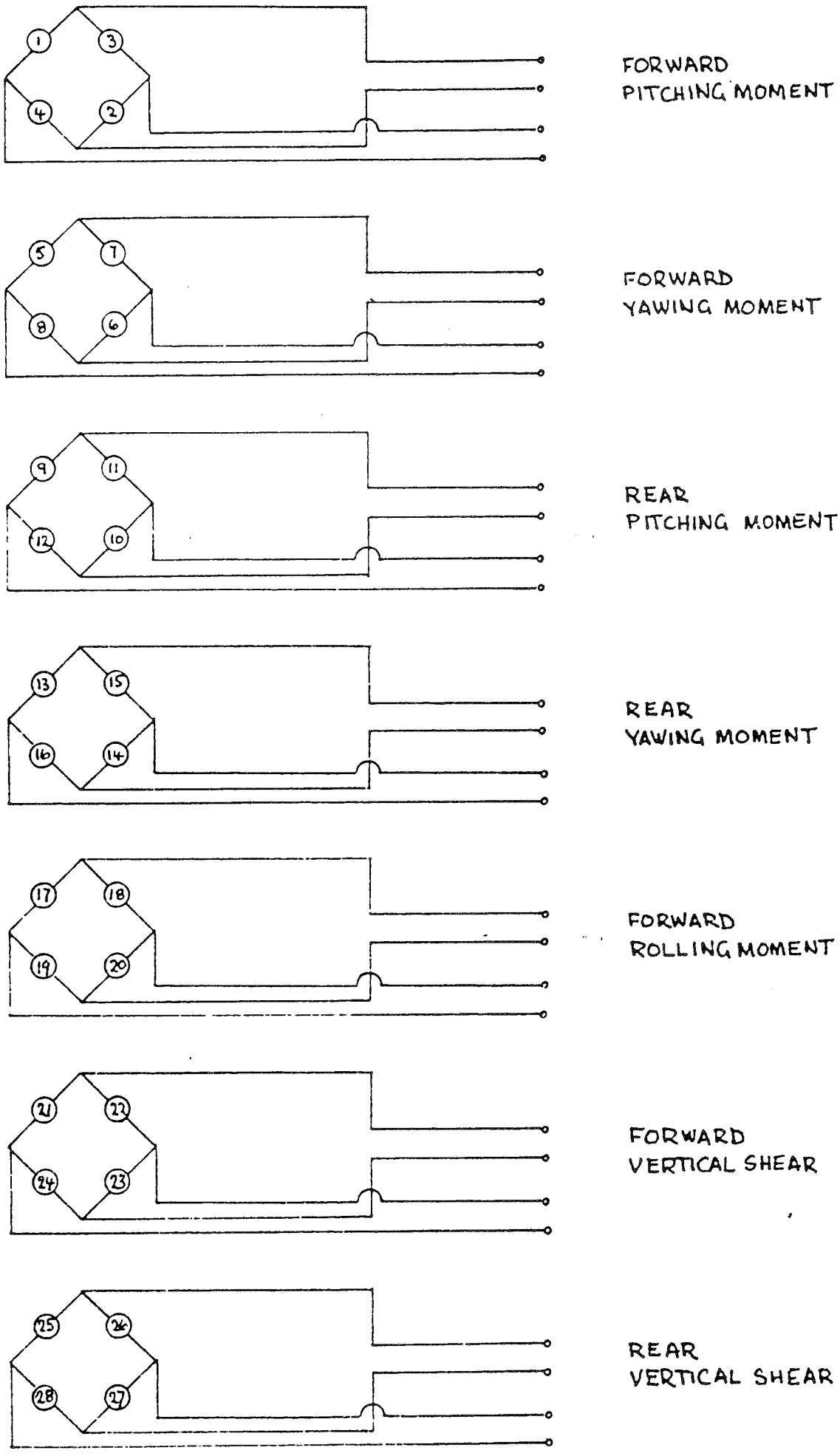

Figure 2.8 . Strain-gauge wiring diagram for steady-state experiments balance .

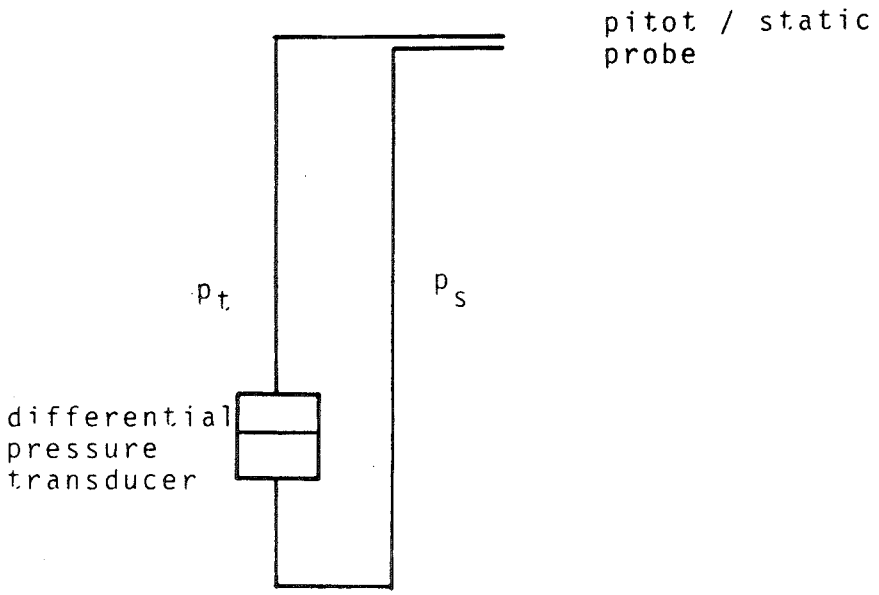

Figure 2.9 . Initial WA pressure measurement system .

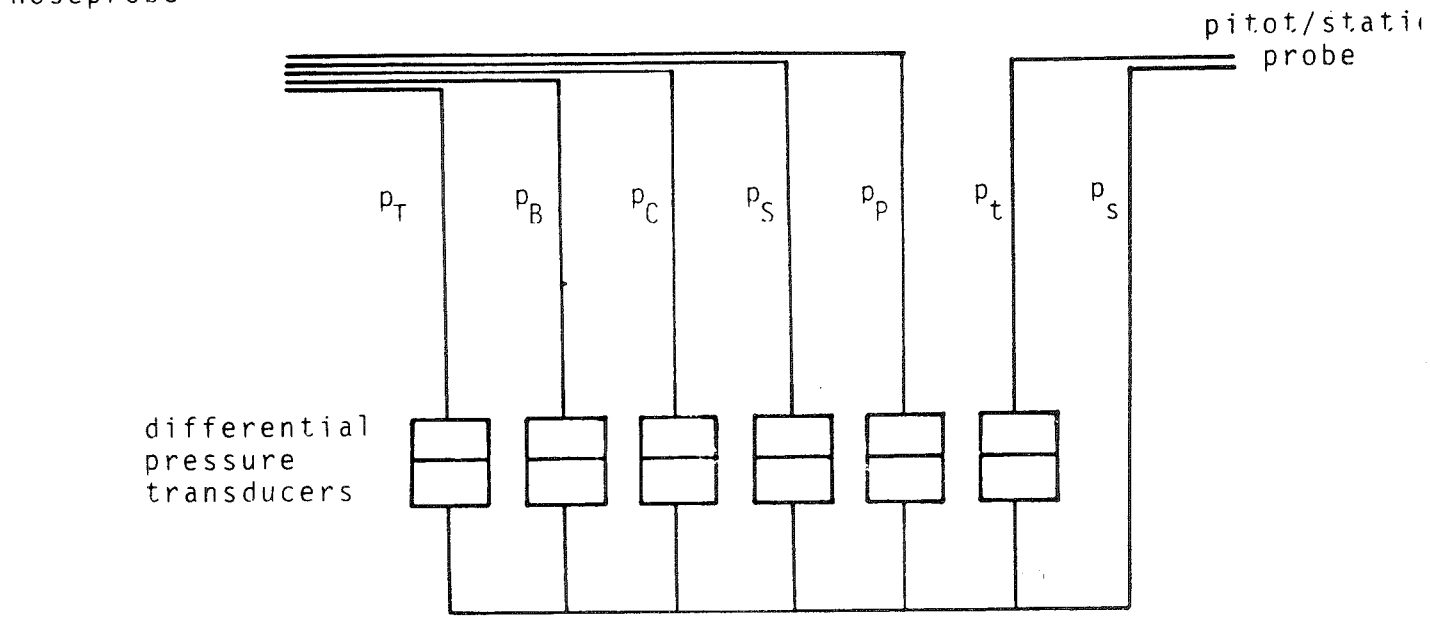

Figure 2.10 . WA pressure measurement system with noseprobe data .

NEXT PAGE:

Top: Figure 2.11

This picture shows the Model 2206 (HIRM I) in the Whirling Arm test passage. The wooden fairings over the end of the Arm structure, used to reduce swirl, can be seen. On the right hand side, parts of the incidence-changing mechanism can be seen. Just visible is one of the six sets of curtains, mounted to reduce swirl. The metal sheets seen on the outer wall of the test passage were used in earlier experiments not related to the HIRM project. They are not expected to have influenced the measurements on HIRM in a significant way.

Bottom: Figure 2.12

The Model 2206 supported by the cranked sting, used for high incidence measurements. The rubber sheets on the leading edge of the fairing are mounted in an attempt to reduce the swirl caused by the slot. Also visible is the nose probe, with its 5 hole hemispherical tip.

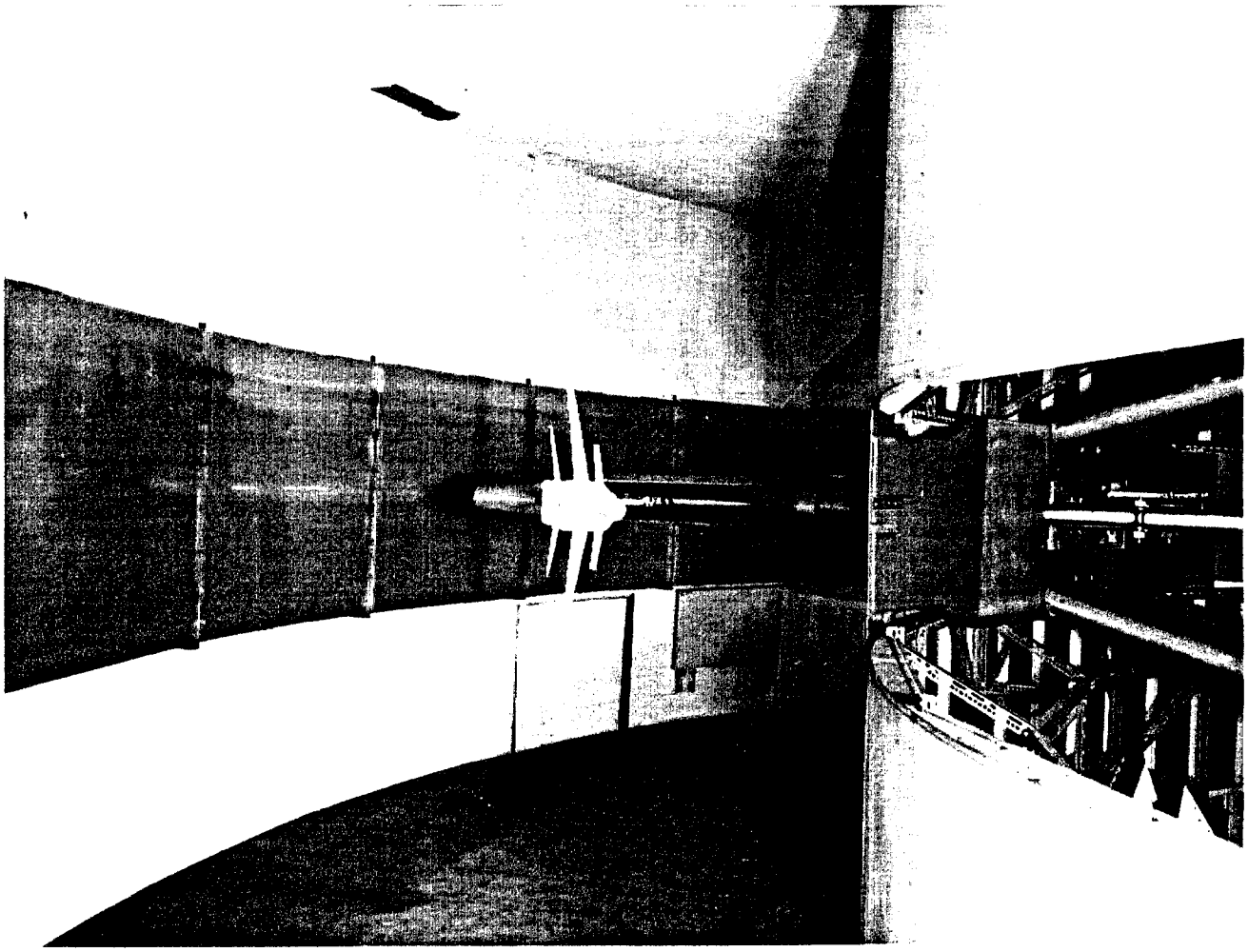

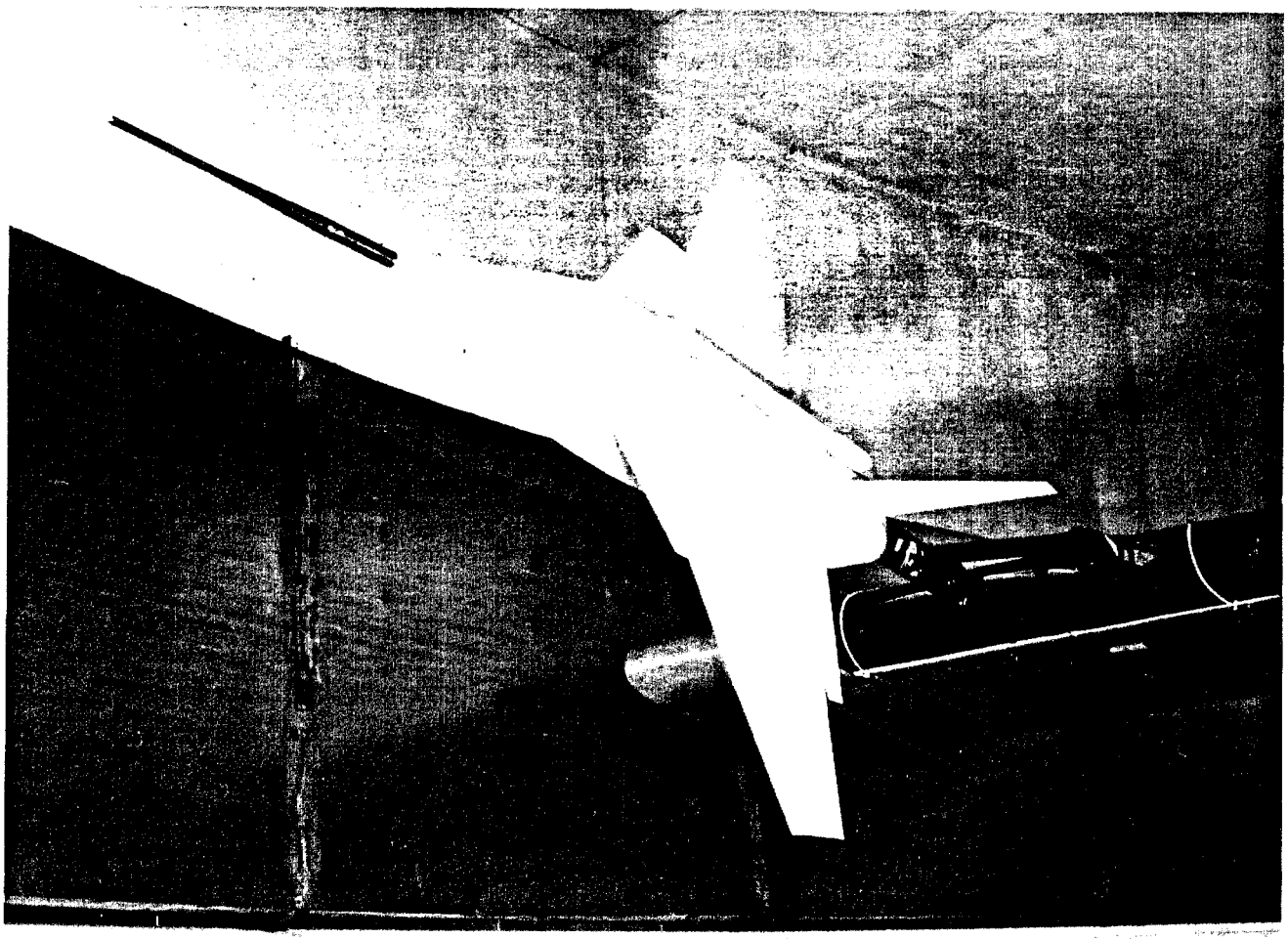

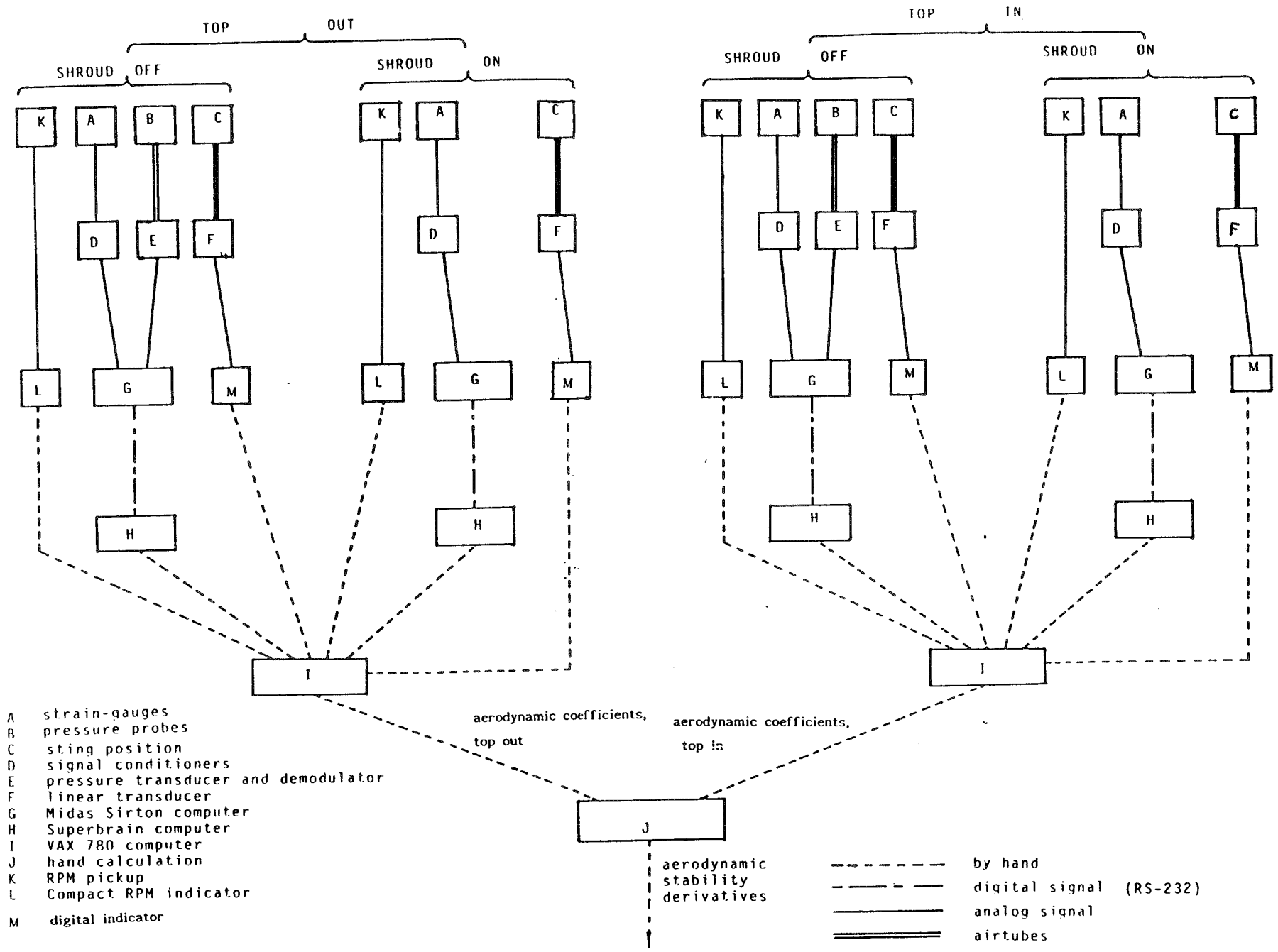

Figure 3.1 . General data reduction scheme as used for the steady-state experiments.

symbol	V (m/s)	$Re_{\bar{c}}$	model
□	19	5.0E5	2206
○	40	1.1E6	2206
×	70	1.9E6	2130

Figure 4.1 . HIRM I windtunnel measurement comparisons.

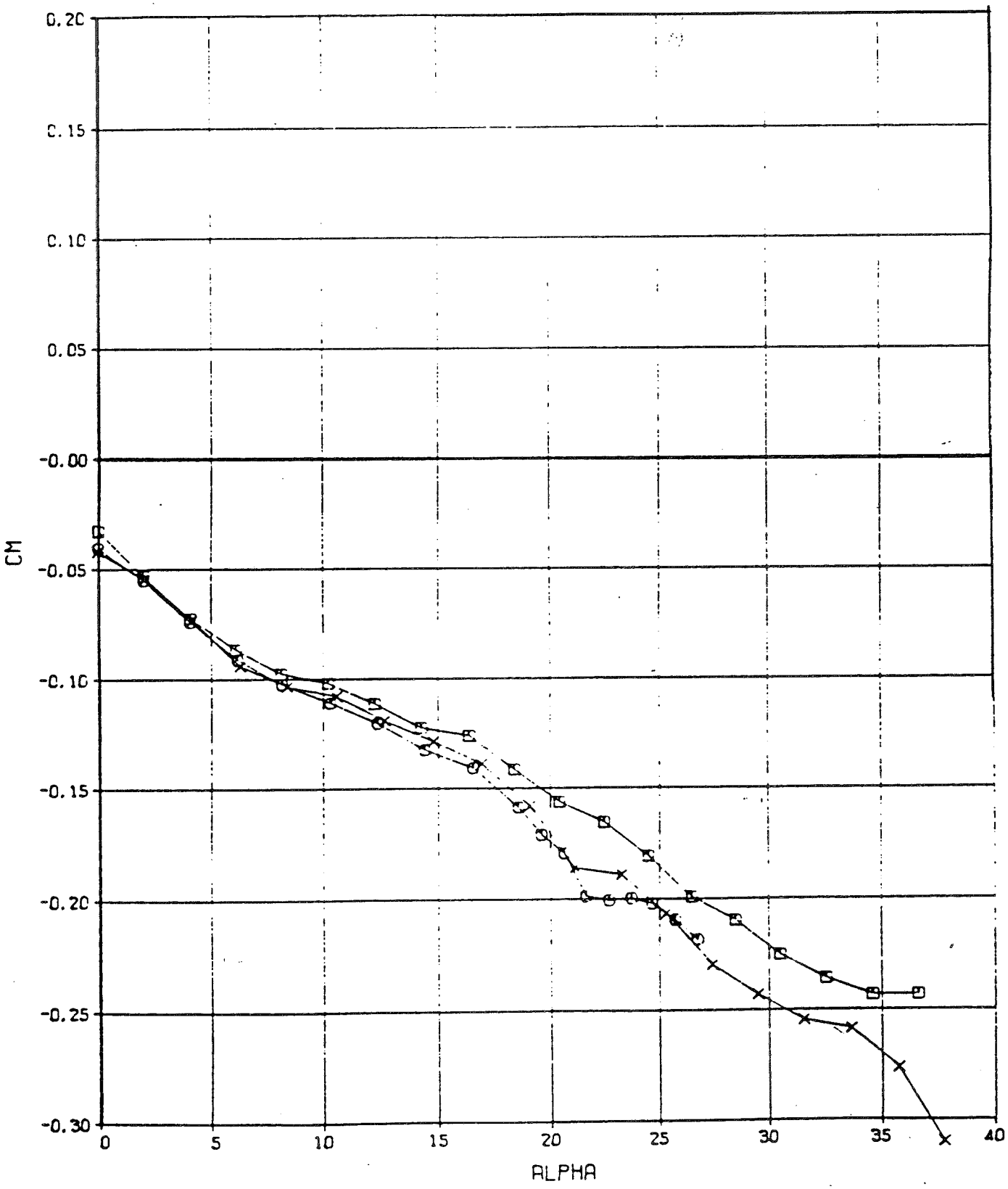

symbol	V (m/s)	$Re_{\bar{c}}$	model
□	19	5.0E5	2206
○	40	1.1E6	2206
×	70	1.9E6	2130

Figure 4.2 . HIRM I windtunnel measurements comparisons.

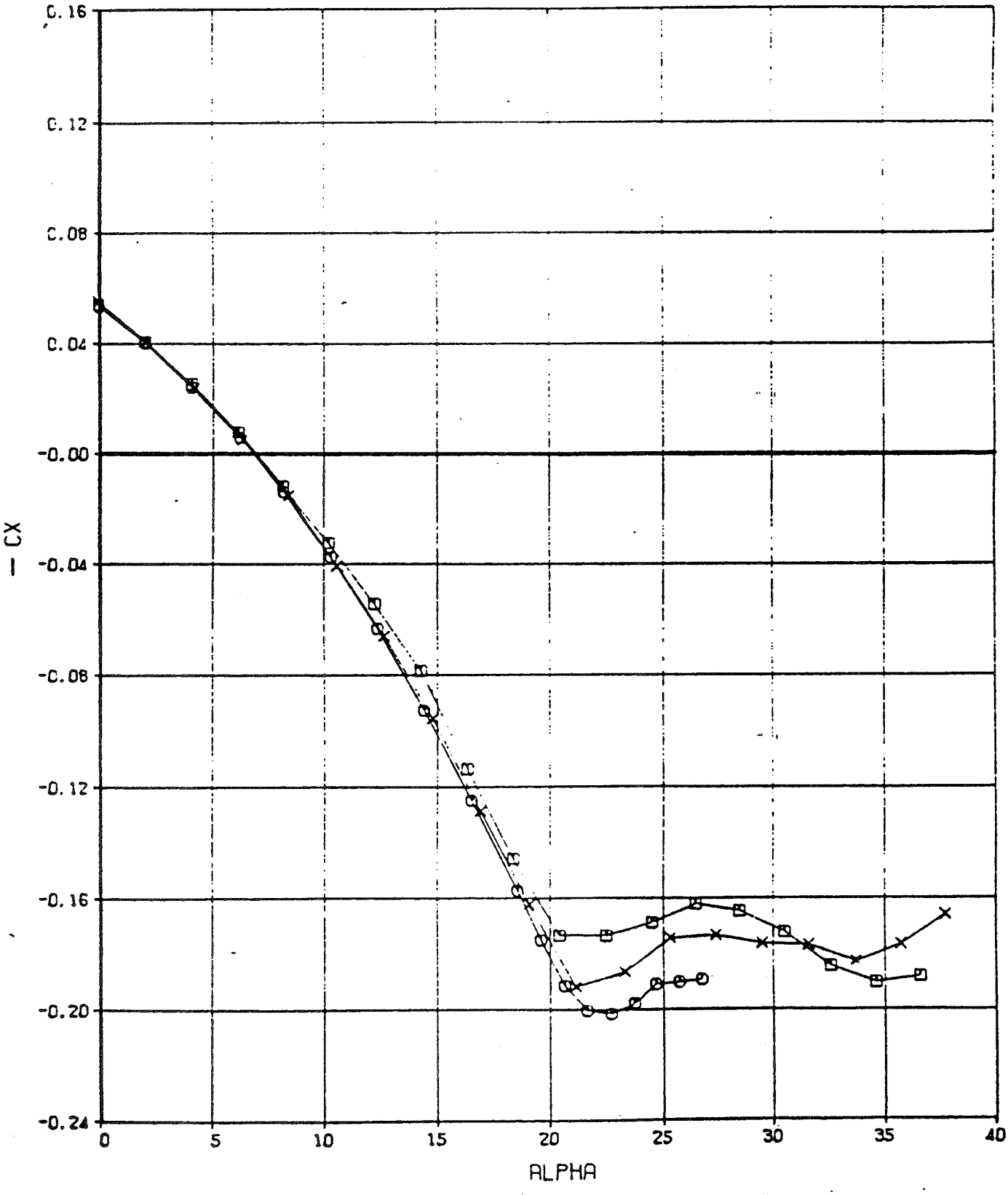

symbol	V (m/s)	Re_c	model
□	19	5.0E5	2206
○	40	1.1E6	2206
×	70	1.9E6	2130

Figure 4.3 . HIRM I windtunnel measurements comparisons.

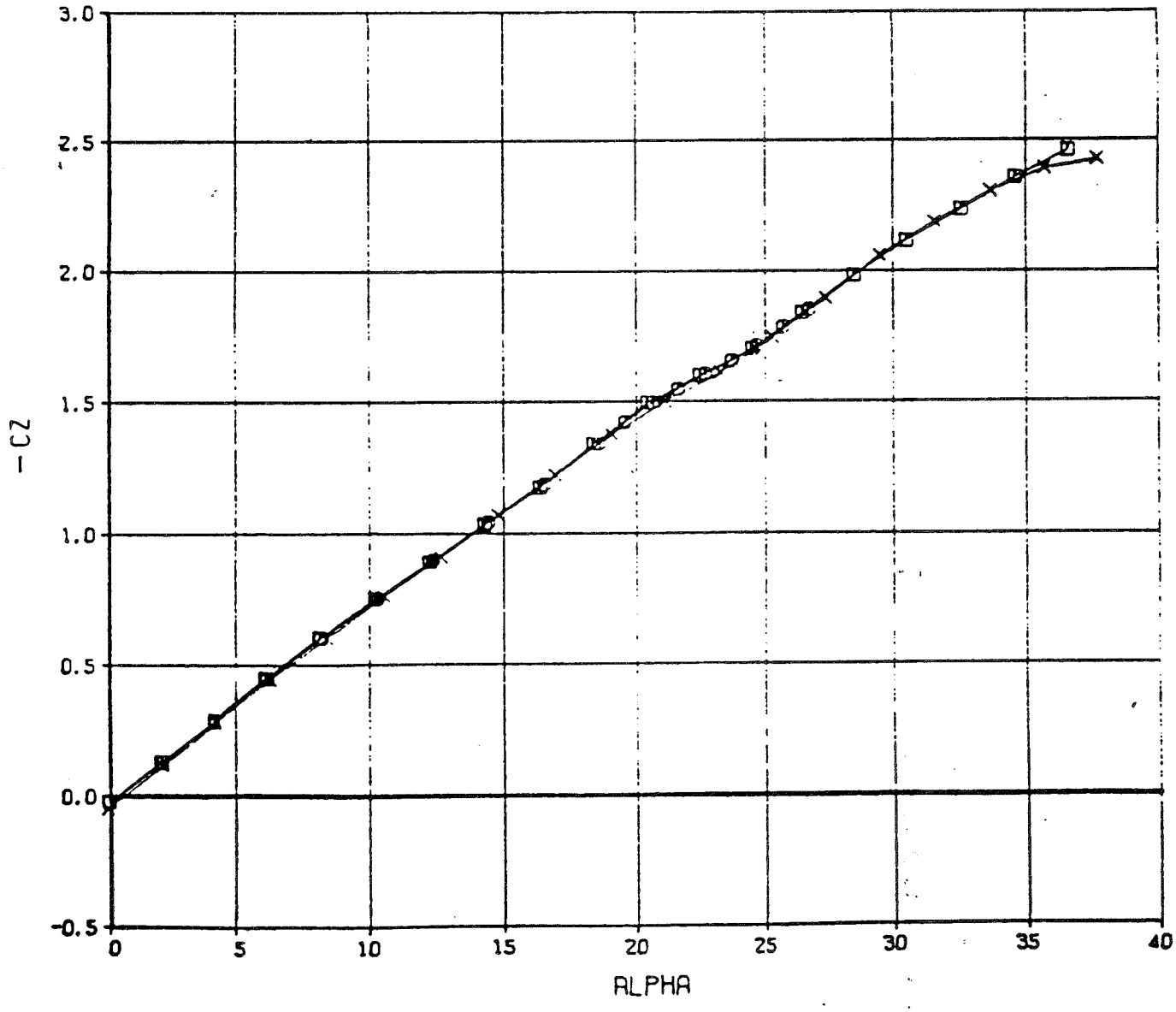

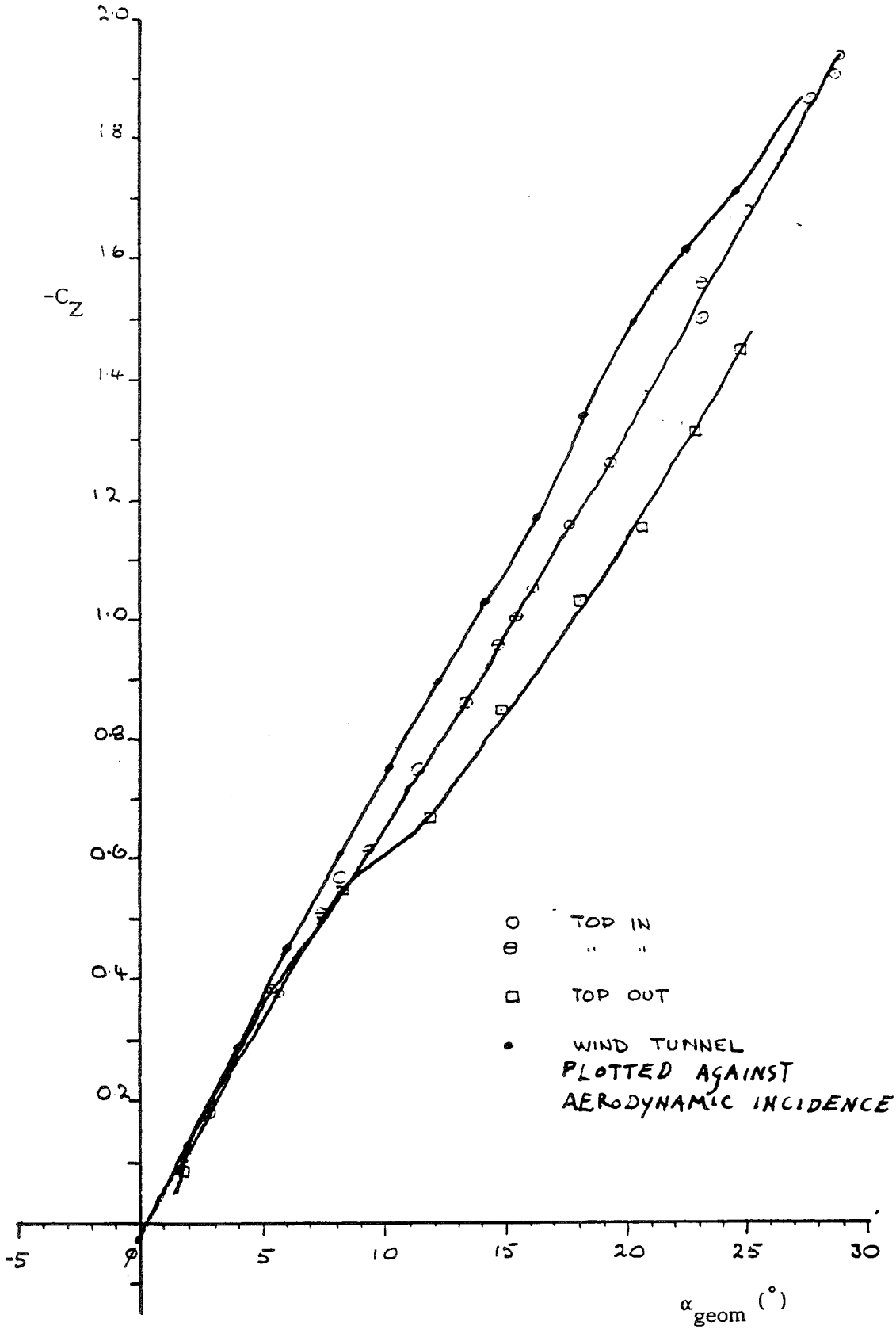

Figure 4.4. Normal force coefficient, using pitot/static probe

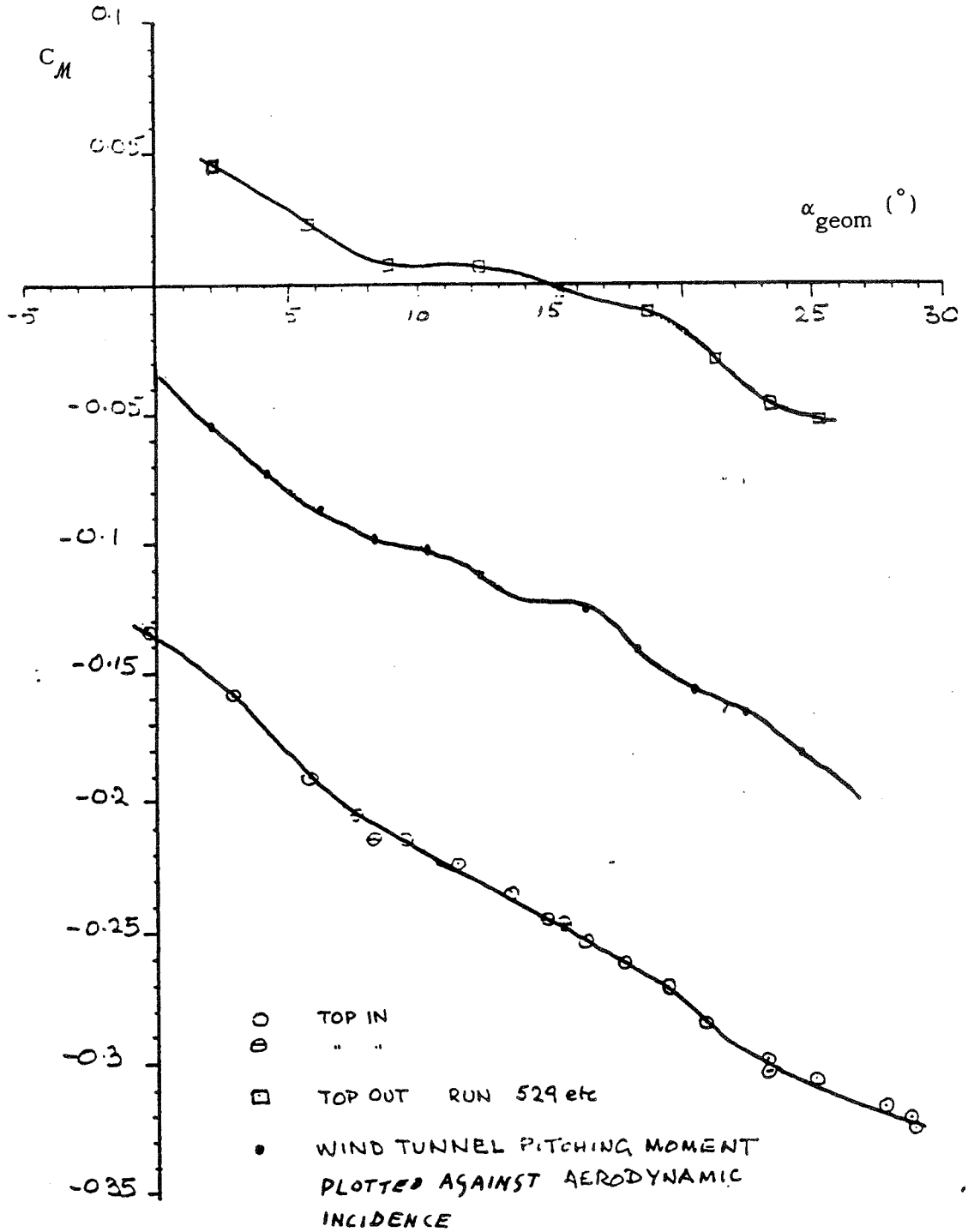

MRC = $0.125\bar{c}$

Figure 4.5. Pitching moment coefficient, using pitot/static probe

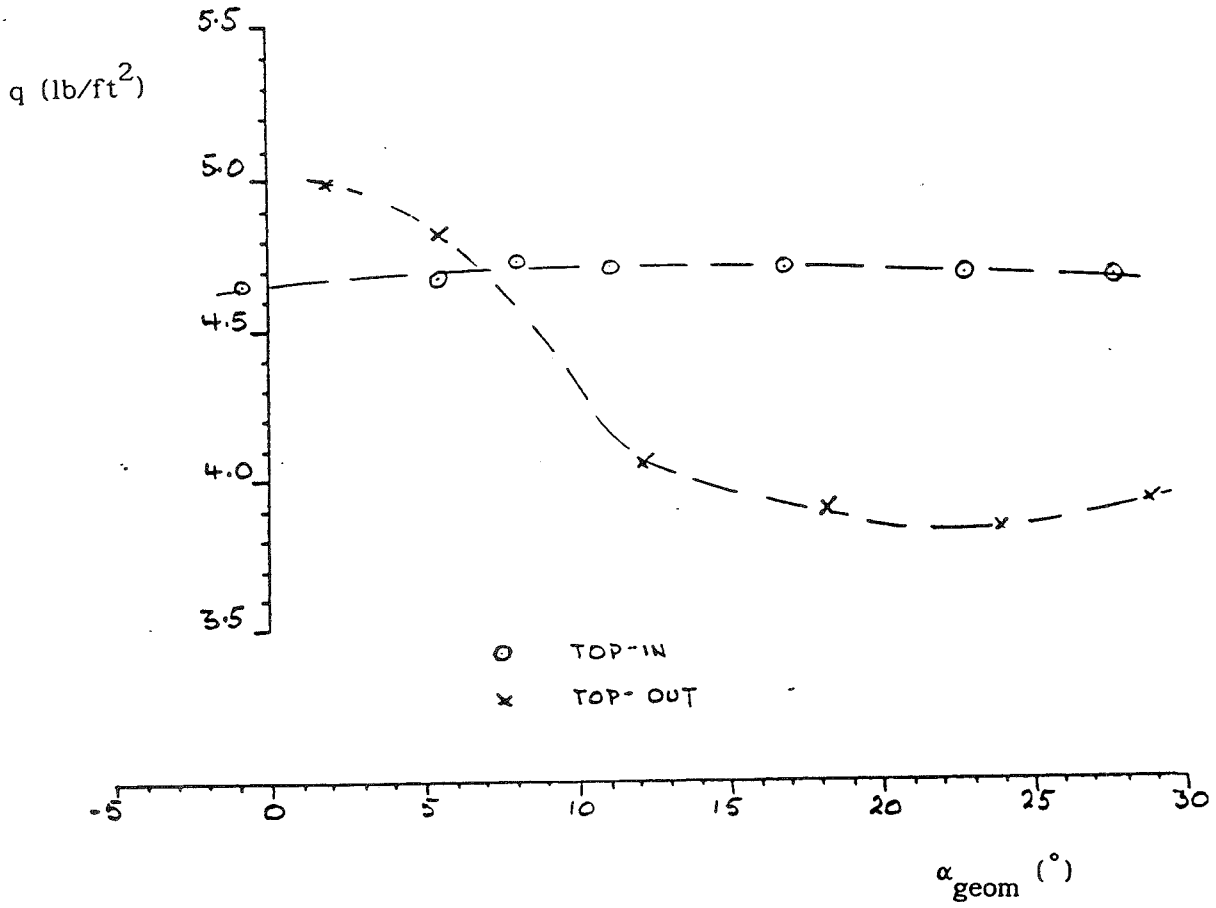

Figure 4.6. Dynamic head as sensed by pitot/static tube. Shroud on

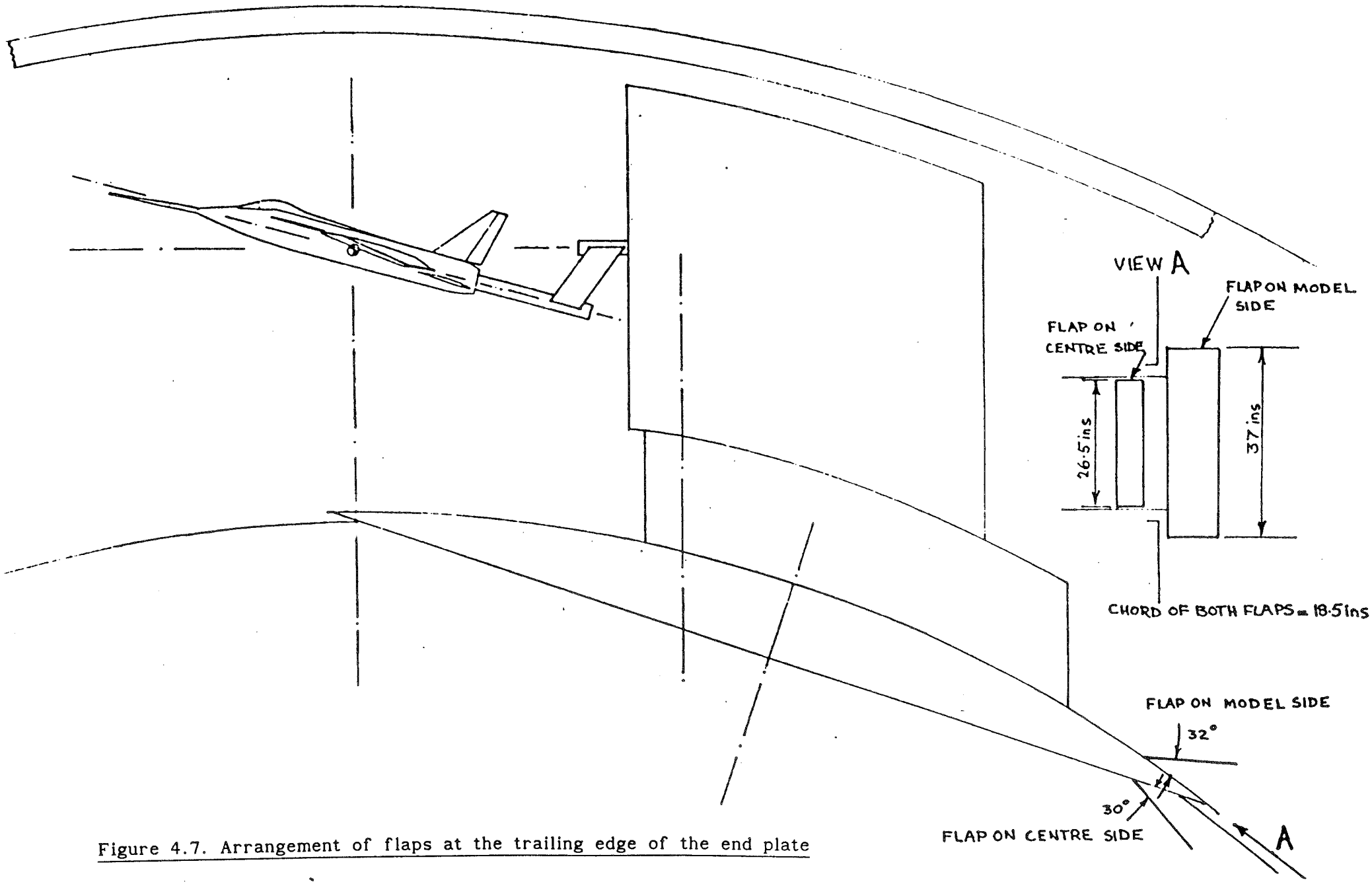

Figure 4.7. Arrangement of flaps at the trailing edge of the end plate

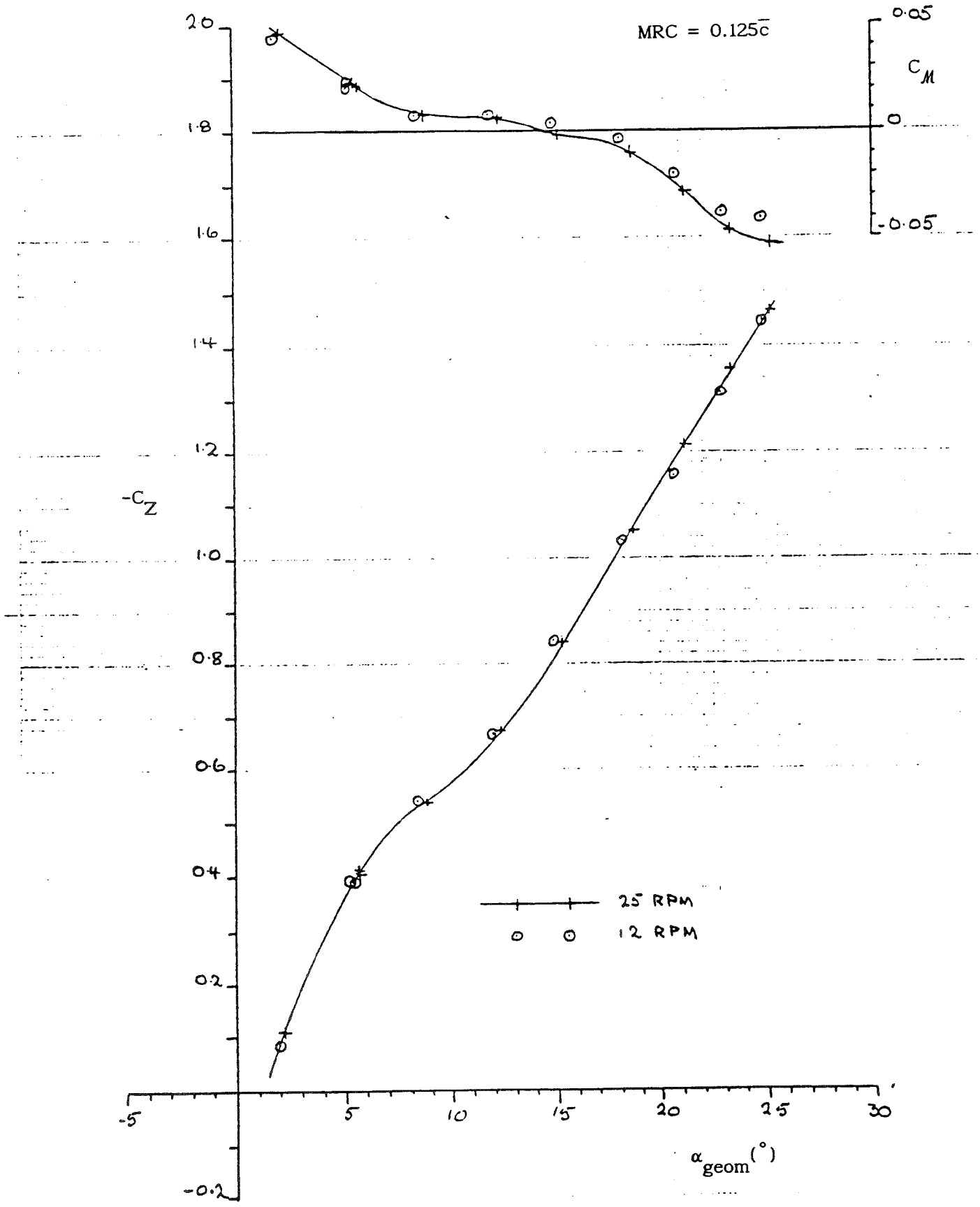

Figure 4.8. Normal force- and pitching moment coefficients at 12 and 25 rpm. Top out attitude. (Pitot/static pressures from opposite side arm.)

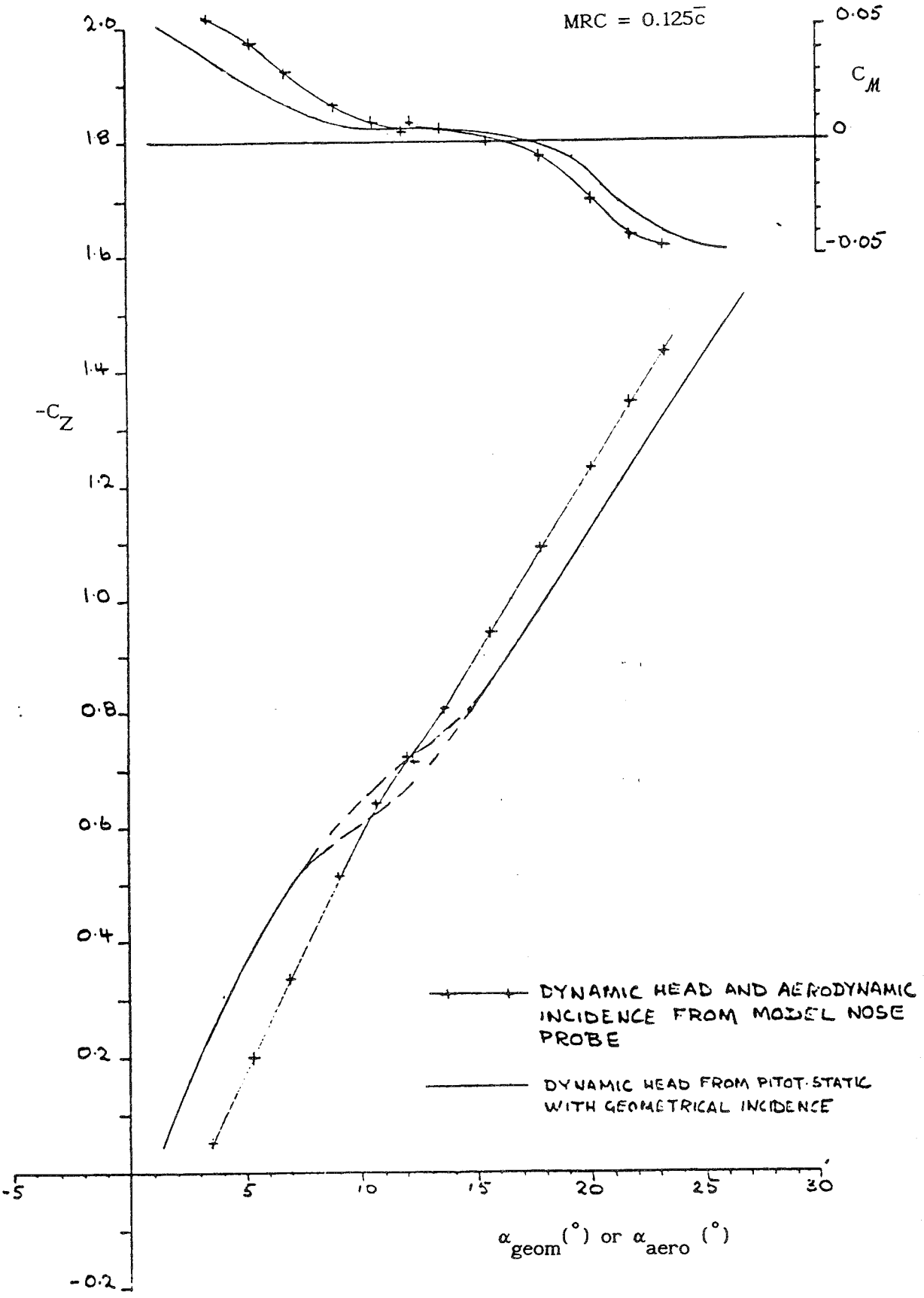

Figure 4.9. Normal force- and pitching moment coefficient using different air-sensors. Model top-out attitude

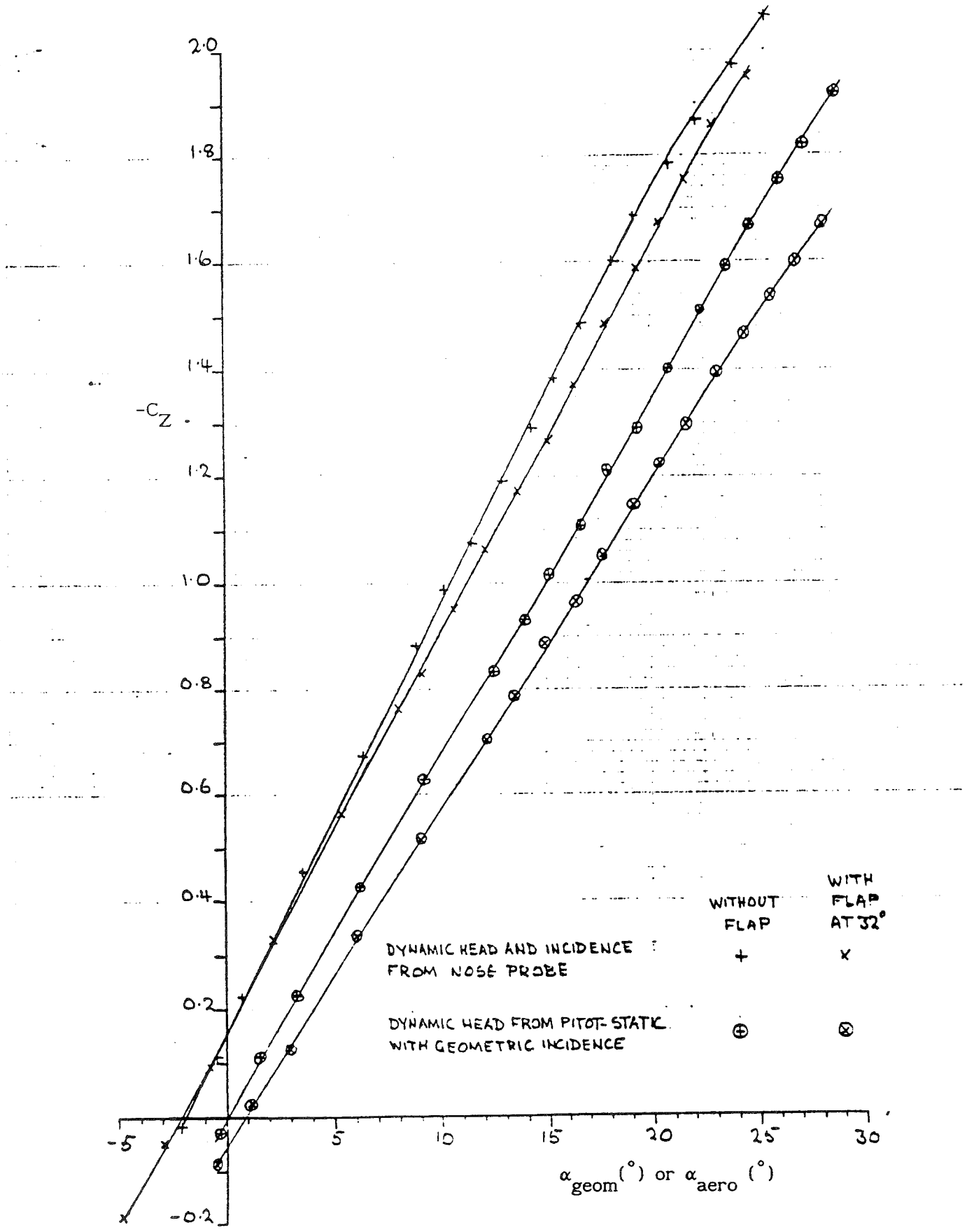

Figure 4.10. Normal force coefficient. Model top-in attitude. With and without flap on end plate, model side

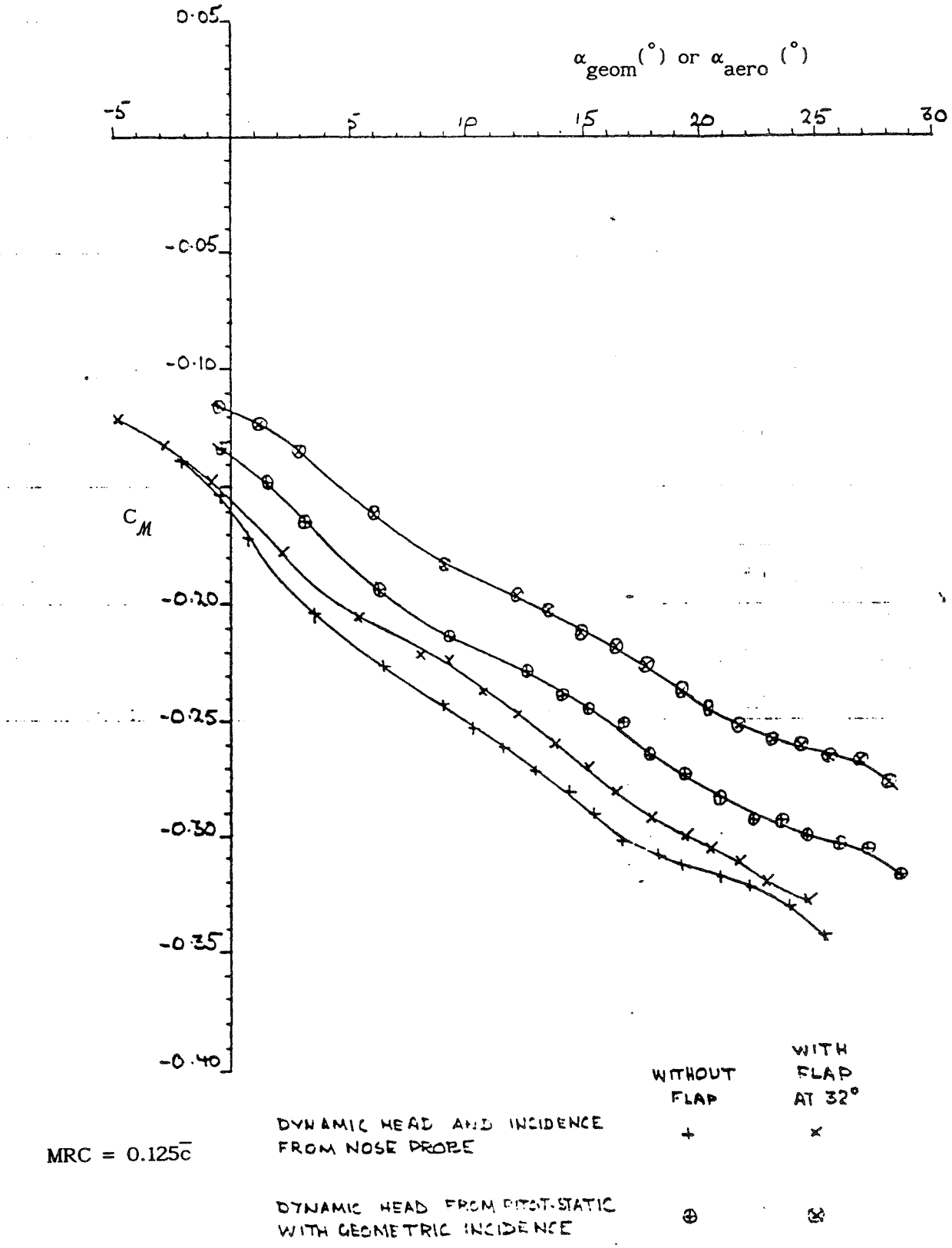

Figure 4.11. Pitching moment coefficients. Model top-in attitude. With and without flap on end plate, model side.

MRC = $0.125\bar{c}$

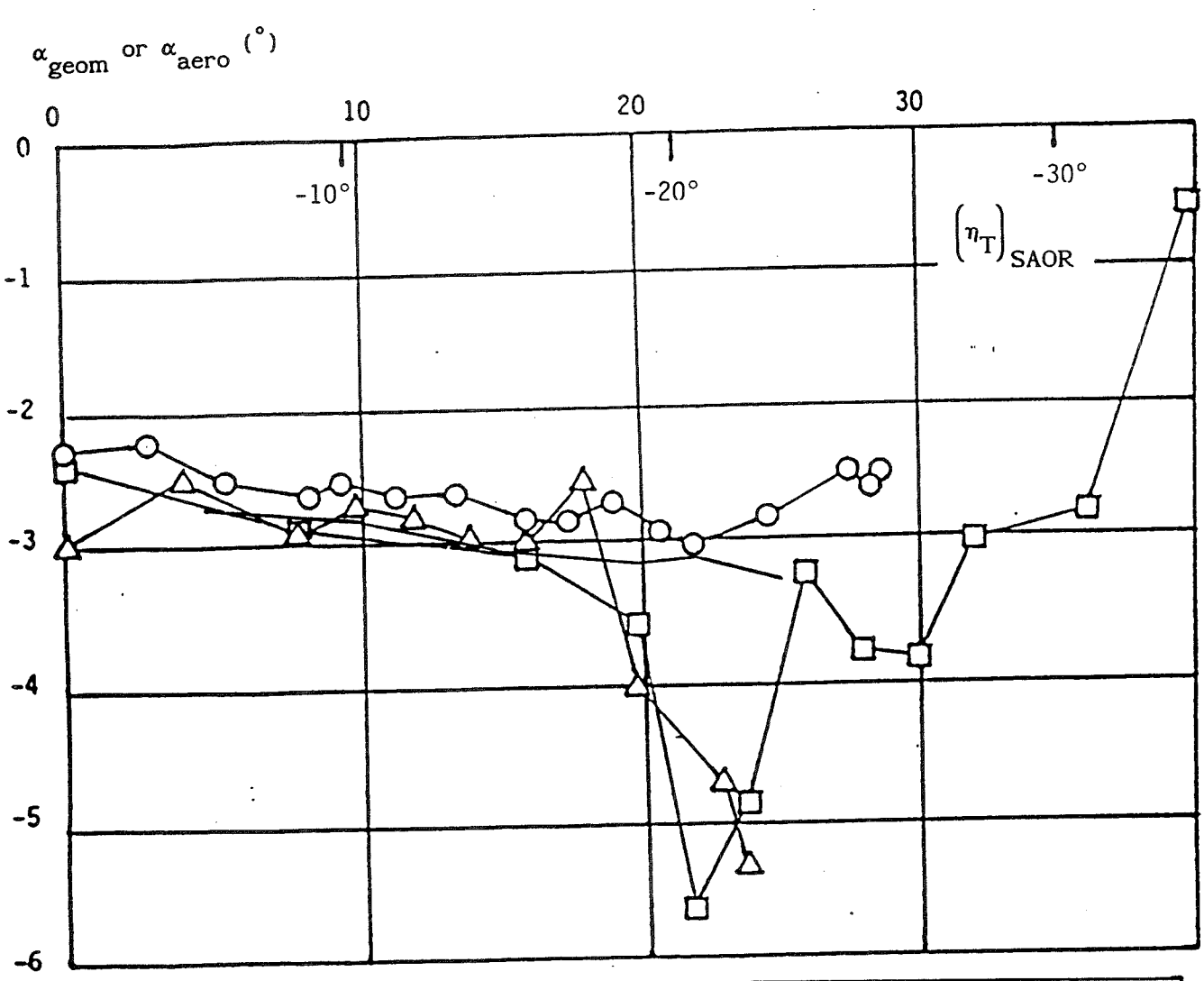

symbol	V(m/s)	$Re_{\bar{c}}$	model	η_C	η_T	facility	quantity
△	70	1.9×10^6	2130	0°	trim	SAOR	$\check{M}_q+\check{M}_{\dot{w}}\cos\alpha$
□	40	1.1×10^6	2130	0°	trim	SAOR	$\check{M}_q+\check{M}_{\dot{w}}\cos\alpha$
○	22	5.8×10^5	2206	0°	0°	WA	$\check{M}_q$ †
—	22	5.8×10^5	2206	0°	0°	WA	$\check{M}_q$ ‡

† These values are derived from coefficients obtained using the pitot-static probe. Geometric incidence used on horizontal axis.

‡ These values are derived from coefficients obtained using the 5-hole nose probe. Aerodynamic incidence used on horizontal axis.

Figure 4.12. Comparison of measurements of damping in pitch, HIRM I.

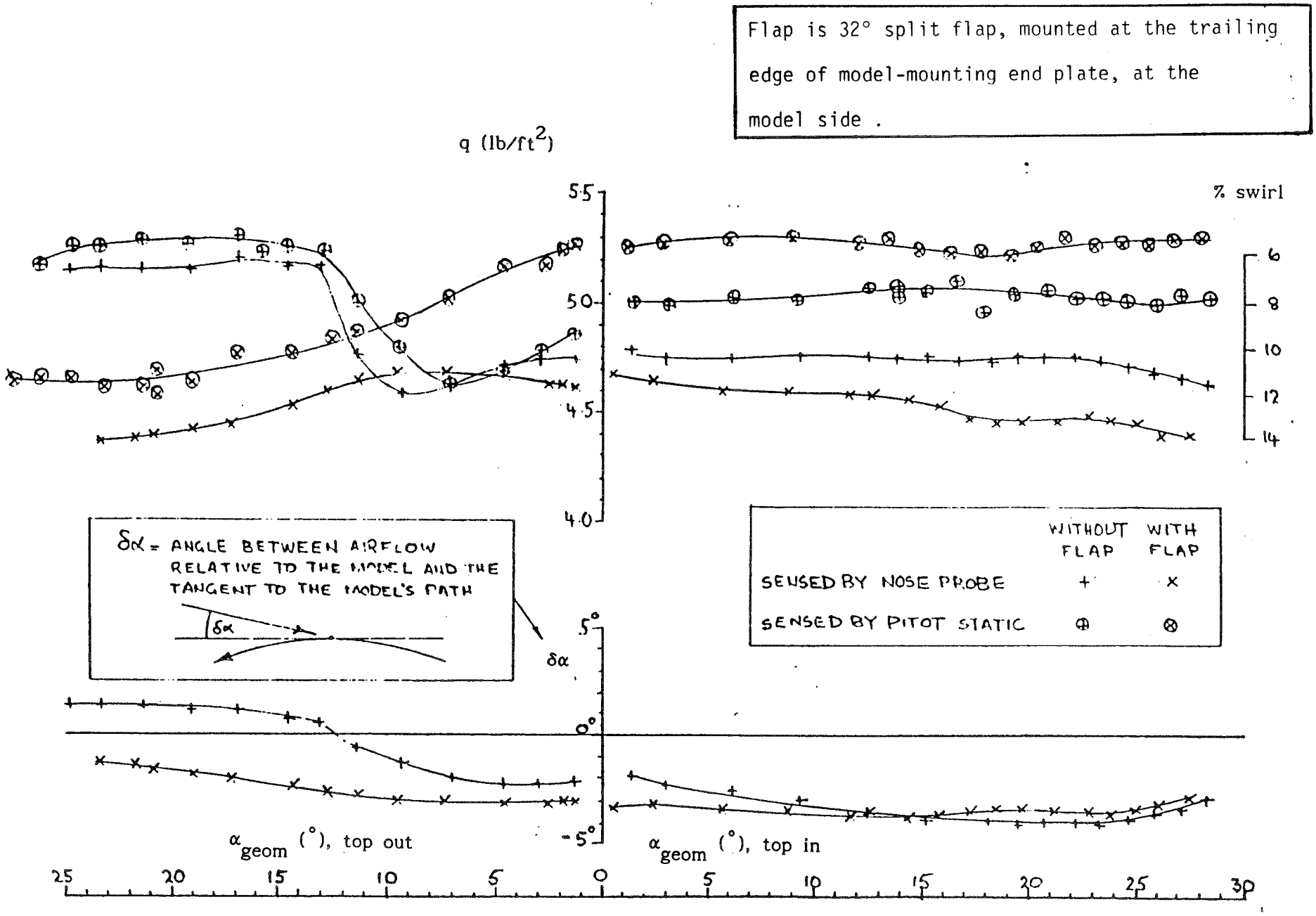

Figure 4.13. Dynamic head and flow direction in test passage at 25 rpm

symbol	$\frac{q\bar{c}}{V}$	position	$Re_{\bar{c}}$	model	η_c	η_F	facility
⊙	.067	top in	8.3E5	2254	0	0	WA
⊡	0.0	neutral	1.5E6	2201	0	0	static, windtunnel
◈	-.067	top out	8.3E5	2254	0	0	WA

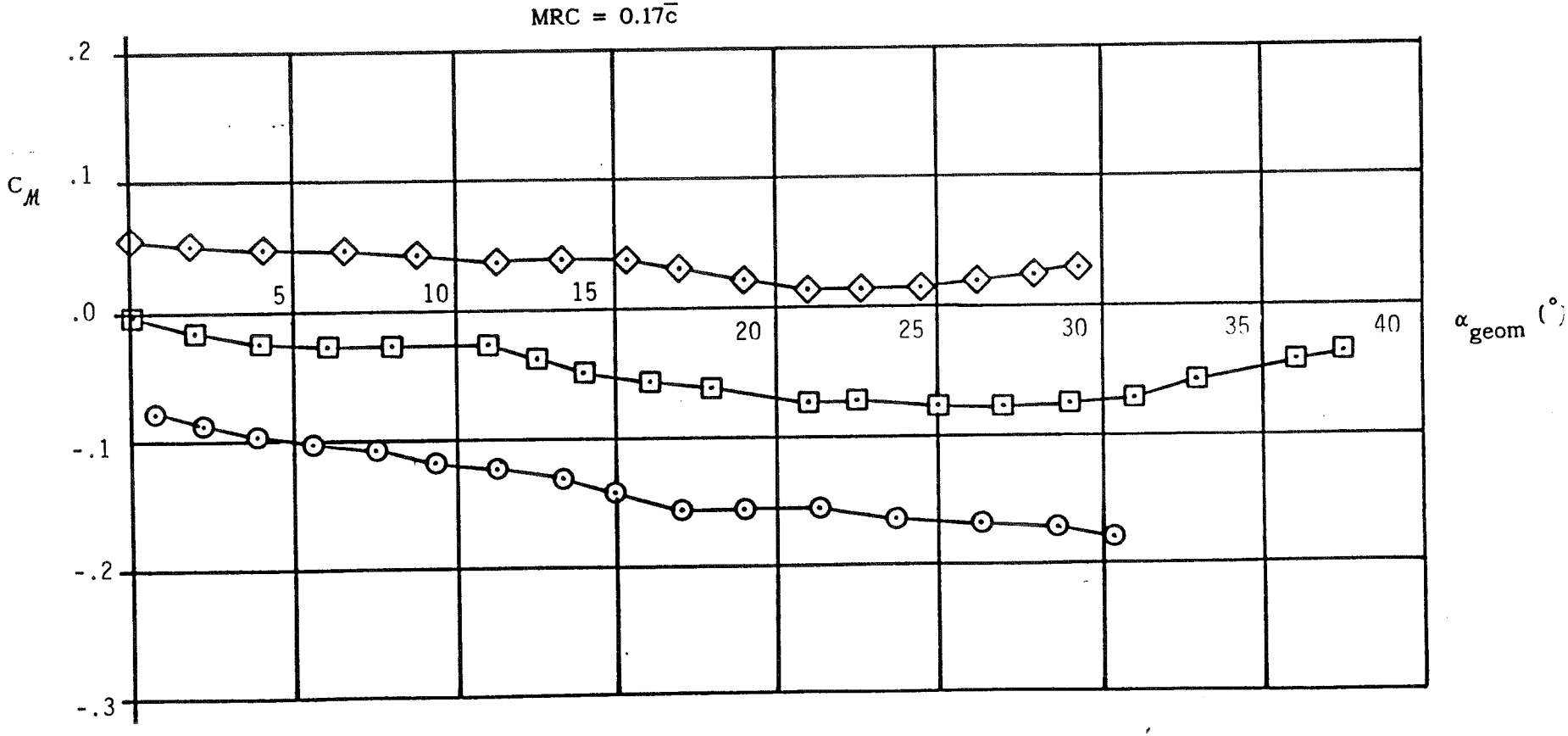

Figure 4.14. HIRM II pitching moment coefficients

MRC = $0.17\bar{c}$

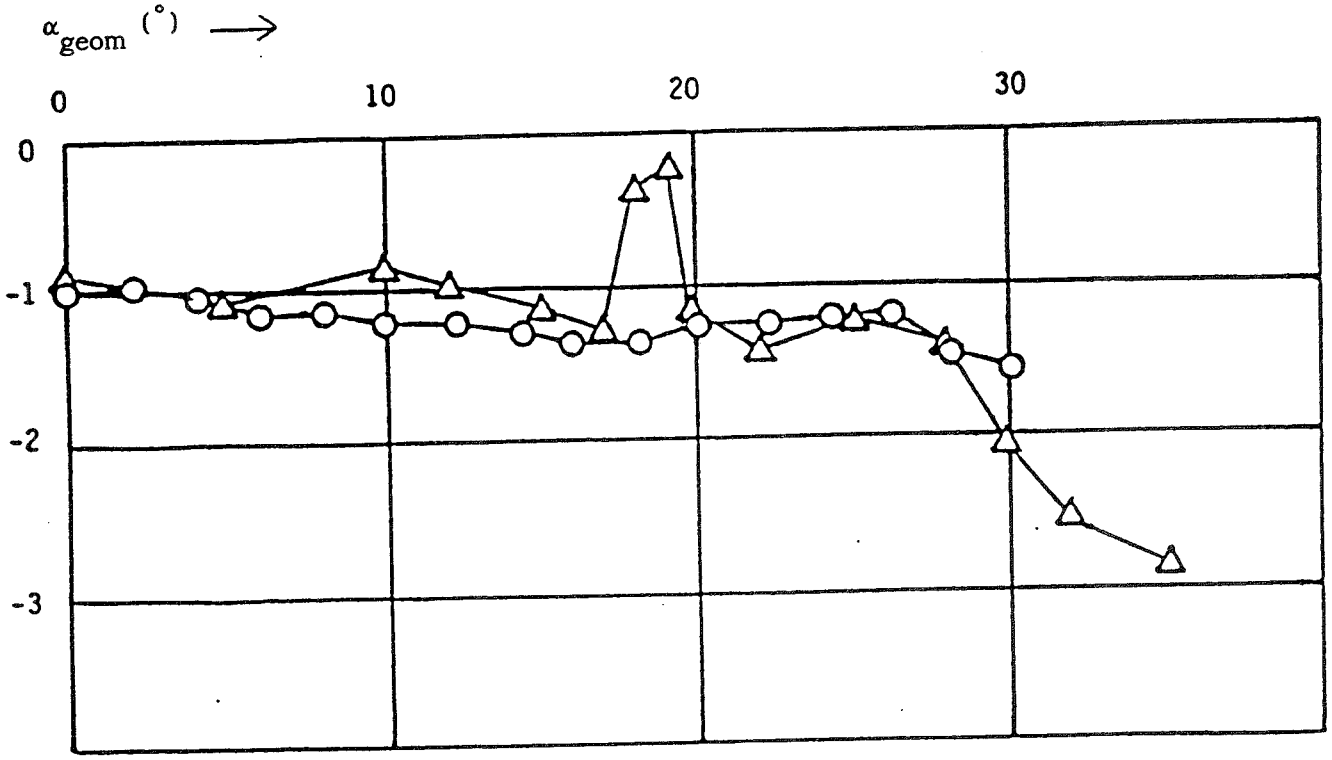

symbol	$Re_{\bar{c}}$	model	η_C	η_F	facility	quantity
△	1.5×10^6	2201	0°	0°	LAPR	$M_q + M_{\dot{w}} \cos\alpha$
○	8.3×10^5	2254	0°	0°	WA	M_q

Figure 4.15. Damping in pitch comparisons, HIRM II

HIRM I

MRC = .125 $\bar{c}$

Aerodynamic body axes

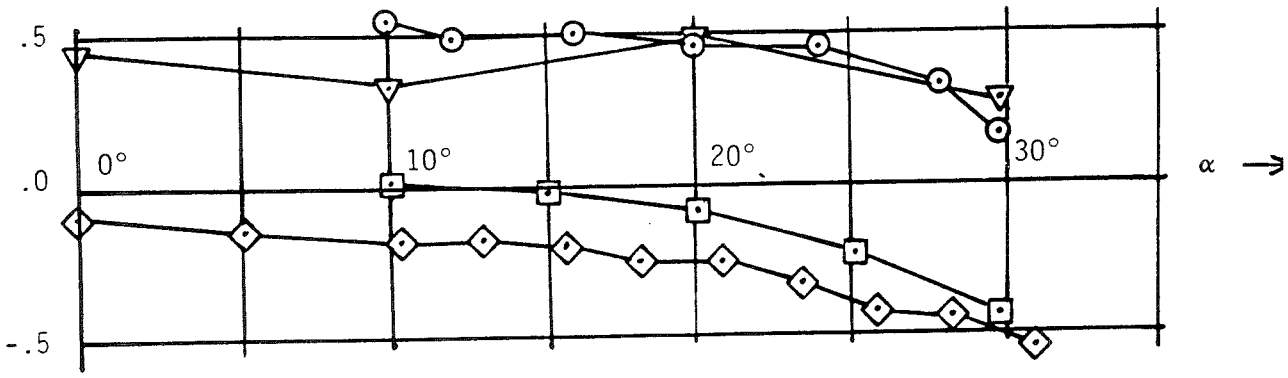

symbol	quantity	facility	$Re_{\bar{c}}$	model	η_C	η_T	$\frac{rb}{V}$
⊙	$\check{Y}_r - \check{Y}_{\dot{v}}$	SAOR	1.05×10^6 1.85×10^6	2130	-10°	-20°	0.015 0.025
▽	$\check{Y}_r - \check{Y}_{\dot{v}}$	SAOR	1.05×10^6 1.85×10^6	2130	0°	0°	0.015 0.025
⊡	$\left(\check{Y}_r\right)_{WA} - \left(\check{Y}_{\dot{v}}\right)_{ADR}$	WA →	5.8×10^5	2206	0°	0°	0.139
		ADR →	7.9×10^5	2206	-10°	-20°	-
◇	$\check{Y}_r$	WA	5.8×10^5	2206	0°	0°	0.139

Figure 4.16. Comparison of angular velocity results

HIRM I

MRC = .125 $\bar{c}$

Aerodynamic body axes

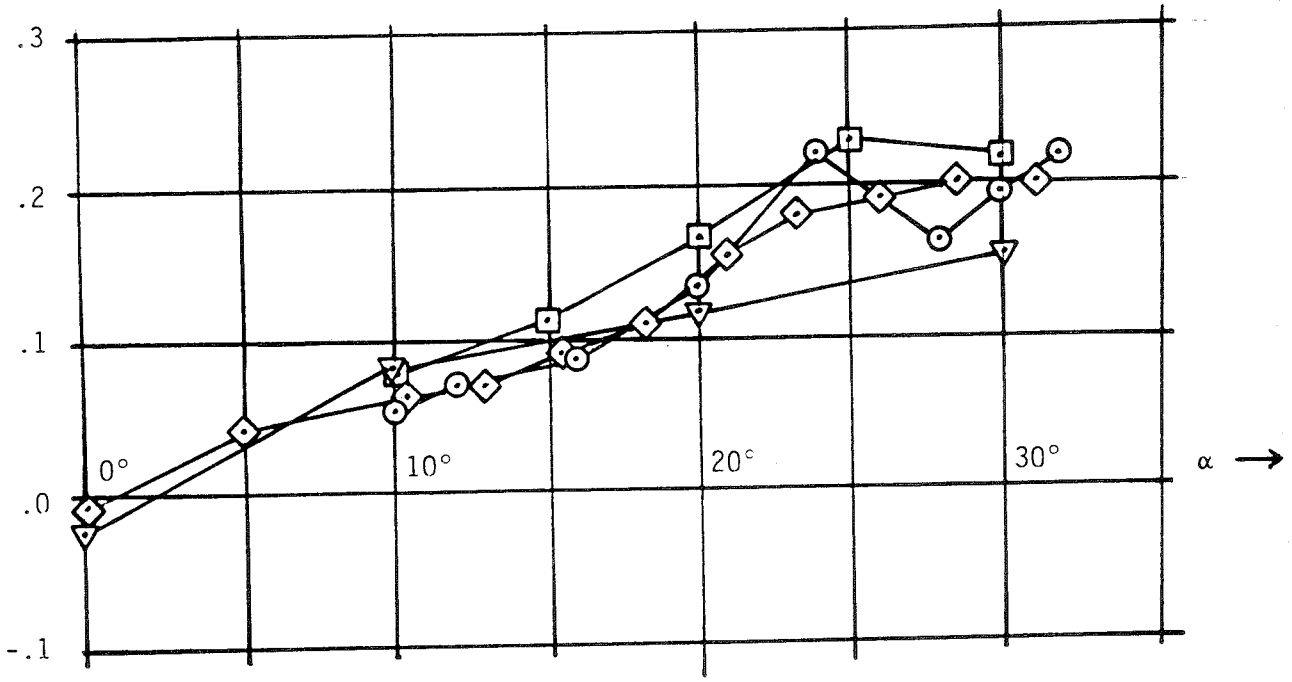

symbol	quantity	facility	$Re_{\bar{c}}$	model	η_C	η_T	$\frac{rb}{V}$
⊙	$\breve{\varphi}_r - \breve{\varphi}_{\dot{v}}$	SAOR	1.05×10^6 1.85×10^6	2130	-10°	-20°	0.015 0.025
▽	$\breve{\varphi}_r - \breve{\varphi}_{\dot{v}}$	SAOR	1.05×10^6 1.85×10^6	2130	0°	0°	0.015 0.025
⊡	$\left(\breve{\varphi}_r\right)_{WA} - \left(\breve{\varphi}_{\dot{v}}\right)_{ADR}$	WA → ADR →	5.8×10^5 7.9×10^5	2206 2206	0° -10°	0° -20°	0.139 - ,
◇	$\breve{\varphi}_r$	WA	5.8×10^5	2206	0°	0°	0.139

Figure 4.17. Comparison of angular velocity results

HIRM I

MRC = .125$\bar{c}$

Aerodynamic body axes

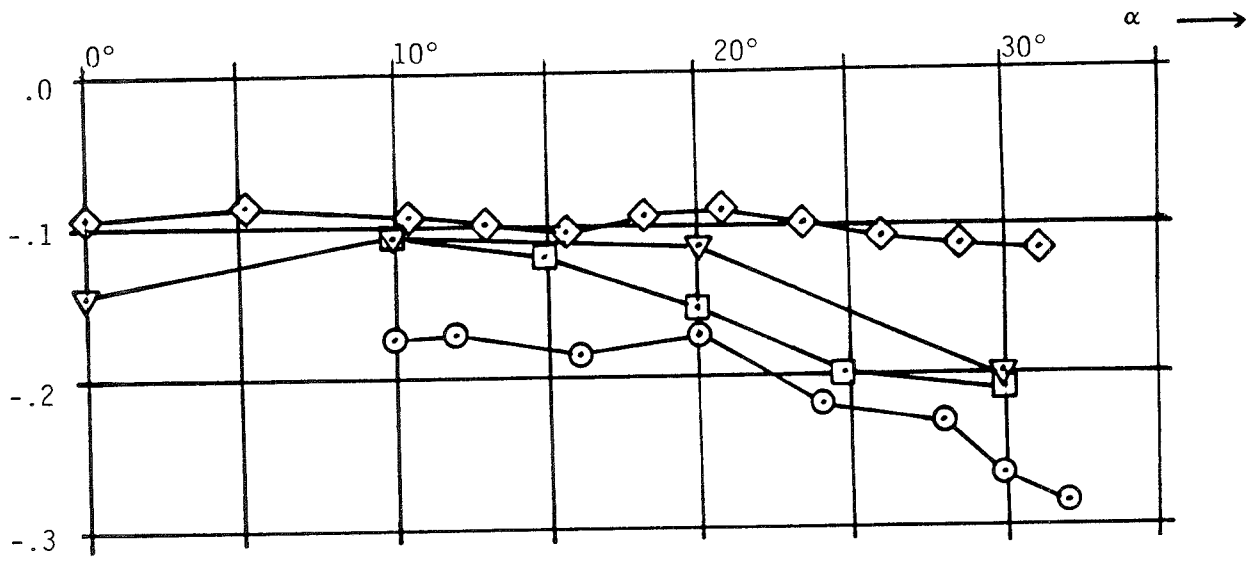

symbol	quantity	facility	$Re_{\bar{c}}$	model	η_C	η_T	$\frac{rb}{V}$
⊙	$\check{N}_r - \check{N}_{\dot{v}}$	SAOR	1.05×10^6 1.85×10^6	2130	-10°	-20°	0.015 0.025
▽	$\check{N}_r - \check{N}_{\dot{v}}$	SAOR	1.05×10^6 1.85×10^6	2130	0°	0°	0.015 0.025
⊡	$\left(\check{N}_r\right)_{WA} - \left(\check{N}_{\dot{v}}\right)_{ADR}$	WA → ADR →	5.8×10^5 7.9×10^5	2206 2206	0° -10°	0° -20°	0.139 -
◇	$\check{N}_r$	WA	5.8×10^5	2206	0°	0°	0.139

Figure 4.18. Comparison of angular velocity results

HIRM I

MRC = .125$\bar{c}$

Geometric body axes

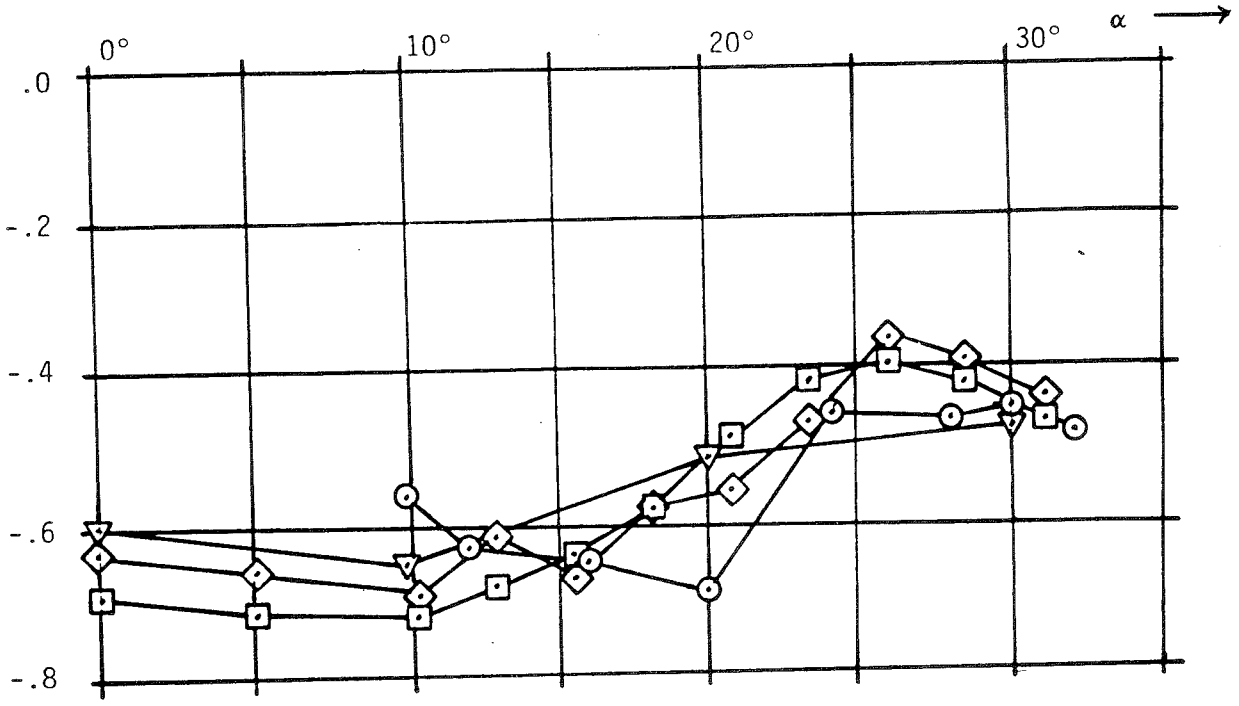

symbol	quantity	facility	$Re_{\bar{c}}$	model	η_C	η_T
⊙	$\check{Y}_v$	SAOR	1.05×10^6 1.85×10^6	2130	-10°	-20°
▽	$\check{Y}_v$	SAOR	1.05×10^6 1.85×10^6	2130	0	0
⊡	$\check{Y}_v$	WA (pos. β)	5.8×10^5	2206	0	0
◇	$\check{Y}_v$	WA (neg. β)	5.8×10^5	2206	0	0

Figure 4.19. Comparison of side-slip derivative results

HIRM I

MRC = .125$\bar{c}$

Geometric body axes

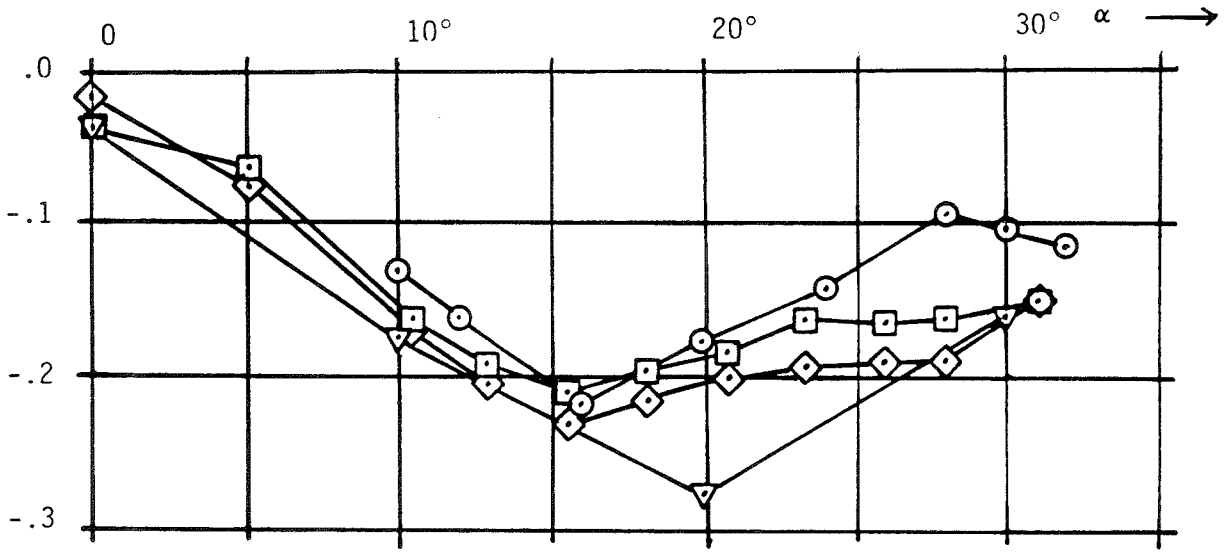

symbol	quantity	facility	$Re_{\bar{c}}$	model	η_C	η_T
⊙	$\check{\varphi}_v$	SAOR	1.05×10^6 1.85×10^6	2130	-10°	-20°
▽	$\check{\varphi}_v$	SAOR	1.05×10^6 1.85×10^6	2130	0	0
⊡	$\check{\varphi}_v$	WA (pos. β)	5.8×10^5	2206	0	0
◇	$\check{\varphi}_v$	WA (neg. β)	5.8×10^5	2206	0	0

Figure 4.20. Comparison of side-slip derivative results

HIRM I

MRC = .125$\bar{c}$

Geometric body axes

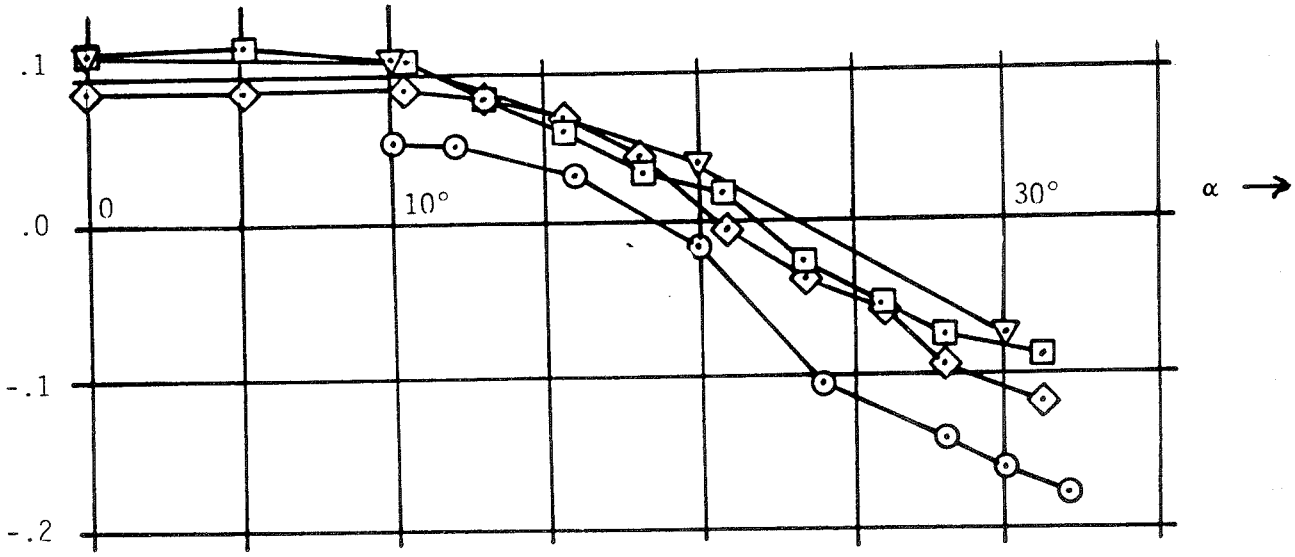

symbol	quantity	facility	$Re_{\bar{c}}$	model	η_C	η_T
⊙	$\check{N}_v$	SAOR	1.05×10^6 1.85×10^6	2130	-10°	-20°
▽	$\check{N}_v$	SAOR	1.05×10^6 1.85×10^6	2130	0	0
⊡	$\check{N}_v$	WA (pos. β)	5.8×10^5	2206	0	0
◇	$\check{N}_v$	WA (neg. β)	5.8×10^5	2206	0	0

Figure 4.21. Comparison of side-slip derivative results

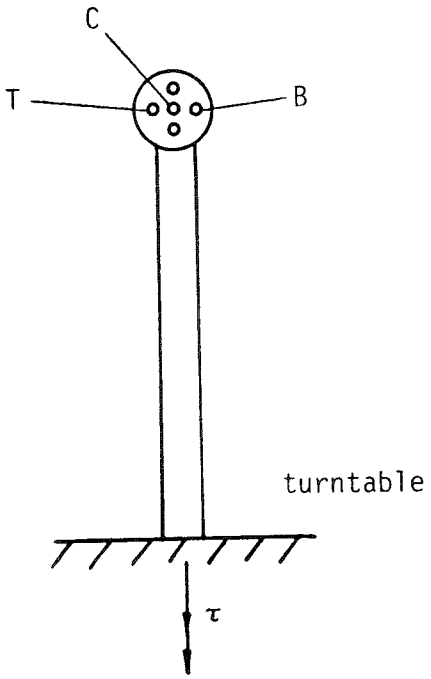

Figure A2.1 . Frontal view of 5-hole noseprobe in calibration set-up .

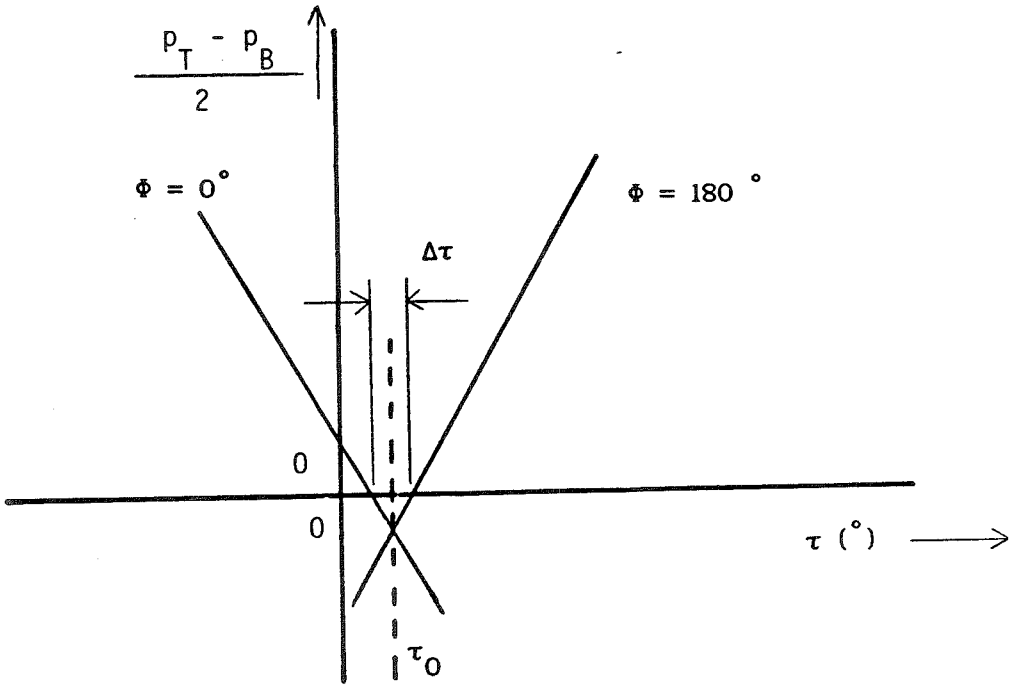

Figure A2.2 . Procedure for finding tunnel flow direction in the plane parallel to the turntable.

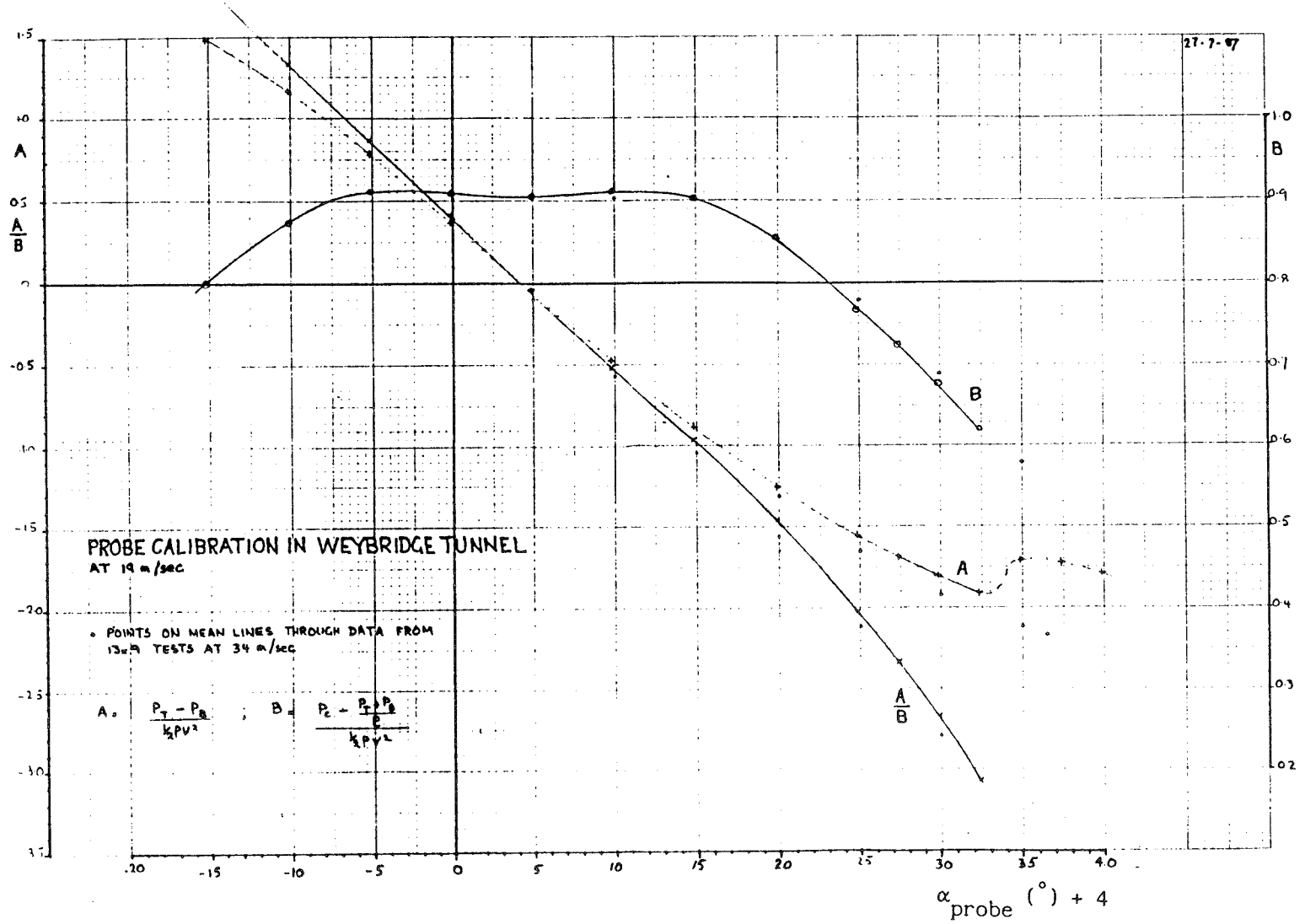

Figure A2.3 . Noseprobe calibration graph .

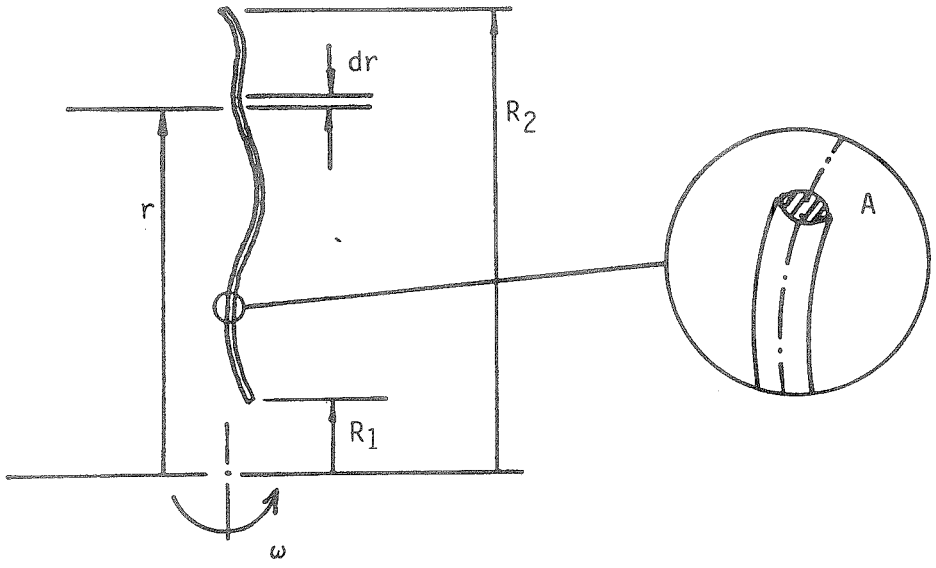

Figure A3.1. Part of pressure measurement system on the WA

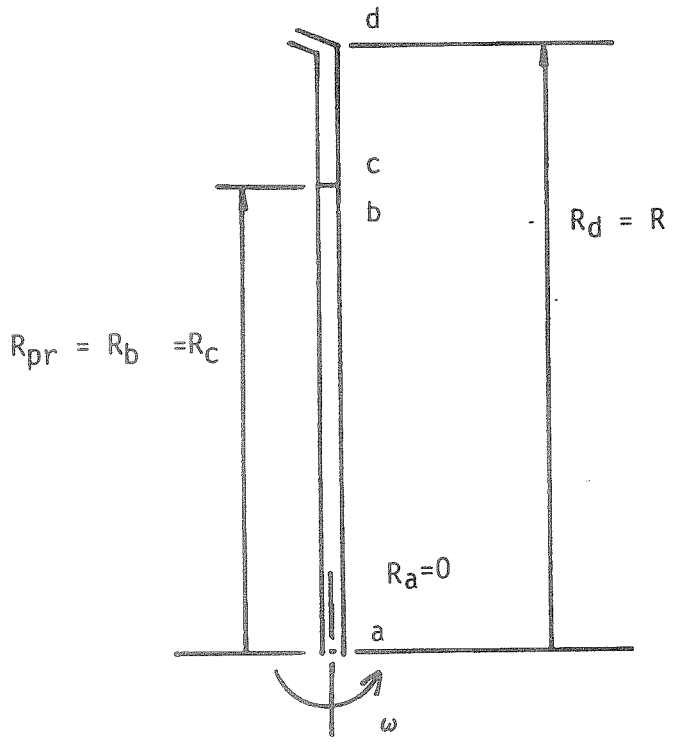

Figure A3.2. General pressure measurement system on the WA

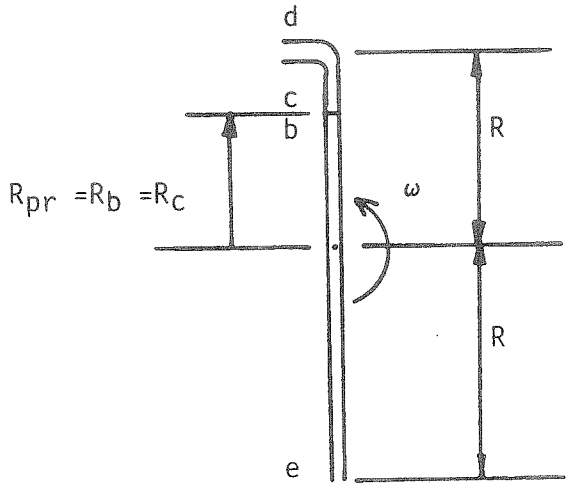

Figure A3.3. Pressure measurement system as used on the WA

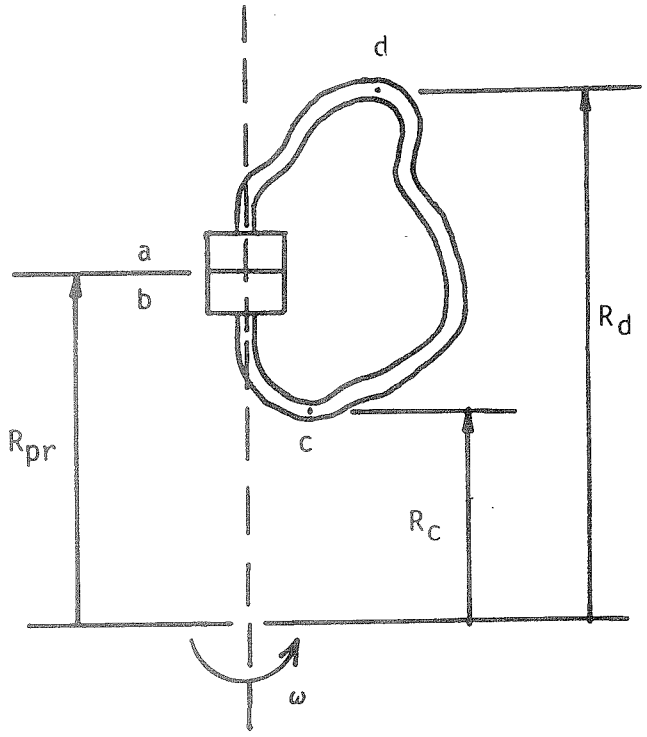

Figure A3.4. Arrangement to check pressure transducer membrane deflection due to centrifugal loading.